Reconnaissance Paleomagnetism of the Northern Rehoboth Basement Inlier, Namibia

Chiara Chung-Halpern

Advisor: David A. D. Evans
Second Reader: Richard Hanson

A Senior Thesis presented to the faculty of the Department of Geology and Geophysics, Yale University, in partial fulfillment of the Bachelor's Degree.

TABLE OF CONTENTS

ABSTRACT:

The Rehoboth Basement Inlier (RBI) lies along the edge of the Kalahari craton at the southern margin of the Pan-African Damara Orogen, Namibia, thus knowledge of its location will be useful in future supercontinent reconstructions. During the Summer of 2019, a reconnaissance study was carried out in the RBI with the primary aim of better constraining the location of the RBI in the Meso-Neoproterozoic. The paleomagnetic data from 31 sites are presented here: 10 sites from the Bitterwater volcanics and quartzites in the Opdam Formation (V19D01-V19D10), 17 sites from the Swartkoppies mafic dykes (C19S01-C19S17), 2 sites from the Uisib River mafic dykes (C19U1 - C19U2), and 2 sites from dolerite dikes intruding the Opdam Formation outside the town of Rehoboth (C19R1-C19R2). All of the Bitterwater sites displayed a strong remanent direction. A fold test was done on 9 of the Bitterwater sites that indicated the occurrence of a syn-folding event. Due to the shallow inclination seen in all of these samples, this was likely due to a much older folding event than the Damara folding event that occurred at mid-latitudes. The Bitterwater sites produced a pole that was estimated to be ca. 1100 Ma in age. What was notable about this pole was that it was rotated 30 degrees from the well-established ca. 1100 Ma paleopole for the Kalahari craton. The majority of the Swartkoppies sites were unable to produce any significant primary remanent magnetic directions, mainly due to lightning strikes and the premature decay of samples. However, C19S14 was able to produce a virtual geomagnetic pole that had a similar location to that of the Bitterwater sites. C19U1 also produced a similar location to C19S14 and the Bitterwater sites. Our results indicate that the Rehoboth Basement Inlier underwent a rotation of approximately 30 degrees clockwise relative to the rest of the Kalahari craton. Previously published data suggest that this rotation affected

magnetization as young as ca. 500 Ma. C19S13 and C19R2 both produce directions that follow the Torsvik et al. 2012 Apparent Polar Wander Path when the 30 degree rotation is applied, at either 520 Ma and 540 Ma respectively, or 1000 and 1030 Ma. Ages for both of these dykes need to be obtained to confirm the origin of these directions. The cause of this rotation remains unclear and opens the door for future investigations.

INTRODUCTION:

The study of past supercontinent reconfigurations is important for not only locating natural resource deposits but also for explaining the evolution of climate during Earth's history. Configurations of past supercontinents are able to be determined using paleomagnetism, where one looks at the past geomagnetic field and utilizes magnetic directions frozen in rocks via magnetic minerals such as hematite and magnetite. In this way, one is able to pinpoint the rock's location in Earth's past.

Large amounts of uncertainty exist in earlier supercontinent reconstructions. For example, the location of the Kalahari craton in the Neoproterozoic is a large issue that remains today. During this time, the Kalahari craton existed as part of the Rodinia Supercontinent, although its location relative to other cratons, such as the Congo craton, still remains widely debated. (Salminen et al. 2018). The Rehoboth Basement Inlier (RBI) remains an ideal site for identifying the past location of the craton, as whilst much of the Kalahari's Meso-Neoproterozoic crust has been metamorphosed, especially in Namibia during the formation of the Damara Orogen at ca. 500-550 Ma, much of it remains exposed today in the RBI with only low-grade metamorphism present. (Becker et al. 2005) (Goscombe et al. 2020) This means there is a high likelihood that any paleomagnetic data collected from this region will not consist of a Cambrian overprint, but will be primary in origin.

In the Summer of 2019, a reconnaissance paleomagnetic study was conducted in the RBI. Samples were collected from 31 sites that can be grouped into 4 general areas: Dordabis (Bitterwater and Protea Farms), Swartkoppies, Uisib, and Rehoboth. This study aims to provide new paleomagnetic data that will be able to constrain the location of the Rehoboth Basement Inlier and therefore the Kalahari craton during the Meso-Neoproterozoic.

REGIONAL GEOLOGY:

The Rehoboth Basement Inlier (RBI), is made up of largely crystalline rocks that are believed to have originated from the Kalahari craton, as well as Paleoproterozoic greenschist rocks that had undergone a metamorphic event 1.7 Ga, syn- and post- tectonic granites and associated volcanic rocks and clastic sedimentary successions from the 1.3-1.0 Ga Namaqua Orogenic Cycle, and swarms of mafic dykes. (Becker et al. 2004). The RBI is located at the southern margin of the Damara Belt, and at the northern edge of the Kalahari craton as displayed in Figure 1. There is progressively less folding as one moves south.

Within the RBI there are numerous intrusive black and brown mafic dykes, mainly with sharp contacts with the country-rock. The dykes do not display any high-grade regional metamorphism or weathering, increasing their likelihood of producing reliable primary remanent directions. In addition, the majority of the dykes have similar northeast/southwest trends that align with the Areb shear zone, indicating that they might have come from the same magmatic event. (Ziegler and Stoessel et al. 1993). Figure 2 displays a zoomed-in version of the RBI with sampling areas marked in green. (Becker et al. 2005)(Shalk et al. 1982)

The Rehoboth swarm is located just outside of Rehoboth town and mainly consists of west-east trending dolerite dykes directly intruding the Opdam formation. (Becker et al. 2005). The Opdam Formation consists of mafic metavolcanic rocks integrated with quartz mica schist. Both the dykes and formations have yet to be dated, thus as a result, one can only estimate the ages by looking at stratigraphic correlations and underlying formations. Figure 3 displays a stratigraphic column adapted from Borg and Maiden et al. 1989. Underlying the Opdam Formation is the Langberg Formation (Becker and Shalk et al. 2008). Since the Langberg formation had been dated to about 1100 Ma, (Van Schijndel et al. 2014) one can set a maximum

age constraint for the Rehoboth dykes at 1100 Ma. In addition, the Kgwebe formation in the Lake Ngami sequence, Botswana, displays similar stratigraphic correlations, so we can make the assumption that the Opdam formation would have a similar age to that of the Kgwebe formation that had been dated to ca. 1106 Ma. (Schwartz et al. 1996)

In the Uisib river valley, 2 mafic dykes were sampled that intruded the Gamsberg Granite Suite, a group of plutons that primarily consist of biotite-bearing microline-orthoclase-oligoclase granite, often with a porphyritic texture. Since the dykes themselves have not been dated, we can set a maximum age for the Uisib river dykes as the age of the granite, at 1100 Ma. (Becker et al. 2005).

The Swartkoppies dykes are a cluster of mafic diabase igneous dykes that intrude 1820 Ma basement granites (Van Schijndel et al. 2014). It is commonly believed that they formed due to rifting between the Congo and Kalahari cratons during the breakup of the Rodinia Supercontinent. However, one cannot rule out the possibility of multiple generations of dykes in the region, thus it is possible that older dykes exist, such as seen at site S14 which cross-cuts dykes S12 and S13. However, it has been hypothesized that the Swartkoppies dykes feed the Opdam formation, thus as a result could also have an age of ca. 1100 Ma.

Ziegler et al. 1990 dated northeast trending dykes of the western RBI to be ca. 821 Ma. However, only four isochron points were used in his geological study, thus as a result it is likely that the dykes would have much older ages of ca. 1100 Ma.

The Dordabis sequence was also identified as a potential site, more specifically, the Bitterwater Member. The Bitterwater member is one of the three members of the Opdam Formation (the other two members are the Idaberg member and the Kupferberg member). (Becker and Shalk et al. 2008). The Bitterwater member consists of quartzites, mafic

metavolcanics with medium to coarse-grained red clastics in the upper section of the Opdam formation. (Borg and Maiden et al. 1989) Due to the previous discussion, the ages are likely to be ca. 1100 Ma.

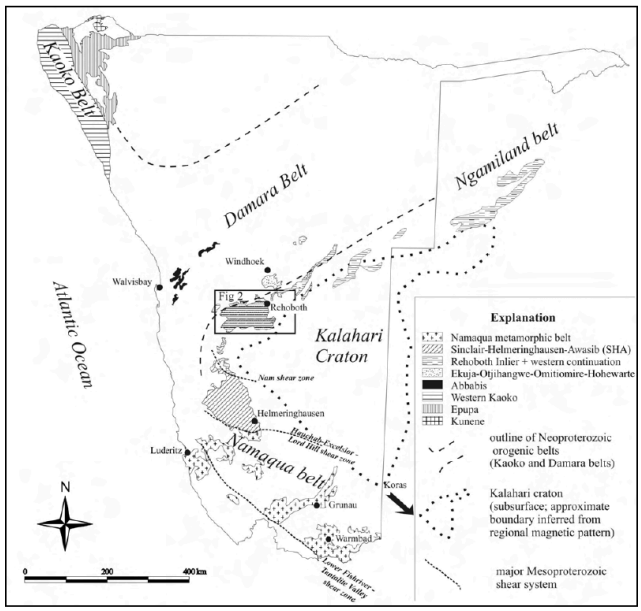

Figure 1: A map of the location of the Rehoboth Basement Inlier in Southern Africa. Taken from Becker et al. 2005

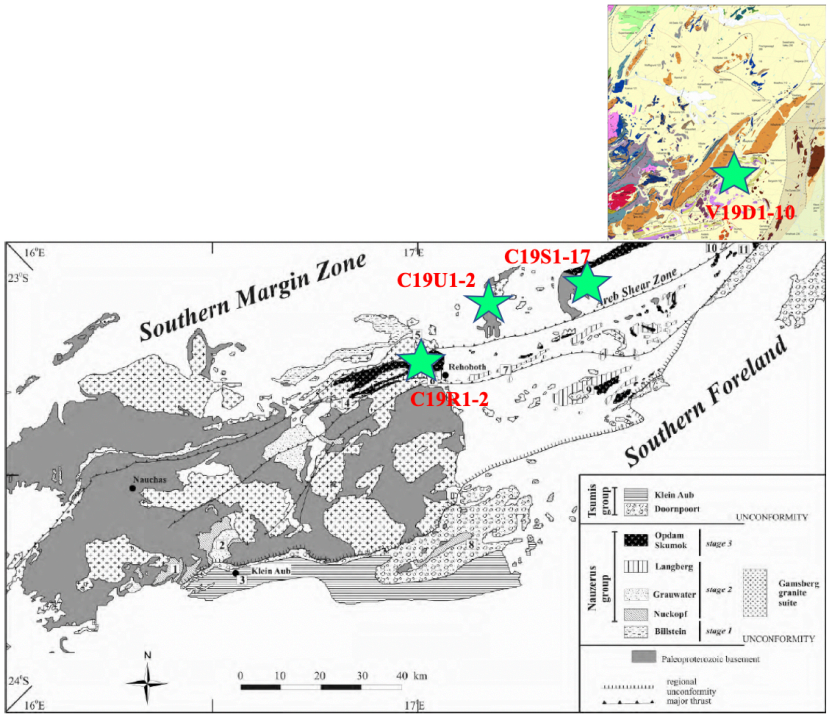

Figure 2: A map of the Rehoboth Basement Inlier, adapted from Becker et al. 2005 and Schalk et al. 2006. Sampling sites are marked in green.

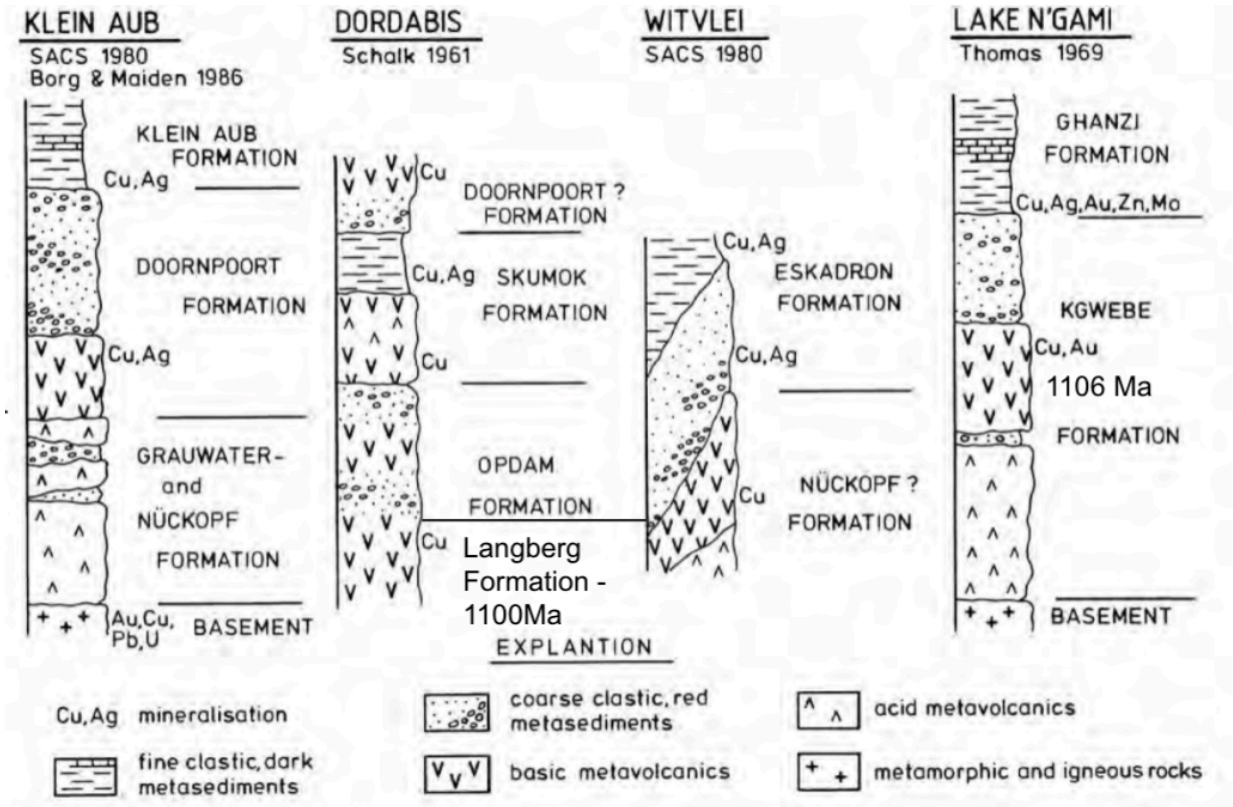

Figure 3: Stratigraphic columns from the Rehoboth Basement Inlier. (Borg and Maiden et al. 1986)

METHODLOLOGY:

During the summer of 2019, 245 samples were collected from 31 sites as part of a reconnaissance field study. The initial study areas were chosen by observing maps created by Becker et al. 2005, as well as Schneider et al. 2006. Google Earth satellite imaging was also utilized to choose the sites, which was useful for directly identifying dykes across the landscape, as well as for marking dirt roads for transportation to the sites.

At each site, the magnetic susceptibility was measured using a portable magnetic susceptibility meter. This measurement enabled us to accurately identify the dyke, which would be expected to have a higher amount of magnetism than the surrounding bedrock. We also recorded the stratigraphic relationships of the outcrops and measured strata thickness and dyke widths. In addition, a magnetic compass was used at every site to check for lightning strikes. If bedding was visible in stratified rocks such as at site V19D01, the strike and dip were taken so tilt corrections would be able to be utilized during later stages of the analysis. 7-9 rock core samples were then extracted using a handheld portable drill with a diamond-encrusted tip. After each sample was measured, an orienting device and clinometer were used to measure hade and the azimuth direction of the drill core. A sun compass was used to measure the shadow angle in order to account for magnetic declination at the site. Although, the general intention was to sample 1 dyke, in several areas crosscutting dikes were observed, such as at C19S04 and C19S05, as well as at C19S14 and C19S15. At these crosscutting dikes, we sampled a transect at the baked contact margin in order to potentially conduct a baked contact test. At each site a sledgehammer was also used to extract block samples of the dyke; should a clear magnetic component be observed in laboratory measurements, the dyke blocks can be used for geochronological U-Pb baddeleyite or zircon dating.

Figure 4: Photographs of sampling in the field (a) TOP PICTURE: Extracting samples using a portable hand drill. Water is pumped to cool the drill bit. (b) LOWER LEFT PICTURE: Taking orientation measurements post-drilling. (c) LOWER RIGHT PICTURE: Searching for suitable outcrops.

The samples were then exported to Kline Geology Laboratory. Pre-arrival, header files were made that would contain their strike, dip, geographic coordinates, and orientation. When the core samples arrived, they were cut using a dual-blade diamond-encrusted rock saw to resize them to ca. 1 inch. This size was large enough to fit correctly in the Anisotropic Measurement System (AMS) machine, which was used to measure the correct orientation of the magnetic minerals within the sample. After the anisotropy of the samples were measured, the samples were cut in half. The samples were then placed into the SquID magnetometer in batches (S01-S05), (S06-S10), (S11-S15), (S16-17, U1-2, R1-2), (D01-D05), and (D06-D10). The magnetometer was first used to measure the NRM. After this initial measurement, the samples were placed overnight in a barrel filled with liquid nitrogen, in order to remove any potential viscous remanent magnetization (VRM). The magnetometer was used again to measure the magnetic direction, before being heated in a magnetically shielded Curie oven to thermally demagnetize the sample. This step was repeated as the magnetic component got stripped away and the Curie temperatures were reached. Certain sites (S01-17, U1-2, and R1-2), were heated until roughly 580°C, the Curie temperature for magnetite, whilst other sites (D01-D10) were heated until roughly 675°C, the Curie temperature for hematite.

At each step, the magnetic direction was plotted onto an orthographic zijderveld diagram and an equal-area stereonet via PaleoMag 3.1.0 b7 computer software. (Jones et al. 2002) Both the zijderveld and stereonet plots displayed the direction's declination and inclination at each step, as well as whether it was pointed up (into the upper hemisphere), or down (into the lower hemisphere). These plots were used to fit lines of best fit for least squares analysis (LSQ), with each line corresponding to a different magnetic direction component. Different names were given to characterize the various components. LN2 stood for the low-temperature component

removed during the liquid nitrogen step. LTH or LTC was used to label the low temperature component, whilst a second low temperature component was named LT2. Decay to origin was labelled HTO (High temperature hematite to origin, that shows decay above 650 °C), MTO (High temperature magnetite to origin, that displays decay until 580°C), and LTO (Low temperature decay to origin). For each type of components seen across all samples within a single site, an equal area plot was created containing the direction of each sample's component across all sites. These points were then analyzed using mainly Fisher statistics (Fisher et al. 1953), (also Bingham statistics) in order to obtain the mean characteristic remanent direction (ChRM) for that sample and a 95% confidence error ellipse. Should the a95 error be low, in general below 20 degrees, the (ChRM) will then be able to be used to calculate a VGP (Virtual Geomagnetic Pole). This VGP was then plotted on GPlates 2.1.0 (Müller et al. 2018), in order to see the geographic location of the pole.

RESULTS:

Swartkoppies Dykes:

Table 1: Paleomagnetic site information for the Swartkoppies Dykes

Name	Location	N	Lithology	Susceptibility (SI)	Width (m)	Altitude(m)	RHS(°)/DIP(°)	Notes
C19S01	23.07542°S 17.49786°E	8	Dolerite	900-1470*10e-6	60 m	1519 m	258°/76°	Southern margin of dyke
C19S02	23.0759°S 17.49759°E	8	Dolerite	1200-2920* 10e-6	10 m	70 m	265°/70°	Lightning point above samples A and B
C19S03	23.07594°S 17.49979°E	8	Dolerite	260-790*10e-6	8.3 m	1523 m	256°/70°	Southern margin
C19S04	23.07631°S 17.49956°E	8	Fine-grained dolerite	2200-16000*10e-6	7 m	1527 m	255°/70°	
C19S05	23.07631°S 17.49956°E	6	Medium-grained dolerite	1829-1990*10e-6	N/A	1527 m	N/A	Drilled within 2cm exocontact of S04
C19S06	23.07639°S 17.49956°E	8	Medium-grained dolerite	2000-26000*10e-6	19 m	1517 m	N/A	Ledge of outcrop
C19S07	23.07956°S 17.50092°E	9	Dolerite	560-1990*10e-6	6 m	1519 m	105°/78°	In shadow of large cliff.
C19S08	23.07972°S 17.50116°E	8	Fine-grained dolerite	1200-3900*10e-6/15,000-20,000*10e-6	2.5 m	1509 m	75°RHS	Shaded by S-facing cliff. 10m south of C19S07.
C19S09	23.08071°S 17.50183°E	8	Fine-grained feldspar porphyry	874-2150*10e-6	14 m	1530 m	95RHS/No margin visible for dip	
C19S10	23.08221°S 17.50211°E	8	Fine-grained mafic dyke with feldspar porphyry	620-950*10e-6	18 m	1520 m	60°/240°	
C19S11	23.1°S 17.5°E	8	Fine-grained feldspar porphyry cutting granitic gneiss	100-12300*10e-6	13 m	1520 m	80°/65°	Southern facing margin
C19S12	23.08467°S 17.50382°E	8	Medium-grained diabase, a	495-708*10-6	5 m	1519 m	N/A	No contact margin.

			bit undulose					
C19S13	23.08628°S 17.50239°E	8	Dolerite, undulose	27-965*10e-6	15 m	1511m	N/A	Sampled near southern margin
C19S14	23.07436°S 17.47999°E	8	Dolerite dyke intruding granitic gneiss	2380-8960*10e-6	5.5 m	1514 m	100°/83°	
C19S15	23.07401°S 17.47892°E	8	Fine-grained porphyry	8000-25000*10e-6	10 m	1546 m	N/A	Exocontact of S14
C19S16	23.07386°S 17.47940°E	8	Fine-grained porphyry	N/A	9 m	1513 m	75°/83°	Same dyke as S15
C19S17	23.07792°S 17.48357°E		Fine-grained feldspar porphyry	3270-5850*10e-6	N/A	1490 m	55°/80°	

S01: Eight rock cores were sampled from a dolerite dyke. The NRMs all had magnetic moments of ca. 1e-04 emu. There was a clear steep south LN2 component seen across all samples. Sample B only had a single component that decayed directly to the origin from low temperature, starting the decay from the NRM. The rest of the samples showed a well-defined low thermal component (LTH) between the LN2 and 100°C, although these thermal components displayed a large scatter, with fisher statistics producing an a95 error of 33.9 degrees. Most samples also had an LT2 component that was similar to the present day direction, starting after step 100°C until step 300°C. The primary component began after the 300°C step until the origin. However, most samples began to scatter before the origin was reached, thus resulting in messy data. 4 samples were clustered with an MTO component (C, D, H and F) of shallow north-northwest direction. It was possible from these 4 samples to obtain a final demagnetization component direction, although the error was large. Due to the large error, this site was not used to calculate a VGP. (Figure 5)

S02: Eight samples were drilled out of a dolerite dyke. The NRM components all displayed magnetic moments of ca. 10e-2 emu, indicating strongly magnetized samples. All samples had extremely prominent LN2 components. LTH components were also present up to the 150°C thermal steps. For all samples, there was a secondary component (MTO) that started after the 150°C step, demagnetizing directly to the origin after being heated to 580°C. Both the LTH and MTO directions showed significant scattering when plotted on an equal-area stereonet; one was unable to identify a single component direction for either sample. Due to the strong magnetic moments, prominent LN2 components, and the significant amount of scatter, it is likely that S02 was struck by lightning. This was further evidenced during the fieldwork, where a lightning point was noticed 1m between the locations of samples A and B. As a result, a VGP was not calculated from this site. (Figure 6)

S03: Eight samples were drilled out of a dolerite dyke's southern margin. For samples A, B, C, and H, the NRMs had magnetic moments of ca. 10e-4 emu. The NRM magnetic moments of samples D, E, F and G were ca. 10e-5emu. Most samples displayed a low thermal component (LTH) until 230°C; the only exceptions to this were A and B, which decayed directly to the origin from low temperatures. One was unable to identify a specific MTO component as there was a significant amount of scattering, with the remanent directions, even when Fisher auto reverse statistics were utilized. As a result, an accurate VGP was unable to be calculated from this site. (Figure 7)

S04: 8 samples were taken from a fine-grained dolerite dyke. All samples had high NRM magnetic moments of around ca. 10e-1 emu. All samples displayed prominent LN2 components, although all samples showed vastly different directions. Furthermore, all samples displayed prominent low thermal decay to the origin, also with large amounts of scatter - producing a

Fisher statistics a95 error of 80.6 degrees. One sample that stood out was A, which showed a higher temperature decay to the origin (MTO) starting from step 300°C. Since there was only one MTO component, this was included in the LTO equal-area stereonet. Overall, the high magnetic moments, prominent LN2 component, and large amounts of scatter in all components indicated that the S04 site was most likely struck by lightning. As a result, a VGP calculation was not included for this site. (Figure 8)

S05: 8 core samples were taken from a medium dolerite mafic dyke that crosscut site S04. The intention at this site was to conduct a baked contact test, with the samples being taken from the 2cm exocontact of the younger dyke (although this did not end up happening as site S04 was struck by lightning). Samples A and C displayed a NRM magnetic moment of ca. 10e-4 emu, whilst samples B, D, E, and F displayed a NRM magnetic moment of ca. 10e-3 emu. During the LN2 step, a large proportion of magnetization was removed from all samples, although the magnetic direction in which this was removed varied. Samples A, B, C, and E all had low thermal (LTH) components that were removed from the LN2 step to 150°C steps. A Bingham statistics distribution produced a 'banana streak' direction that provided a shallow north direction. Samples B and C also produced a second low thermal component (LT2) that was removed by step 425°C, although both showed contrasting directions. C produced a shallow north-northwest direction, and B produced a steep north direction. Samples D and F produced components that decayed to the origin from low temperatures (LTO). Decay to origin components was seen in higher temperatures through the magnetite unblocking temperatures (MTO), although the data is scattered. When combining the MTOs and LTOs, the data is still extremely scattered so no clear magnetic direction is able to be distinguished. Therefore no VGP can be calculated from this site. (Figure 9)

C19S01:

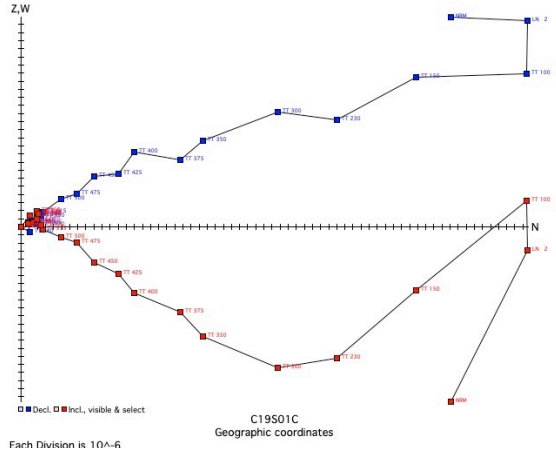

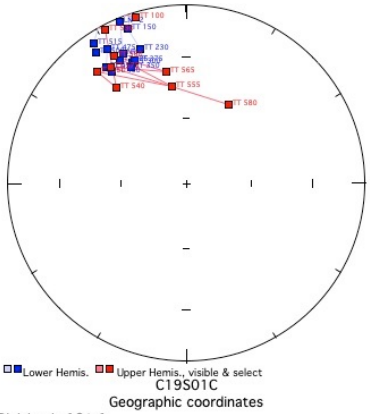

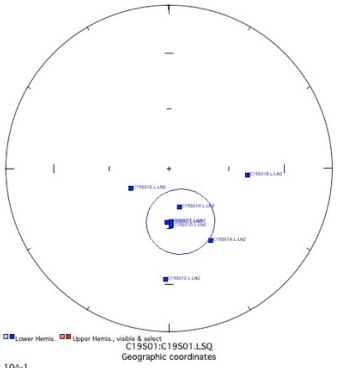

Fisher mean geog. decl.: 167.7, incl.: 62.6 a95 16.6, N: 8

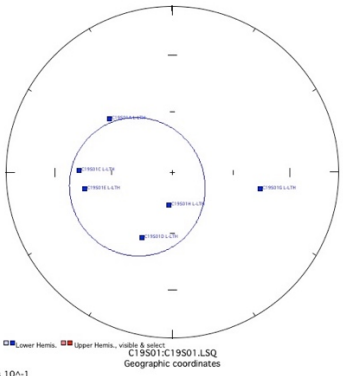

Fisher mean geog. decl.: 247.8, incl.: 70.6 a95 33.9, N: 6

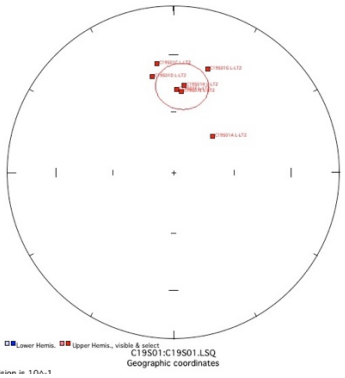

Fisher mean geog. decl.: 5.7, incl.: -46.6 a95 12.1, N: 7

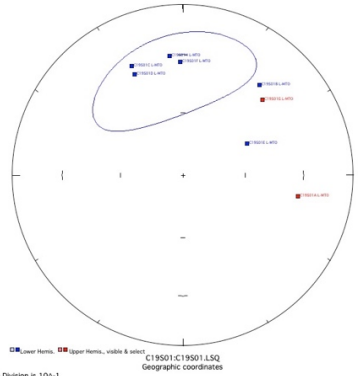

Bingham Mean geog. decl.: 352.7, incl.: 40.5 a95 20.7, 38.7, N: 8

Figure 5: Representative demagnetization behavior from site C19S01. Starting from top row left to right: (a) Zijderveld diagram of sample C19S01C, showing four distinguishable components of the NRM. (b) Equal-area stereonet diagram of sample C19S01C. (c) Equal-area plot of the LN2 component with Fisher statistics 95% confidence ellipse. (d) Equal-area plot of the LTH component with Fisher statistics 95% confidence ellipse. (e) Equal-area plot of the LT2 component with Fisher statistics 95% confidence ellipse. (f) Equal-area plot of the MTO component with Bingham statistics 95% confidence ellipse.

C19S02:

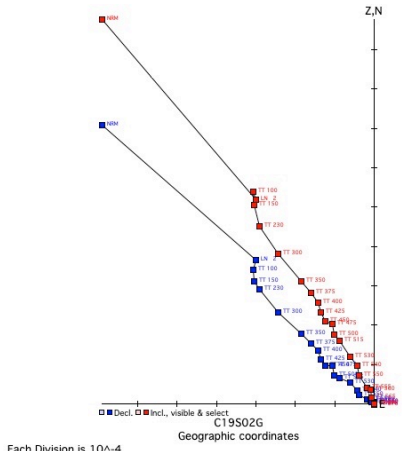

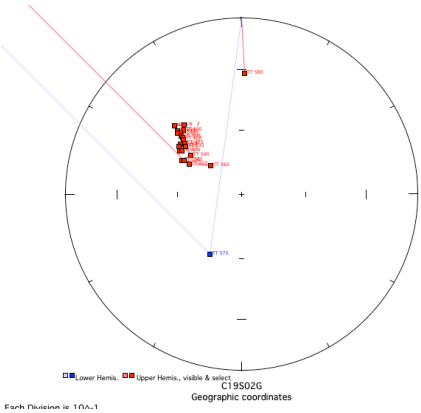

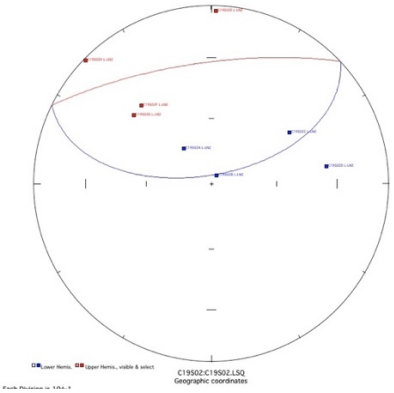

Fisher mean geog. decl.: 351.4, incl.: 26.8 a95 59.4, N: 8

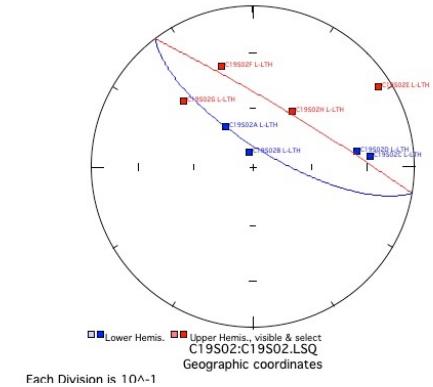

Fisher mean geog. decl.: 31.1, incl.: 12.1 a95 6.8, N

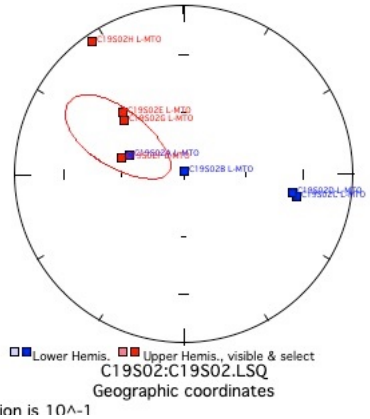

Bingham mean geog. decl.: 299.1, incl.: -52.1 a95 13.1, 31.2, N: 8.

Figure 6: Representative demagnetization behavior from site C19S02. Starting from top row left to right: (a) Zijderveld diagram of sample C19S02G, showing three distinguishable components of the NRM. (b) Equal-area stereonet diagram of sample C19S02G. (c) Equal-area plot of the LN2 component with Fisher statistics 95% confidence ellipse. (d) Equal-area plot of the LTH component with Fisher statistics 95% confidence ellipse. (e) Equal-area plot of the MTO component with Bingham statistics 95% confidence ellipse.

C19S03:

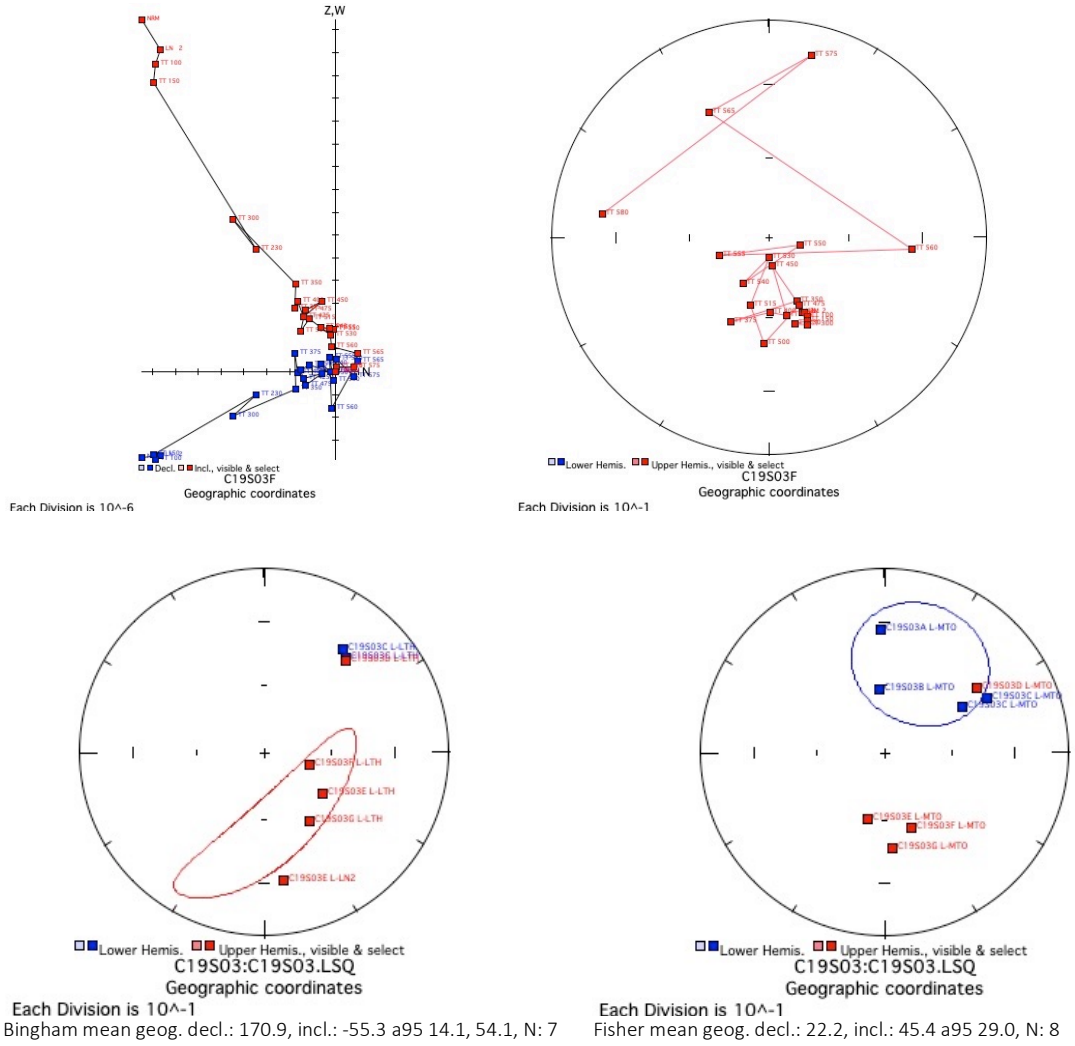

Bingham mean geog. decl.: 170.9, incl.: -55.3 a95 14.1, 54.1, N: 7

Fisher mean geog. decl.: 22.2, incl.: 45.4 a95 29.0, N: 8

Figure 7: Representative demagnetization behavior from site C19S03. Starting from top row left to right: (a) Zijderveld diagram of sample C19S03F, showing two components of the NRM. (b) Equal-area stereonet diagram of sample C19S03F. (c) Equal-area plot of the LTH component with Bingham statistics 95% confidence ellipse. (d) Equal-area plot of the MTO component with Fisher auto-reverse statistics 95% confidence ellipse.

C19S04:

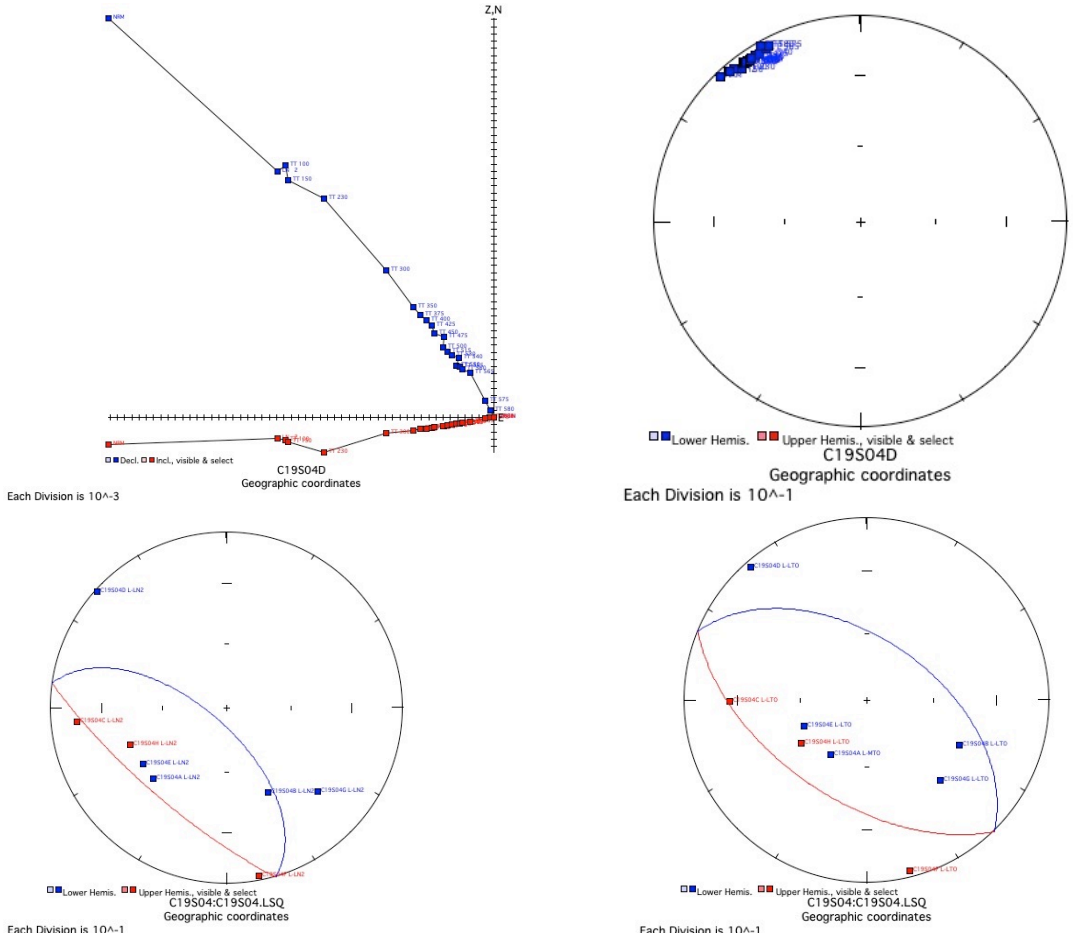

Fisher mean geog. decl.: 221, incl.: -23.4 a95 60.1, N: 8

Fisher mean geog. decl.: 214.1, incl.: 36.7 a95 80.6, N: 8

Figure 8: Representative demagnetization behavior from site C19S04. Starting from top row left to right: (a) Zijderveld diagram of sample C19S04D, showing two components of the NRM. (b) Equal-area stereonet diagram of sample C19S04D. (c) Equal-area plot of the LN2 component with Fisher statistics 95% confidence ellipse. (d) Equal-area plot of the LTO (+ 1 MTO)component with Fisher statistics 95% confidence ellipse.

C19S05:

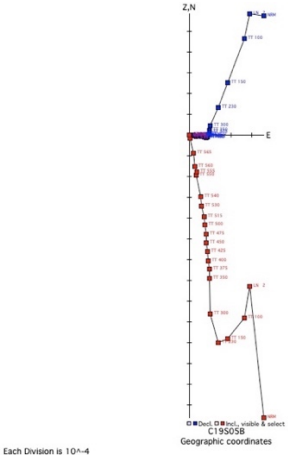

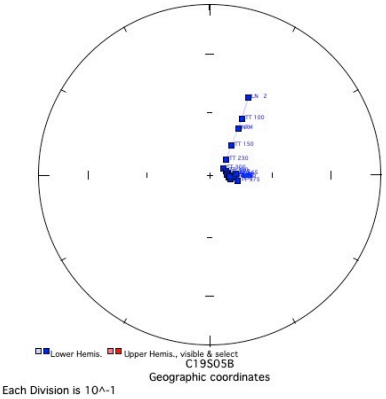

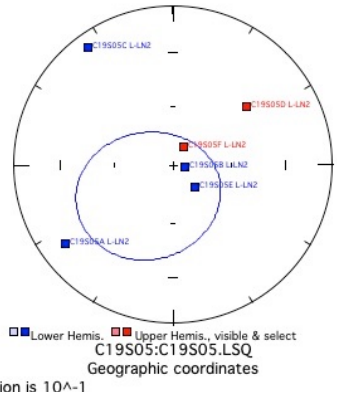

Fisher mean geog. decl.: 218.6, incl.: 68.9 a95 32.7, 38.0, N: 6

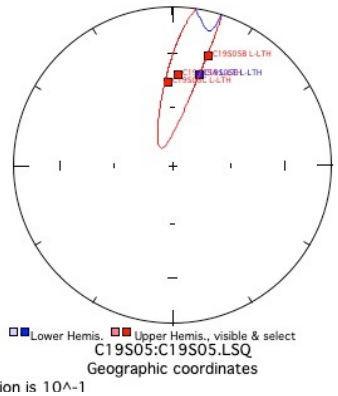

Bingham mean geog. decl.: 8.0, incl.: -34.5 a95 7.3, 47.8, N: 4

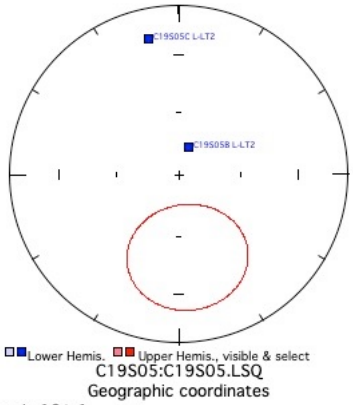

Fisher mean geog. decl.: 353.9, incl.: 48.0 a95 152.6, N: 2

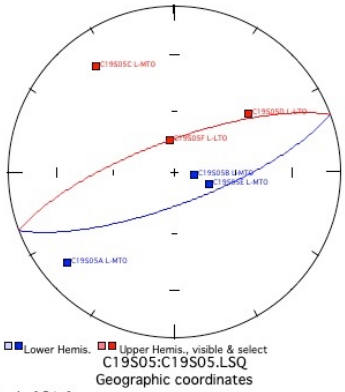

Fisher mean geog. decl.: 339.6, incl.: 15.6 a95 90.0 N: 6

Figure 9: Representative demagnetization behavior from site C19S05. Starting from top row left to right: (a) Zijderveld diagram of sample C19S05B, showing three components of the NRM. (b) Equal-area stereonet diagram of sample C19S05B. (c) Equal-area plot of the LN2 component with Fisher statistics 95% confidence ellipse. (d) Equal-area plot of the LTH component with Bingham statistics 95% confidence ellipse. (e) Equal-area plot of the LT2 component with Fisher statistics 95% confidence ellipse (f) Equal-area plot of the MTO and LTO components combined with Fisher statistics 95% confidence ellipse

S06: 8 samples were taken from a dolerite dyke that was further away from the younger, crosscutting S05 dyke. The NRM magnetic moments for all samples were ca. 10e-1 emu, apart from sample C which had a moment of ca. 10e-3 emu. All samples had extremely prominent LN2 components which heavily demagnetized the sample, although no consistent direction was observed. Sample C and E both produced low-temperature components (LTC) from the LN2 steps to 230°C. In addition, a second low-temperature component (LT2) from 300°C to 425°C was produced by sample C. However, no correlation between any of the low-temperature components was observed. Samples A, B, D, F, and H all produced decay-to-origin components from low temperatures (LTO), whilst C and D had high-temperature components that started to decay before the magnetite unblocking temperatures, from steps 450°C to the endpoint at 580°C. Overall, when looking at either the LTO and MTO components individually or separately, no clear site magnetic direction was able to be distinguished. It is likely that this site was struck by lightning, as evidenced by the large magnetic moment, amount of scattering, and significant LN2 component. No VGP was calculated from this site. (Figure 10)

S07: 9 rock cores were sampled from a dolerite dyke. The NRMs displayed a magnetic moment of ca. 10e-4 emu. All samples showed prominent LN2 components, although all samples displayed varying LN2 directions. In addition, the low-temperature component (LTC) displayed a shallow north-northwest direction that was removed by step 230°C. The decay to origin components were a mixture of LTO and MTO. Samples A, E, F, and G displayed a low-temperature component to the origin, whilst samples I, B, C, D, and H showed a high-temperature decay (MTO). Sample B decayed from steps 375°C until 580°C (the magnetite unblocking temperature). However, the majority of the samples with an MTO component began to demagnetize around the 230°C steps and produced extremely noisy data by 425°C, resulting in

the magnetite unblocking temperature not being reached. The LTOs and MTOs combined on an equal area stereonet produced a shallow northwest direction. However, this direction does not exhibit a high level of precision and is a similar direction to the Cambrian overprint, thus no VGP was calculated from this site. (Figure 11)

S08: 8 samples were drilled out of a fine-grained dolerite dyke 10 meters south of site S07. Since the site was overshadowed by a cliff, no sun compass measurements were taken. The NRMs of samples A, B, and C had magnetic moments of around 10e-3 emu, whilst samples D, E, F, G, and H displayed magnetic moments of ca. 10e-1 emu. Samples D, F and B showed low thermal demagnetization components (LTH) all between the LN2 step and the 230°C step, although no overall distinguishable components were seen. Samples A, C, E, G, and H all displayed low-temperature decay-to-origin components (LTO), with C, G, and H displaying south-east directions, and F and A displaying north-west directions. Samples B, F, and D all produceded shallow north north-west high-temperature decay-to-origin components (MTO) that started from step 230°C and continued demagnetizing straight to the origin. There was a significant amount of scattering seen in the LTO and MTO components, and thus when combined with the strong magnetic moment, strong indicators are present that site S08 was struck by lightning. As a result, no VGP was calculated from site S08. (Figure 12)

S09: 8 samples were drilled from a fine-grained feldspar porphyritic dyke with no visible margin. All samples had NRM components with a magnetic moment of ca. 10e-3. Samples C, E, F and G, and H all display low thermal components (LTH). The low thermal component occured between the NRM and the 230°C steps for samples E, F, and G. In contrast, for sample C, the LTH component demagnetized from the LN2 step to the 540°C step. For sample H, the LTH component demagnetized between the LN2 step to the 425°C step. There was a large amount of

scattering between all the LTH components; all produced directions within the north-east quadrant with varying degrees of steepness. Samples A, B, and D all displayed low-temperature decay to origin components, although the directions were not consistent between samples. Samples C, E, F, G, and H all produced high-temperature components that continued to decay through the unblocking temperatures of magnetite to an endpoint of 580°C. However, consistent magnetic directions were not seen within these samples. No VGP was able to be obtained from this data set as there was no consistent decay-to origin direction observed, even when the MTO and LTO components were combined. (Figure 13)

S10: 8 samples were drilled out of a fine-grained porphyritic dyke. NRM components displayed magnetic moments of ca. 10e-4, although sample F had a slightly stronger magnetic moment of 10e-3. Samples B, D, C, G, and H all displayed low thermal components (LTH), with the demagnetization occurring between the NRM step and the 100°C steps for sites C, D, and G, ending at 230°C for sample B, E, and H. The LTH of samples B, E, H displayed the present day direction, whilst the LTH of samples C, D, and G displayed a shallow northeast direction. 4 samples (B, D, E, and G) also produced a secondary low-temperature component (LT2); for G this component demagnetized between 100°C and 230°C, whilst for B, D and E this demagnetization occurred between 300°C and 425°C. The LT2 indicated a prominent shallow north direction. Samples A, F, and D displayed low-temperature decay to origin components, although the samples did not show a consistent direction. Samples B, C, E, G, and Hall displayed MTO components that with shallow, north northwest directions. Whilst H, C, G, and B had downwards directions, D and H had upward directions which matched the present-day direction thus was not included in the Bingham statistics error ellipse as a result. Overall when combining the LTOs and MTOs and excluding A, D, E, and H, a shallow downward north

northwest component is seen, although the error was still too large to calculate a VGP. (Figure 14)

C19S06:

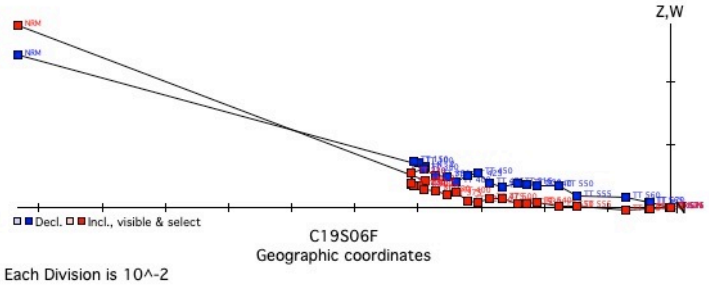

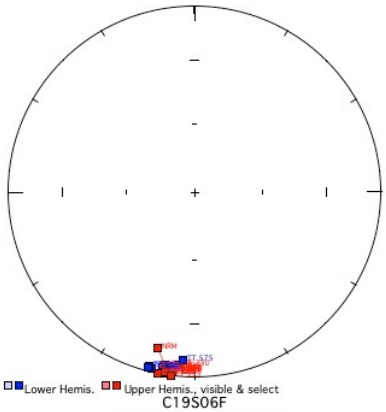

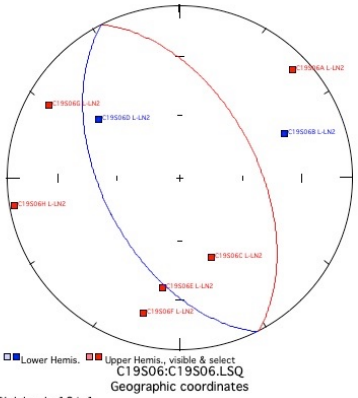

Fisher mean geog. decl.: 243.2, incl.: -37.0 a95 90.0 N: 8

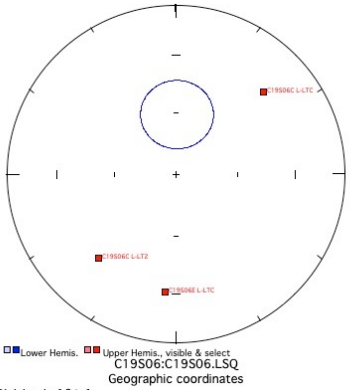

Fisher mean geog. decl.: 180.9, incl.: -60.6 a95 163.6 N: 3

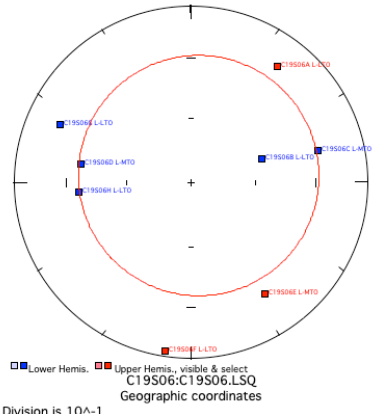

Fisher mean geog. Decl226.5, incl.: 84.5 a95 122.5 N: 8

Figure 10: Representative demagnetization behavior from site C19S06. Starting from top row left to right: (a) Zijderveld diagram of sample C19S06F, showing two components of the NRM. (b) Equal-area stereonet diagram of sample C19S06F. (c) Equal-area plot of the LN2 component with Fisher statistics 95% confidence ellipse. (d) Equal-area plot of the LTC and LT2 components with Fisher statistics 95% confidence ellipse. (e) Equal-area plot of the LTO and MTO components with Fisher statistics 95% confidence ellipse.

C19S07:

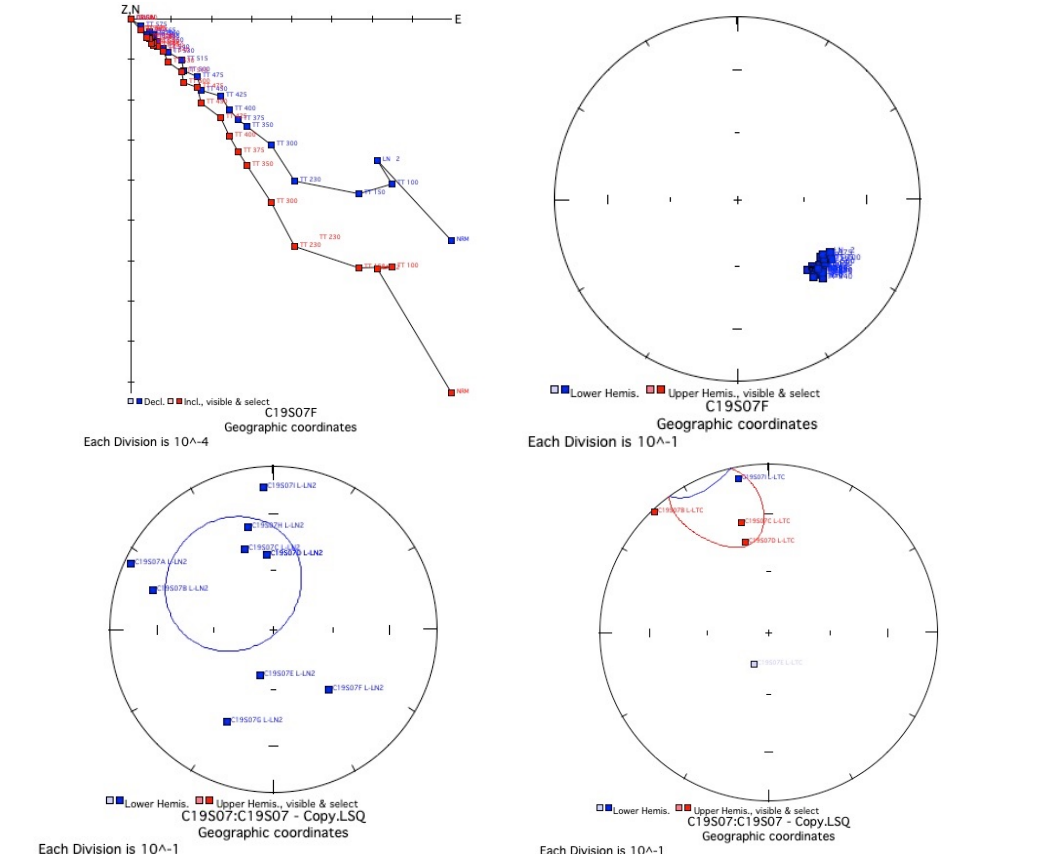

Fisher mean geog. decl.: 319.0 incl.: 58.0 a95 34.0 N: 10

Bingham mean geog. decl.: 339.6, incl.: 15.6 a95 15.7, 27.8 N: 4

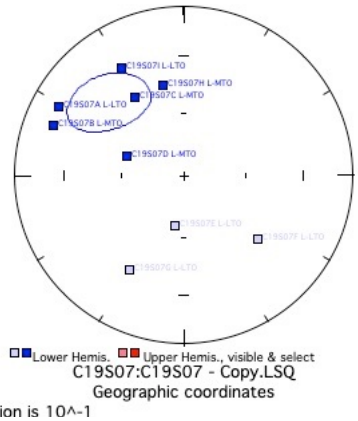

Bingham mean geog. decl.: 314.3 incl.: 37.4 a95 13.7, 20.0, N: 6

Figure 11: Representative demagnetization behavior from site C19S07. Starting from top row left to right: (a) Zijderveld diagram of sample C19S07F, showing three components of the NRM. (b) Equal-area stereonet diagram of sample C19S07F. (c) Equal-area plot of the LN2 component with Fisher statistics 95% confidence ellipse. (d) Equal-area plot of the LTC components with Bingham statistics 95% confidence ellipse. (e) Equal-area plot of the LTO and MTO components with Bingham statistics 95% confidence ellipse.

C19S08:

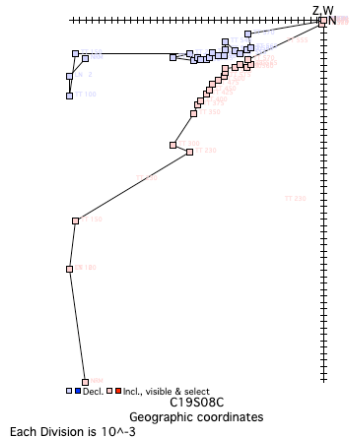

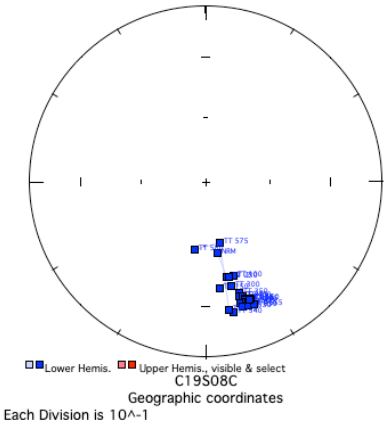

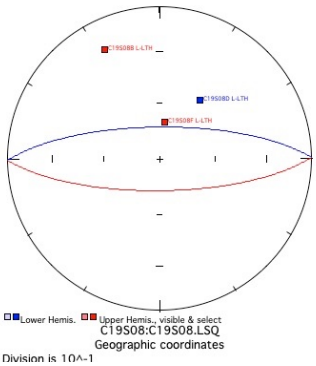

Fisher mean geog. decl.: 359.5 incl.: -17.0 a95 90.0 N: 3

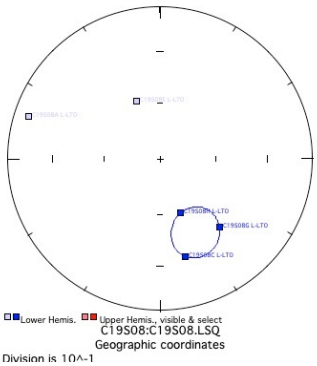

Fisher mean geog. decl.: 154.3 incl.: 45.1 a95 12.3 N: 3

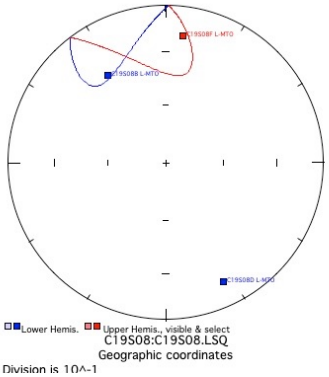

Bingham mean geog. decl.: 343.7 incl.: -4.0 a95 17.2, 45.8 N: 3

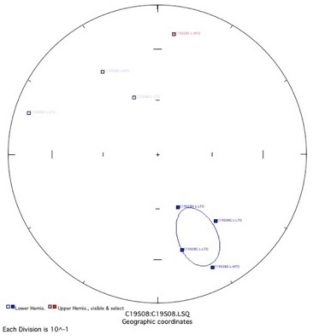

Bingham mean geog. decl.: 154.2, incl.: 38.0 a95 9.6, 18.6, N: 4

Figure 12: Representative demagnetization behavior from site C19S08. Starting from top row left to right: (a) Zijderveld diagram of sample C19S08C, showing two components of the NRM. (b) Equal-area stereonet diagram of sample C19S08C. (c) Equal-area plot of the LTH component with Fisher statistics 95% confidence ellipse. (d) Equal-area plot of the LTO components with Fisher statistics 95% confidence ellipse. (e) Equal-area plot of the MTO components with Bingham statistics 95% confidence ellipse. (f) Equal-area plot of the MTO and LTO components combined with Bingham statistics 95% confidence ellipse.

C19S09:

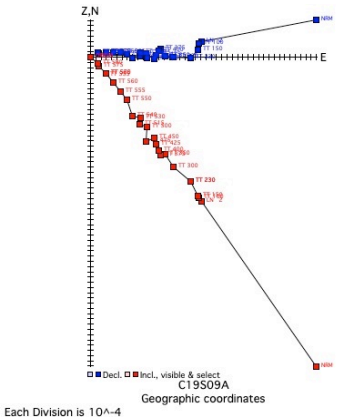

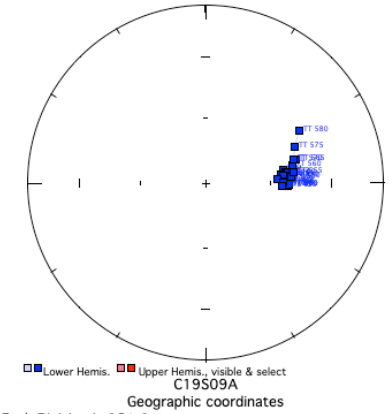

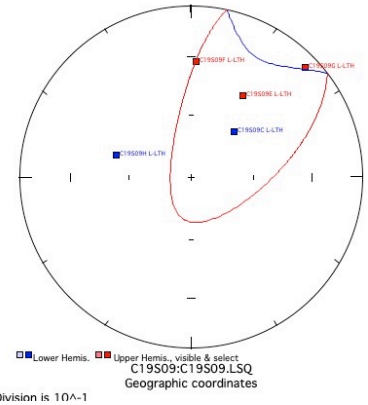

Bingham mean geog. decl.: 38.1 incl.: -43.1 a95 28.7, 65.2 N: 5

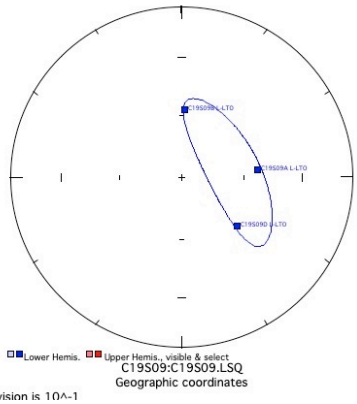

Bingham mean geog. decl.: 81.2 incl.: 65.3 a95 12.8, 38.9, N: 3 (A,B,D)

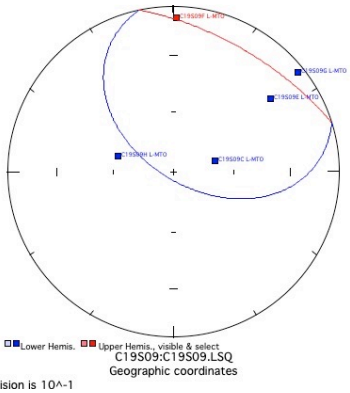

Fisher mean geog. decl.: 30.3 incl.: 38.8 a95 54.8 N: 5

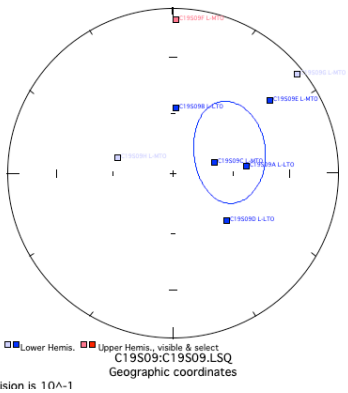

Bingham mean geog. decl.: 59.6 incl.: 18.1, 24.6 a95 24.6 N: 5

Figure 13: Representative demagnetization behavior from site C19S09. Starting from top row left to right: (a) Zijderveld diagram of sample C19S09A, showing one component of NRM. (b) Equal-area stereonet diagram of sample C19S09A. (c) Equal-area plot of the LTH component with Bingham statistics 95% confidence ellipse. (d) Equal-area plot of the LTO components with Bingham statistics 95% confidence ellipse. (e) Equal-area plot of the MTO components with Fisher statistics 95% confidence ellipse. (f) Equal-area plot of the MTO and LTO components combined with Bingham statistics 95% confidence ellipse.

C19S10:

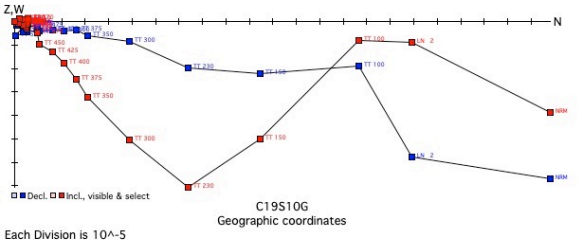

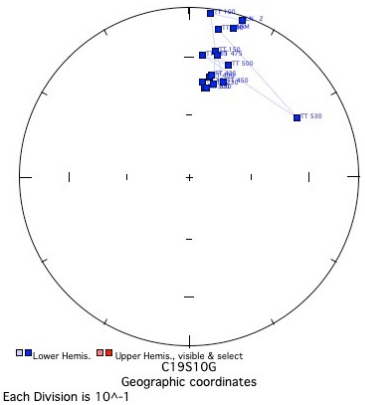

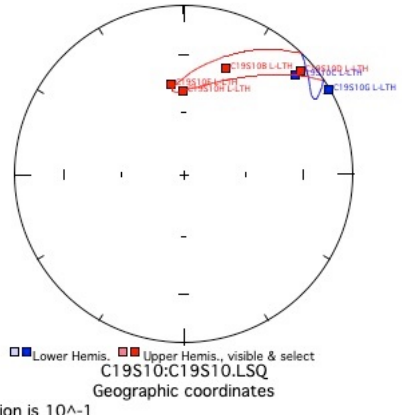

Bingham mean geog. decl.: 33.5 incl.: -21.7 a95 6.2, 42.5, N: 6

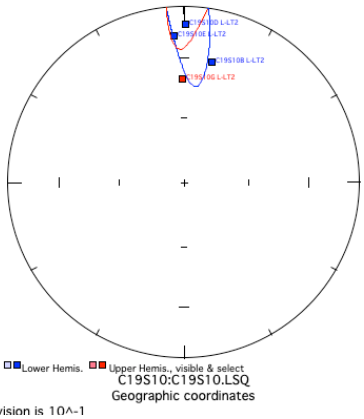

Bingham mean geog. decl.: 2.1, incl.: 9.6 a95 7.1, 35.1, N: 4

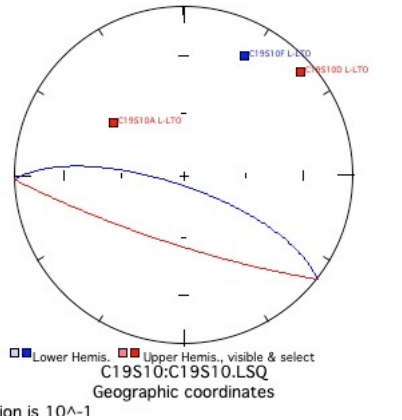

Fisher mean geog. decl.: 18.2 incl.: -14.3 a95 108.9 N: 3

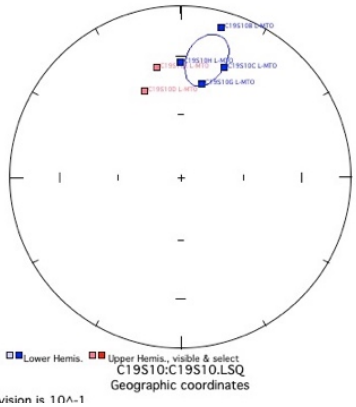

Bingham mean geog. decl.: 12.3 incl.: 30.1 a95 8.1, 15.0 N: 4

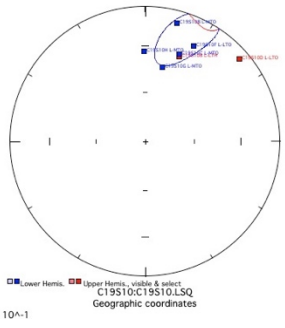

Bingham mean geog. decl.: 20.9 incl.: 10.2 a95 10.2, 25.4, N: 7

Figure 14: Representative demagnetization behavior from site C19S10. Starting from top row left to right: (a) Zijderveld diagram of sample C19S10G, showing three components of NRM. (b) Equal-area stereonet diagram of sample C19S10G. (c) Equal-area plot of the LTH component with Bingham statistics 95% confidence ellipse. (d) Equal-area plot of the LT2 components with Bingham statistics 95% confidence ellipse. (e) Equal-area plot of the LTO components with Fisher statistics 95% confidence ellipse. (f) Equal-area plot of the MTO components with Bingham statistics 95% confidence ellipse. (g) Equal-area plot of the MTO and LTO components combined with Bingham statistics 95% confidence ellipse.

S11: 8 samples were drilled from a fine-grained feldspar porphyritic dyke that had fewer phenocrysts than sites S09 and S10. The dyke cut across granitic gneiss, with a south-facing margin. Most samples had NRM magnetic moments of ca. 10e-4 emu, although sample B had a magnetic moment of ca. 10e-2 emu. All samples displayed significant demagnetization throughout the LN2 component, although when shown on an equal area plot a singular consistent direction was not indicated.. In addition, most samples displayed low thermal demagnetization components. These occurred between steps 100°C and 230°C for samples A, C F, and H, and between the NRM step and 100°C for samples D, E, and G. Overall there was no clear LTH component, although samples A, C, H and F clustered around the present-day direction. Samples A, G, and F displayed a secondary low-temperature component from steps 230°C to 430°C, although no consistent direction was seen. Samples D and B both contained a low thermal origin component that were both with a northwest direction, but in different hemispheres and with varying steepness. However, a high-temperature component to origin (MTO) was seen from steps 300°C to 450°C in samples E, H, G, and A. Unfortunately, the samples began to die before reaching the origin, resulting in a large amount of noise before the magnetite unblocking temperature is reached. Overall, there is a clear MTO direction of northwest and down, although the not-so-clear decay to the origin makes this site unusable for a VGP calculation. (Figure 15)

S12: 8 samples were collected from a medium-grained dolerite dyke at the base of a hill. The NRMs of all the samples displayed a magnetic moment of ca. 10-5 emu. All samples displayed an upwards, moderately shallow north low thermal component (LTH) that was demagnetized by steps 100°C, 150°C, or 230°C. The LTH direction matched the present-day direction. Sample A also had a secondary low-temperature thermal component (LT2) that demagnetized between steps 150°C and 300°C. The LT2 component also had an upwards,

moderately shallow north direction. The only sample that displayed a low-temperature decay directly to the origin (LTO) was sample H, which also displayed the same present-day direction as the other samples' LTO directions. All other samples displayed a high-temperature decay to origin (MTO), from steps 300°C to 430°C. Unfortunately large scatter began to appear on the orthographic zijderveld diagrams before the magnetite unblocking temperature was reached, although a prominent down and shallow, north northwest MTO direction was seen across all samples. Therefore a VGP was calculated from this site. (Figure 16)

S13: 8 samples were collected from a dolerite dyke that had formed a ridge/hill (the same hill at which site S12 was located). All samples had an NRM magnetic moment of ca. 10-4 emu. All sites had a clear LN2 component in the upper hemisphere, all located in the southwestern quadrant of the equal area plot (apart from sample E). In addition, all samples apart from E and A displayed a low-temperature thermal component (LTH) starting from the LN2 or 100°C step until the 230°C or 300°C step. All LTH components displayed an upwards, steep north, or northeast direction. Sample B displayed a second low-temperature component (LT2) that demagnetized between step 100°C and 230°C, with an upwards, moderately steep north northwest direction. Samples B and E displayed a single decay to origin component from low temperatures, both of which had a downwards north-west component. A high-temperature component (MTO) was also displayed between steps 300°C to 430°C or 500°C, although the magnetic component began to break down and scatter in all samples before the magnetite unblocking temperature was reached. Nevertheless, all the MTOs were clustered in a North-northwest direction, enabling a VGP to be calculated from this site. (Figure 17)

S14: 8 samples were drilled out of a dolerite dyke that intruded granitic gneiss. All samples displayed an NRM magnetic moment of ca. 10-3 emu. All samples showed a significant

LN2 component during the demagnetization process, although no consistent direction was seen within the site. The low thermal component was removed between either the LN2 or 100°C and the 230°C step. The LTH step gives a set of upper-hemisphere, north-northwest, moderately shallow directions, that was similar to the present day direction. A secondary low-temperature component (LT2) was also seen with a downwards, shallow north-northwest direction between steps 230°C and 470°C. What was most significant was the high temperature to origin component, which demagnetized until either the 560°C step or the 580°C step (the magnetite unblocking temperature). Here, the samples formed a tight cluster of extremely shallow, south-southwest directions , apart from H which indicated a downwards north-east component that was not included in the Fisher statistics calculation. Due to the tight cluster of MTO components, site S14 can be used to calculate a VGP. (Figure 18)

S15: Site S15 consisted of a fine-grained porphyritic dyke that crosscut site S14 (younger). 8 samples were collected at the dyke's exocontact whilst sampling along a transect towards its center in the hopes of conducting a baked contact test. Samples A, B, C, D, E, and F had NRM magnetic moments of ca. 10-1 emu, whilst samples G and H had magnetic moments of ca. 10-3 emu. All sites showed a significantly removed LN2 component, although the directions were inconsistent between samples. Samples D and H both displayed a low thermal (LTH) component that was completely removed by step 150°C for sample D, and by step 470°C for sample H. However, both samples showed contrasting directions. Samples D and H showed a high-temperature component, where the magnetism continued to be removed at the magnetite unblocking temperature (MTO). Samples D and H did not show consistent MTO directions. All other samples displayed a low-temperature decay to the origin (LTO). All directions were shallow, but there was significant scattering seen on the LTO equal area plot, with directions

ranging from southeast to northeast. Due to significant magnetic removal at the LN2 stage, strong magnetism, and the lack of a consistent magnetic component at the LTO stage, it is likely that S15 was struck by lightning, thus no VGP was able to be calculated from this site, and no baked contact test was able to be carried out. (Figure 19)

S16: Site S16 consisted of the same dyke as S15, but further away from the younger S14 dyke. The NRMs displayed magnetic moments of ca. 10-3 emu (B, C, E), or ca. 10-4 emu (A, D, F, G, H). All samples showed a significant magnetic removal at the LN2 step, although no consistent direction was seen. A low thermal component (LTH) was observed in most samples between temperatures of 100°C and 230°C or 430°C, producing a generally shallow north direction in the upper hemisphere. The only sample producing a secondary low thermal component (LT2) was D, a similarly shallow upper hemisphere north direction was observed that was removed between steps 100°C and 230°C. Sample D, C and E all produced low temperature to origin components, with no consistent directions present. However, from 300°C to 470°C in samples F and H, as well as from 480°C in sample B and 530°C in sample C, a high-temperature component was observed (MTO), although for most samples it did not reach the magnetite unblocking temperature. When combining the MTO and LTO components and reversing sample B's MTO direction, a cluster formed of decay-to-origin components with a downwards, shallow, north northwest direction. A VGP is calculated from this site. (Figure 20)

S17: 8 samples were collected from the southern margin of a fine-grained feldspar porphyritic dyke. All NRM magnetic moments were ca. 10e-4 emu. All samples displayed significant amounts of demagnetization along with the LN2 components, although no reliable direction was obtained when using Bingham statistics. All samples also exhibited an LTH component, that fully demagnetized by step 230°C or 300°C with a mildly shallow, upper

hemisphere north direction. However, during the high temperature to origin stage of demagnetization (MTO) from steps 370°C until 560°C, no consistent magnetic direction was observed. (Figure 21)

C19S11:

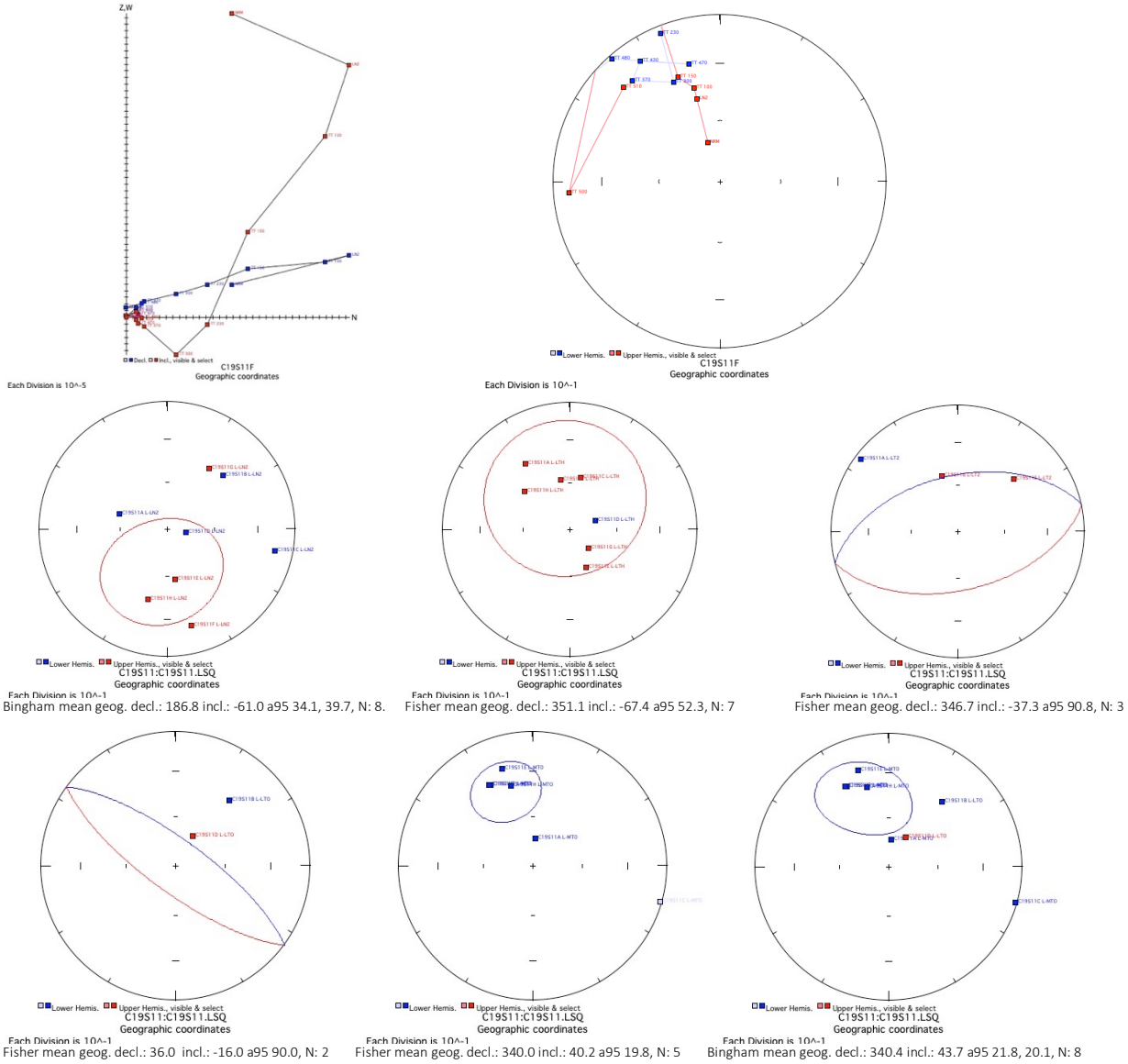

Figure 15: Representative demagnetization behavior from site C19S11. Starting from top row left to right: (a) Zijderveld diagram of sample C19S11F, showing three components of NRM. (b) Equal-area stereonet diagram of sample C19S11F. (c) Equal-area plot of the LN2 component with Bingham statistics 95% confidence ellipse. (d) Equal-area plot of the LTH components with Fisher statistics 95% confidence ellipse. (e) Equal-area plot of the LT2 components with Fisher statistics 95% confidence ellipse. (f) Equal-area plot of the LTO components combined with Fisher statistics 95% confidence ellipse. (g) Equal-area plot of the MTO components combined with Fisher statistics 95% confidence ellipse. (h) Equal-area plot of the LTO +MTO components combined with Bingham statistics 95% confidence ellipse.

C19S12:

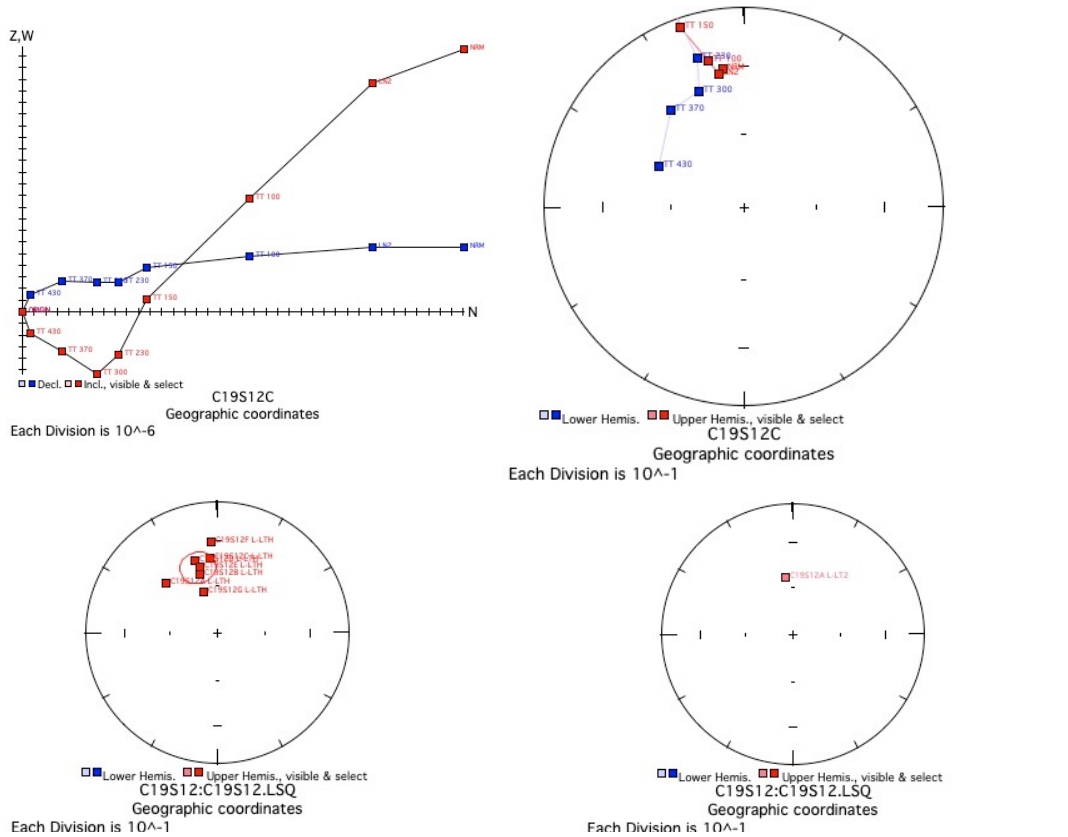

Fisher mean geog. decl.: 343.3 incl.: -46.7 a95 10.4, N: 7

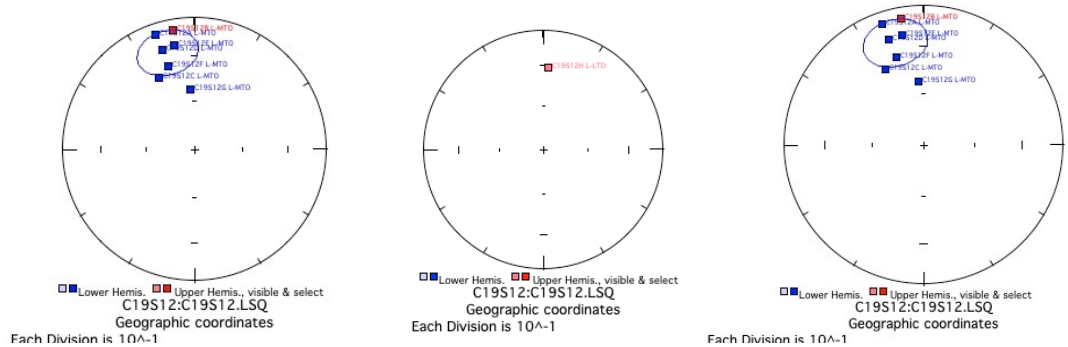

Fisher mean geog. decl.: 343.6 incl.: 29.9 a95 13.8, N: 6

Bingham mean geog. decl.: 345.9 incl.: 20.0 a95 5.6, 23.0, N: 8

Figure 16: Representative demagnetization behavior from site C19S12. Starting from top row left to right: (a) Zijderveld diagram of sample C19S12C, showing two components of NRM. (b) Equal-area stereonet diagram of sample C19S12C. (c) Equal-area plot of the LTH component with Fisher statistics 95% confidence ellipse. (d) Equal-area plot of the LT2 component. (f) Equal-area plot of the MTO components combined with Fisher statistics 95% confidence ellipse. (g) Equal-area plot of the LTO component (h) Equal-area plot of the LTO +MTO components combined with Bingham statistics 95% confidence ellipse.

C19S13:

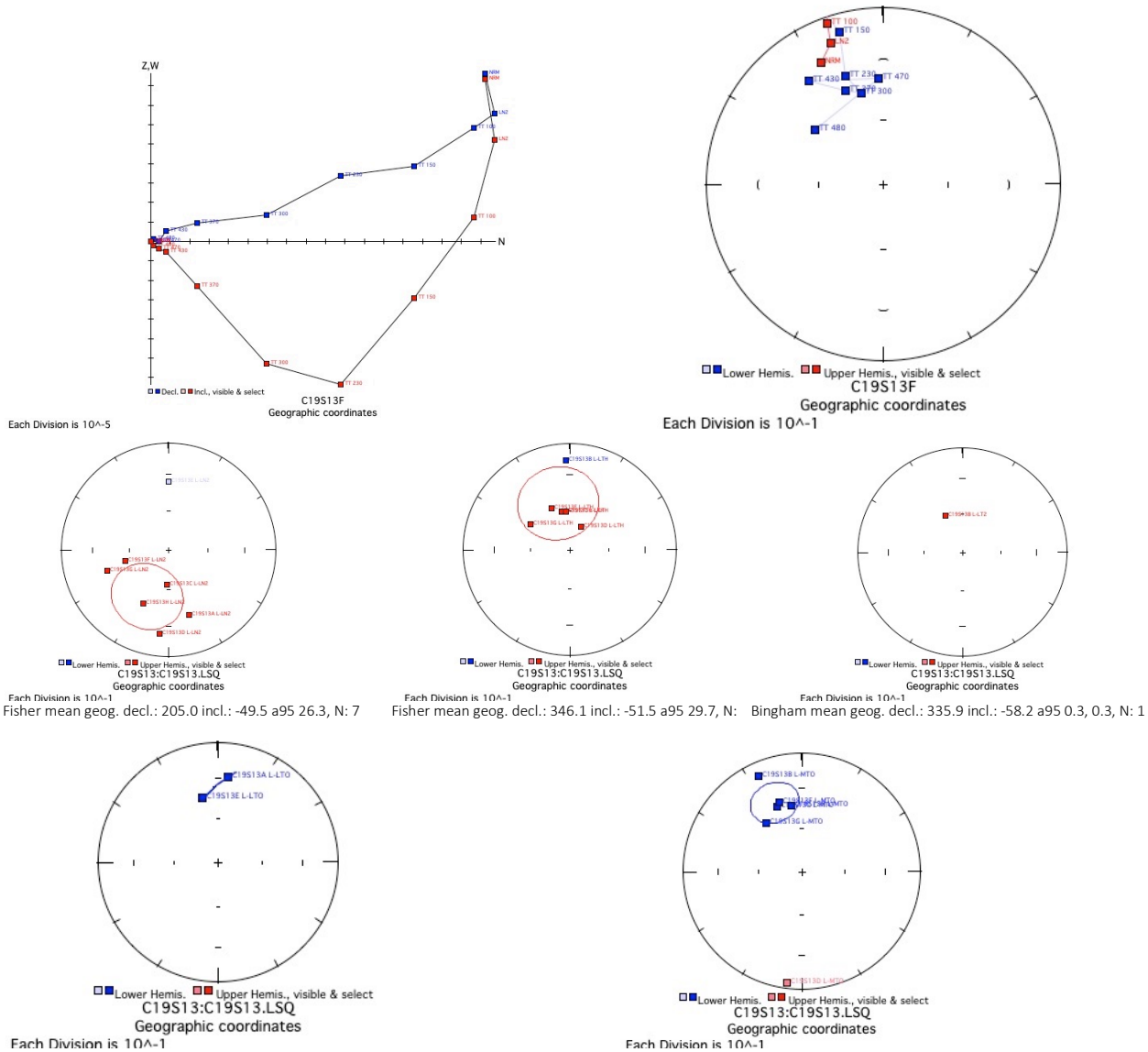

Fisher mean geog. decl.: 205.0 incl.: -49.5 a95 26.3, N: 7

Fisher mean geog. decl.: 346.1 incl.: -51.5 a95 29.7, N:

Bingham mean geog. decl.: 335.9 incl.: -58.2 a95 0.3, 0.3, N: 1

Bingham mean geog. decl.: 357.4 incl.: 36.9 a95 0.2, 18.1, N: 2.

Fisher mean geog. decl.: 338.5 incl.: 37.0 a95 15.2, N: 5.

Figure 17: Representative demagnetization behavior from site C19S13. Starting from top row left to right: (a) Zijderveld diagram of sample C19S13F, showing three components of NRM. (b) Equal-area stereonet diagram of sample C19S13F. (c) Equal-area plot of the LN2 component with Fisher statistics 95% confidence ellipse. (d) Equal-area plot of the LTH component with Fisher statistics 95% confidence ellipse. (e) Equal-area plot of the LT2 component. (f) Equal-area plot of the LTO component combined with Fisher statistics 95% confidence ellipse. (g) Equal-area plot of the MTO components combined with Fisherstatistics 95% confidence ellipse.

C19S14:

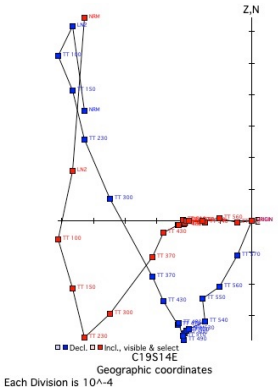

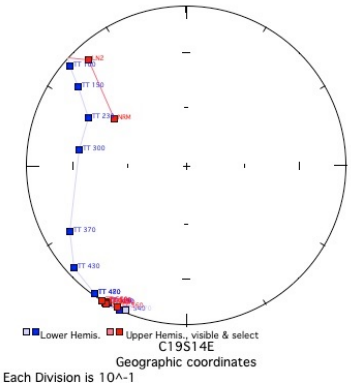

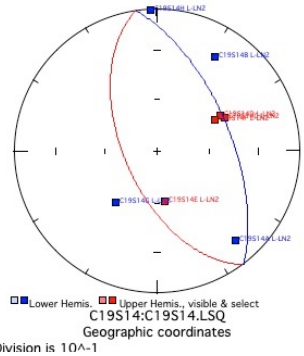

Fisher mean geog. decl.: 67.1 incl.: -31.0 a95 77.7, N: 8

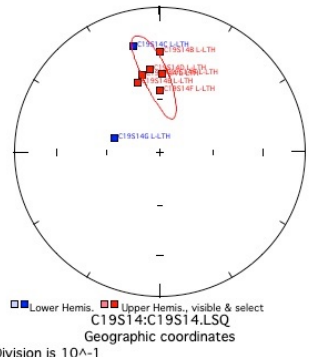

Bingham mean geog. decl.: 356.5, incl.: -45.4 a95 6.6, 27.3, N: 8

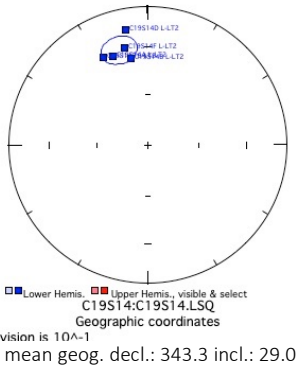

Fisher mean geog. decl.: 343.3 incl.: 29.0 a95 9.3, N: 5

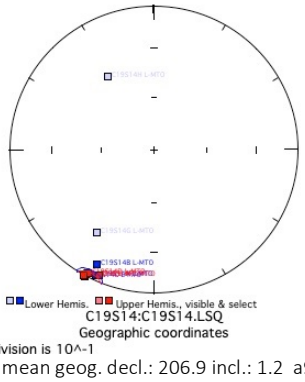

Fisher mean geog. decl.: 206.9 incl.: 1.2 a95 5.5, N: 6

Figure 18: Representative demagnetization behavior from site C19S14. Starting from top row left to right: (a) Zijderveld diagram of sample C19S14E, showing three components of NRM. (b) Equal-area stereonet diagram of sample C19S14E. (c) Equal-area plot of the LN2 component with Fisher statistics 95% confidence ellipse. (d) Equal-area plot of the LTH component with Bingham statistics 95% confidence ellipse. (e) Equal-area plot of the LT2 component with Fisher statistics 95% confidence ellipse (f) Equal-area plot of the MTO components with Fisher statistics 95% confidence ellipse.

C19S15:

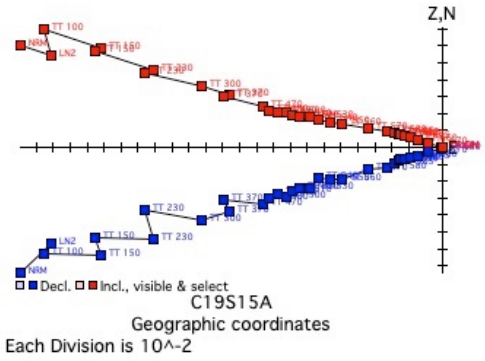

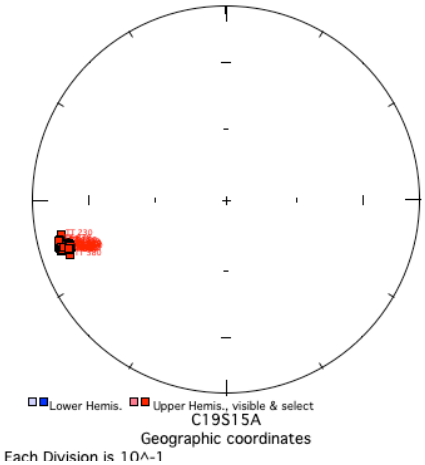

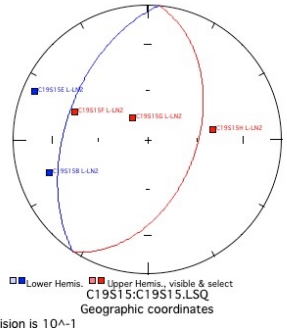

Fisher mean geog. decl.: 289.2 incl.: -40.7 a95 79.1, N: 5

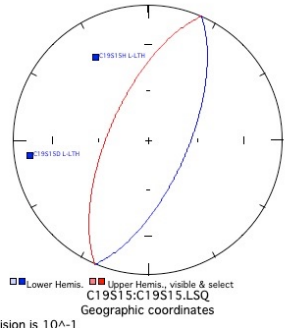

Fisher mean geog. decl.: 293.3 incl.: 24.1 a95 90, N: 2

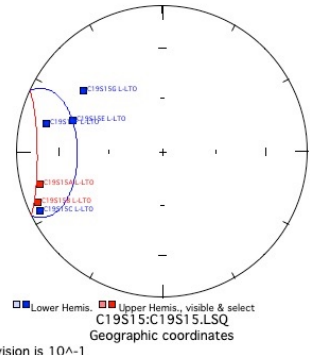

Fisher mean geog. decl.: 269.5 incl.: 13.5 a95 28.3, N: 6

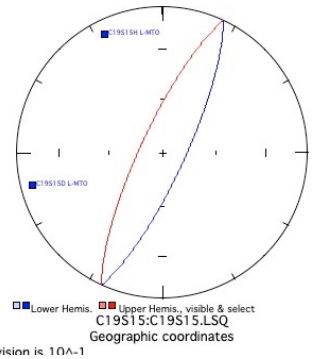

Fisher mean geog. decl.: 294.8 incl.: 12.6 a95 90.0, N: 2

Figure 19: Representative demagnetization behavior from site C19S15. Starting from top row left to right: (a) Zijderveld diagram of sample C19S15A, showing one component of the NRM. (b) Equal-area stereonet diagram of sample C19S015A. (c) Equal-area plot of the LN2 component with Fisher statistics 95% confidence ellipse. (d) Equal-area plot of the LTH component with Fisher statistics 95% confidence ellipse. (e) Equal-area plot of the LTO component with Fisher statistics 95% confidence ellipse (f) Equal-area plot of the MTO component with Fisher statistics 95% confidence ellipse

C19S16:

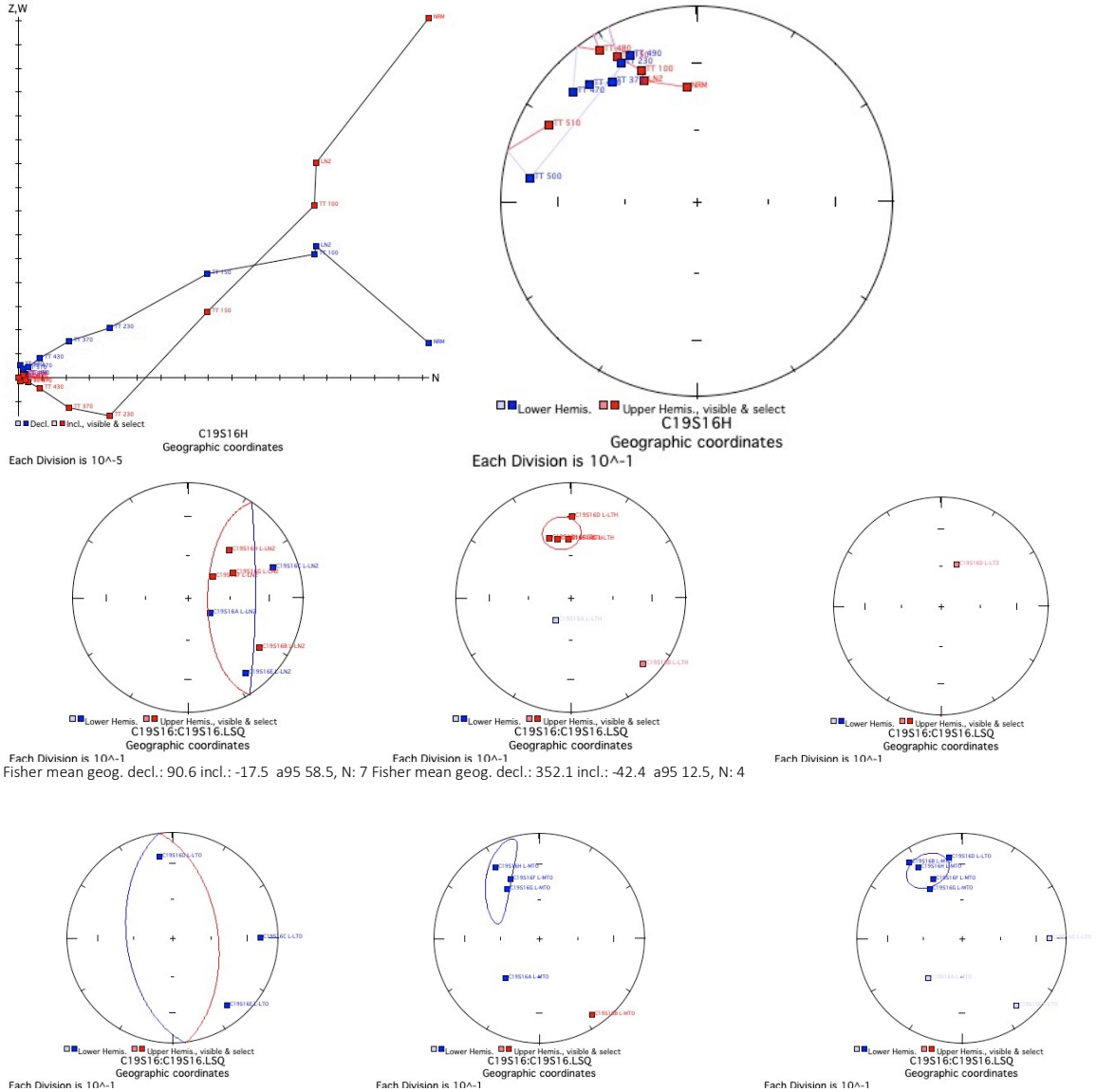

Figure 20: Representative demagnetization behavior from site C19S16. Starting from top row left to right: (a) Zijderveld diagram of sample C19S16H, showing three components of the NRM. (b) Equal-area stereonet diagram of sample C19S016H. (c) Equal-area plot of the LN2 component with Fisher statistics 95% confidence ellipse. (d) Equal-area plot of the LTH component with Fisher statistics 95% confidence ellipse. (e) Equal-area plot of the LT2 component (f) Equal-area plot of the LTO component with Fisher statistics 95% confidence ellipse (g) Equal-area plot of the MTO component with Bingham statistics 95% confidence ellipse (h) Equal-area plot of the MTO and LTO components combined with Fisher statistics 95% confidence ellipse.

C19S17:

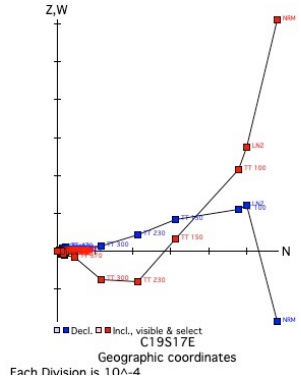

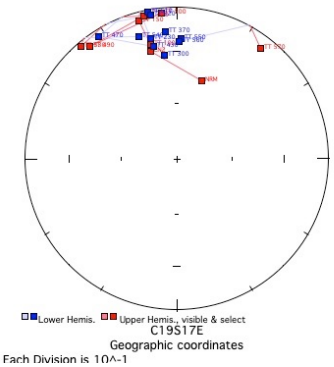

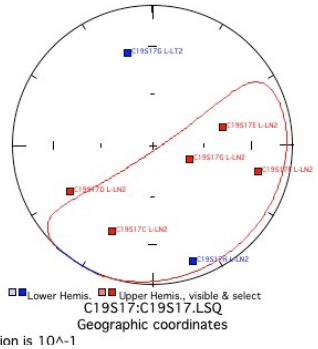

Bingham mean geog. decl.: 149.1, incl.: -46.8 a95 40.2, 81.5 N: 7

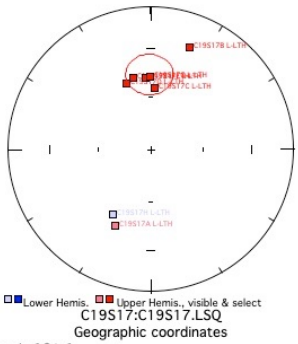

Fisher mean geog. decl.: 359.0, incl.: -46.1 a95 12.5, N: 6

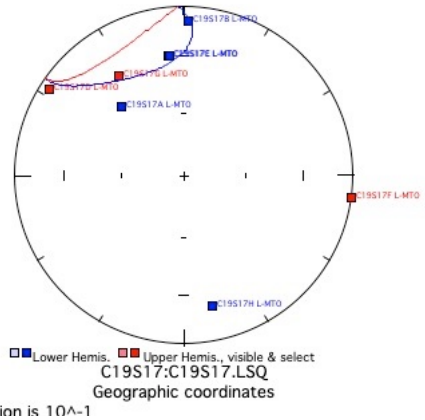

Bingham mean geog. decl.: 333.6, incl.: 8.6 a95 24.2, 31.5, N: 8

Figure 21: Representative demagnetization behavior from site C19S17. Starting from top row left to right: (a) Zijderveld diagram of sample C19S17E, showing three components of the NRM. (b) Equal-area stereonet diagram of sample C19S017E. (c) Equal-area plot of the LN2 component with Bingham statistics 95% confidence ellipse. (d) Equal-area plot of the LTH component with Fisher statistics 95% confidence ellipse. (e) Equal-area plot of the MTO component with Bingham statistics 95% confidence ellipse

Dordabis:

Table 2: Paleomagnetic site information for the Dordabis Sequence (Bitterwater Member)

Name	Location	N	Lithology	Susceptibility (SI)	Width (m)	Altitude(m)	RHS(°)/DIP(°)	Notes
V19D01	22.87706°S 17.79556°E	7	Pale purple/pink quartzite	N/A	N/A	1530 m	60°/78° (Bedding) 60/67 (middle of bed)	
V19D02	22.87788°S 17.79607°E	8	Rare-flattenned amygdales, mafic basalt	260-490*10e-6	N/A	1521 m	75°/95°	
V19D03	22.87864°S 17.79675°E	6	Mafic basalts	990-330*10e-6	N/A	1513 m	68°/89°	Cleavage visible
V19D04	22.87906°S 17.79690°E	8	Flattenned amygdules in greenish meta-basalt	300-498*10e-6	N/A	1509	50°/83°	Southeast from anticline
V19D05	22.85007°S 17.81060°E	8	Amygdaloidal basalt	123-435*10-e6	N/A	N/A	280°/43°	Samples drill red/purple
V19D06	22.84866°S 17.81120°E	7	Pink/purple quartzite	37-55*10e-6	N/A	1547m	320°/42°	
V19D07	22.84553°S 17.80849°E	8	Metabasalt with chlorite and epidote, with cm/dm thick amygdaloidal layers	559-843*10e-6	N/A	1567 m	290°/39°	
V19D08	22.84539°S 17.80811°E	8	Metabasalt with amygdaloidal layers	512-1400*10e-6	N/A	1547 m	290°/55°	
V19D09	22.84514°S 17.80789°E	8	Lower of two flows distinguished by a 60m amygdaloidal flow top.	328-1200*10e-6	N/A	1544 m	290°/55°N	
V19D10	22.84514°S 17.80789°E	8	Upper of two amygdaloidal flows	669-984*10e-6	N/A	1544 m	285°/55N	

D01: Seven samples were drilled from a pale purple/pink quartzite. All NRMs of the samples displayed a magnetic moment of 10-5 emu. The samples developed a low thermal component (LTH) from either the NRM to 150°C or 580°C with a shallow, upwards southwest direction. The samples with the lower temperature LTH ending at 100°C developed a secondary low thermal component starting from 230°C or 300°C and ending at 580°C (Samples A, B, F and C).

There was no consistent demagnetization direction observed within the LT2 components. From 600°C onwards, all samples displayed a clear high-temperature decay-to-origin component that was stable through the hematite unblocking temperature and continued through to 688°C (HTO). All samples produced a precise cluster of HTO poles that consisted of shallow and downwards south-southwest directions. This site was then able to be used to calculate a VGP. (Figure 22)

D02: Eight samples were drilled from mafic basalts, that produced red fluids when drilled. All NRMs had magnetic moments of ca. 10e-3 emu. The samples produced messy data that was unable to be fitted with a line or plane until high temperatures. As a result, no low-temperature directions were recorded, apart from sample C which produced a well-defined linear component of demagnetization from the LN2 step to the origin. All other samples produced a clear component of demagnetization, starting from temperatures of either 580°C, 582°C, 610°C or 640°C and continuing to temperatures held by hematite of either 680°C or 685°C through the origin (HTO). All directions recorded were upwards shallow south-southwest, occurring in a tight cluster. This site was then able to be used to calculate a VGP. (Figure 23)

D03: Seven samples were drilled from the Bitterwater volcanics that produced red fluids when drilled. Magnetic moments were measured to be ca. 10e-3 emu for all samples. The data produced at low temperatures was too messy to determine a line of best fit or a magnetic direction, thus only the distinct high temperature to origin component (HTO) was measured for all samples. The HTOs demagnetized and were stable between 586°C, 610°C or 640°C to an endpoint of 690°C. All directions from the HTOs were shallow upwards and south-southwest, enabling a VGP to be calculated for this site. (Figure 24)

D04: Eight samples were extracted from greenish meta-basalt with flattened amygdules. All magnetic moments of NRMs were ca. 10-4 emu. At low temperatures, the data was too

messy to fit either a line or plane, with the exception of samples B and E that displayed low-temperature thermal components from the magnetite, both with a shallow southeast direction. All samples displayed a clear high-temperature to origin component (HTO) from 578°C to 680°C or 685°C that remained stable through the unblocking temperature of haematite. The HTOs of the samples produced a tight cluster of shallow southwest directions that were used to determine a VGP. (Figure 25)

D05: Eight samples were collected from amygdaloidal basalt that produced red and purple fluids when drilled. For all NRMs, the magnetic moment was 10e-3 emu. Due to messy low-temperature data, it was only possible to identify lines of best fit for high temperature to origin components (HTO), that were stable through hematite. The HTOs demagnetized for all samples, producing a tight cluster of steep, upwards, east southeast directions, between steps of 610°C and 680°C. As a result, site D05 could be used to calculate a VGP. (Figure 26)

V19D01:

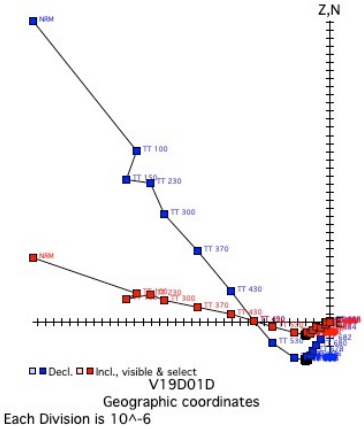

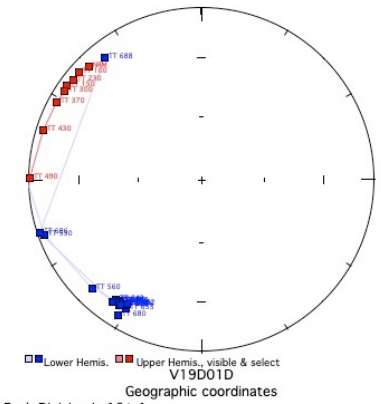

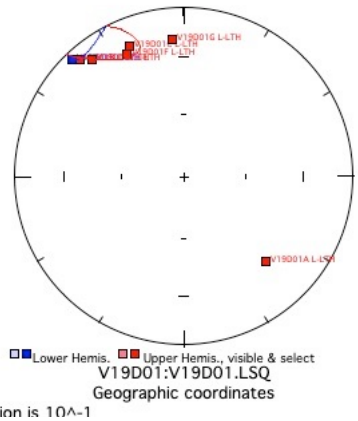

Bingham mean geog. decl.: 328.5, incl.: -7.9 a95 8.1, 18.5, N:7

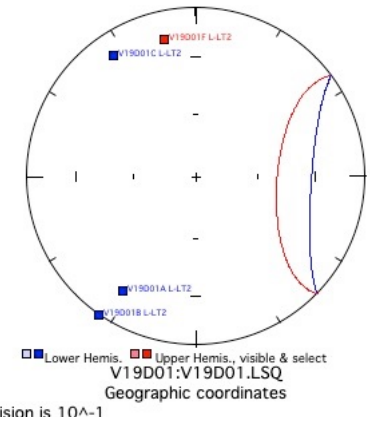

Fisher mean geog. decl.: 273.7, incl.: 9.1 a95 138.8, N:4

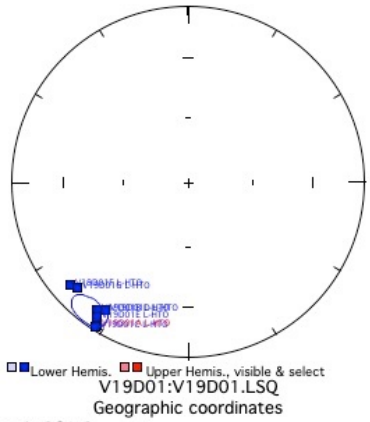

Fisher mean geog. decl.: 217.6, incl.: 8.9 a95 7.3, N:7

Figure 22: Representative demagnetization behavior from site V19D01. Starting from top row left to right: (a) Zijderveld diagram of sample V19D01D, showing two components of the NRM. (b) Equal-area stereonet diagram of sample V19D01D. (c) Equal-area plot of the LTH component with Bingham statistics 95% confidence ellipse. (d) Equal-area plot of the LT2 component with Fisher statistics 95% confidence ellipse. (e) Equal-area plot of the HTO component with Fisher statistics 95% confidence ellipse

V19D02:

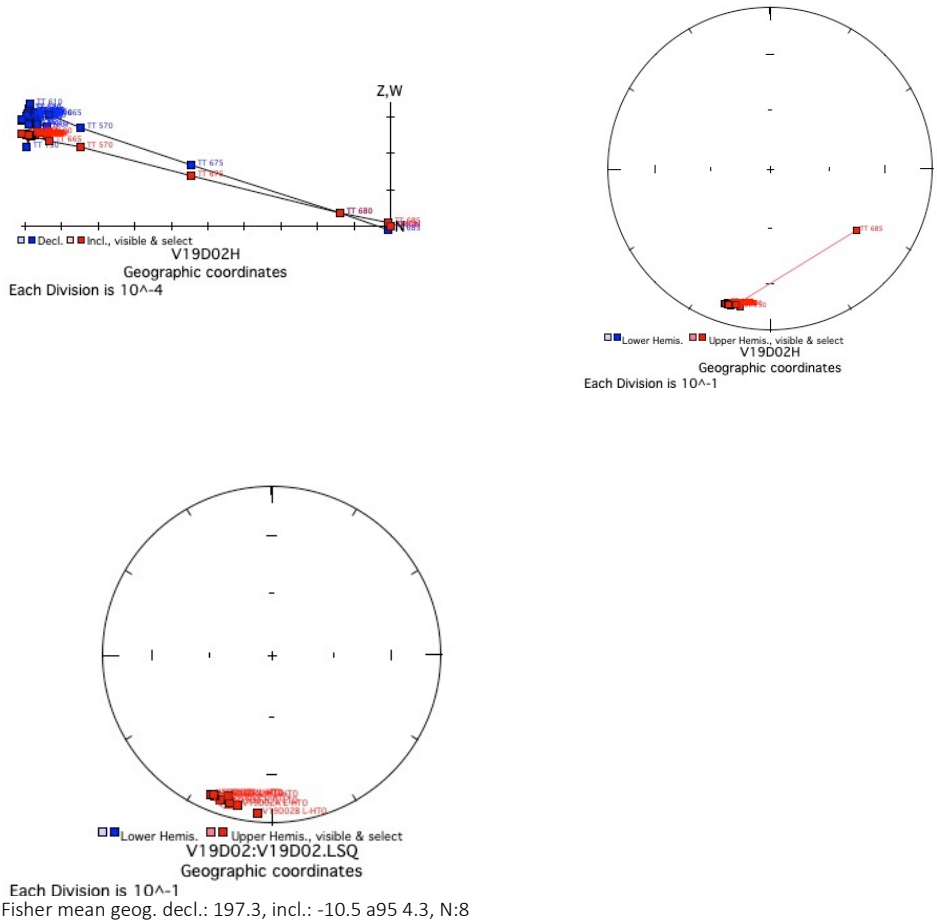

Figure 23: Representative demagnetization behavior from site V19D02. Starting from top row left to right: (a) Zijderveld diagram of sample V19D02H, showing one component of the NRM. (b) Equal-area stereonet diagram of sample V19D02H. (c) Equal-area plot of the HTO component with Fisher statistics 95% confidence ellipse.

V19D03:

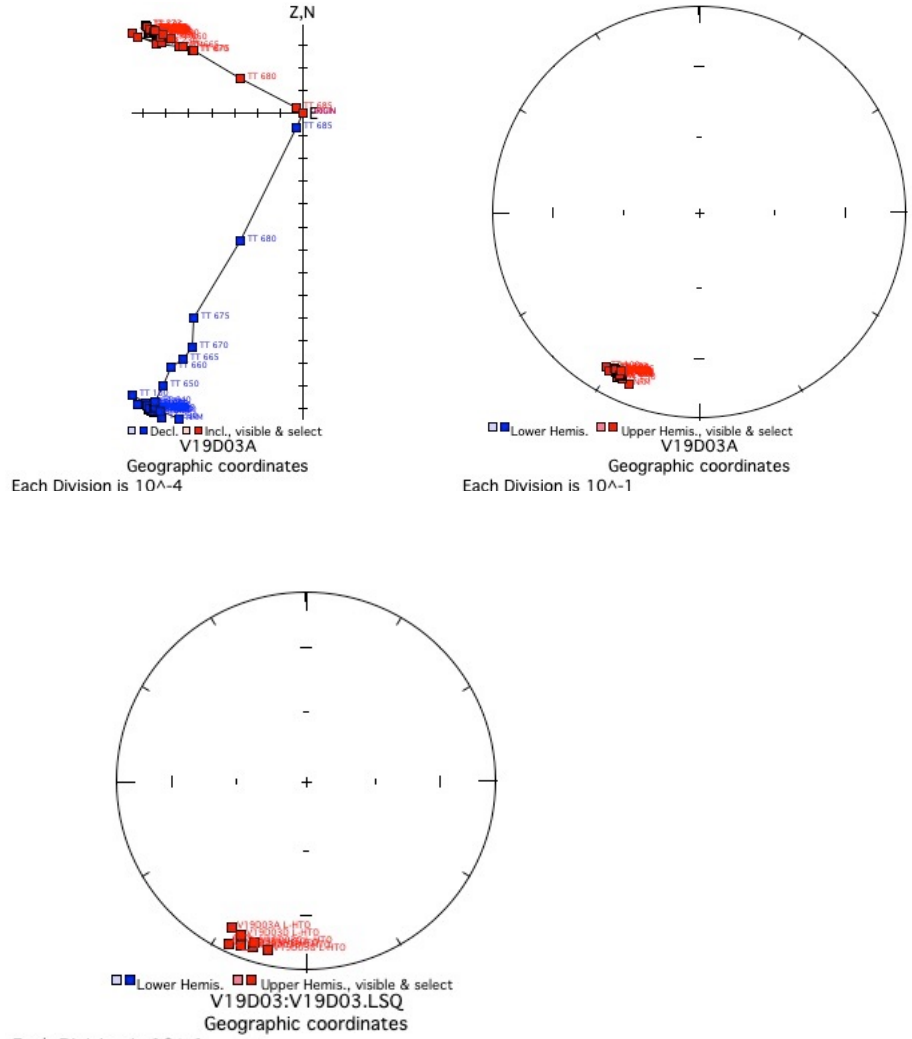

Figure 24: Representative demagnetization behavior from site V19D03. Starting from top row left to right: (a) Zijderveld diagram of sample V19D03A, showing one component of the NRM. (b) Equal-area stereonet diagram of sample V19D03A. (c) Equal-area plot of the HTO component with Fisher statistics 95% confidence ellipse.

V19D04:

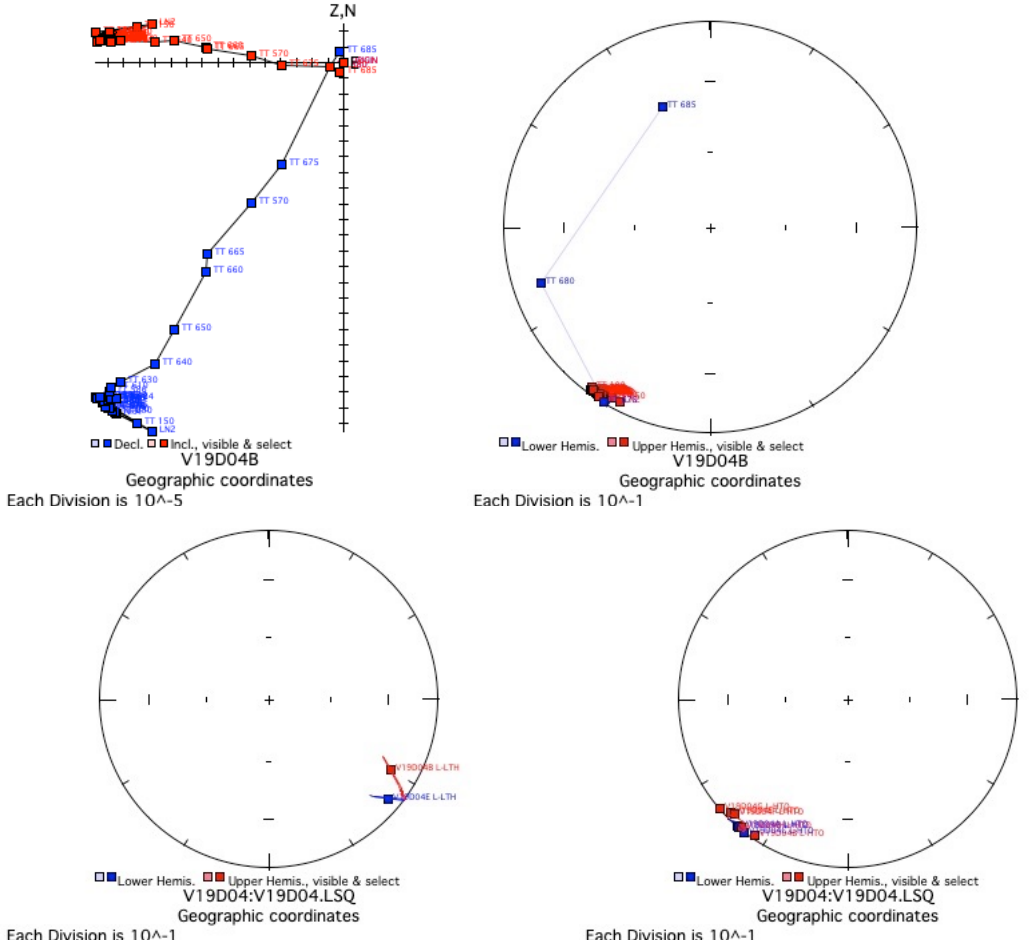

Bingham mean geog. decl.: 124.8, incl.: -4.4 a95 0.2, 24.6, N:2

Fisher mean geog. decl.: 221.8, incl.: -1.7 a95 3.7, N:8

Figure 25: Representative demagnetization behavior from site V19D04. Starting from top row left to right: (a) Zijderveld diagram of sample V19D04B, showing one component of the NRM. (b) Equal-area stereonet diagram of sample V19D04B. (c) Equal-area plot of the LTH component with Bingham statistics 95% confidence ellipse. (d) Equal-area plot of the HTO component with Fisher statistics 95% confidence ellipse.

V19D05:

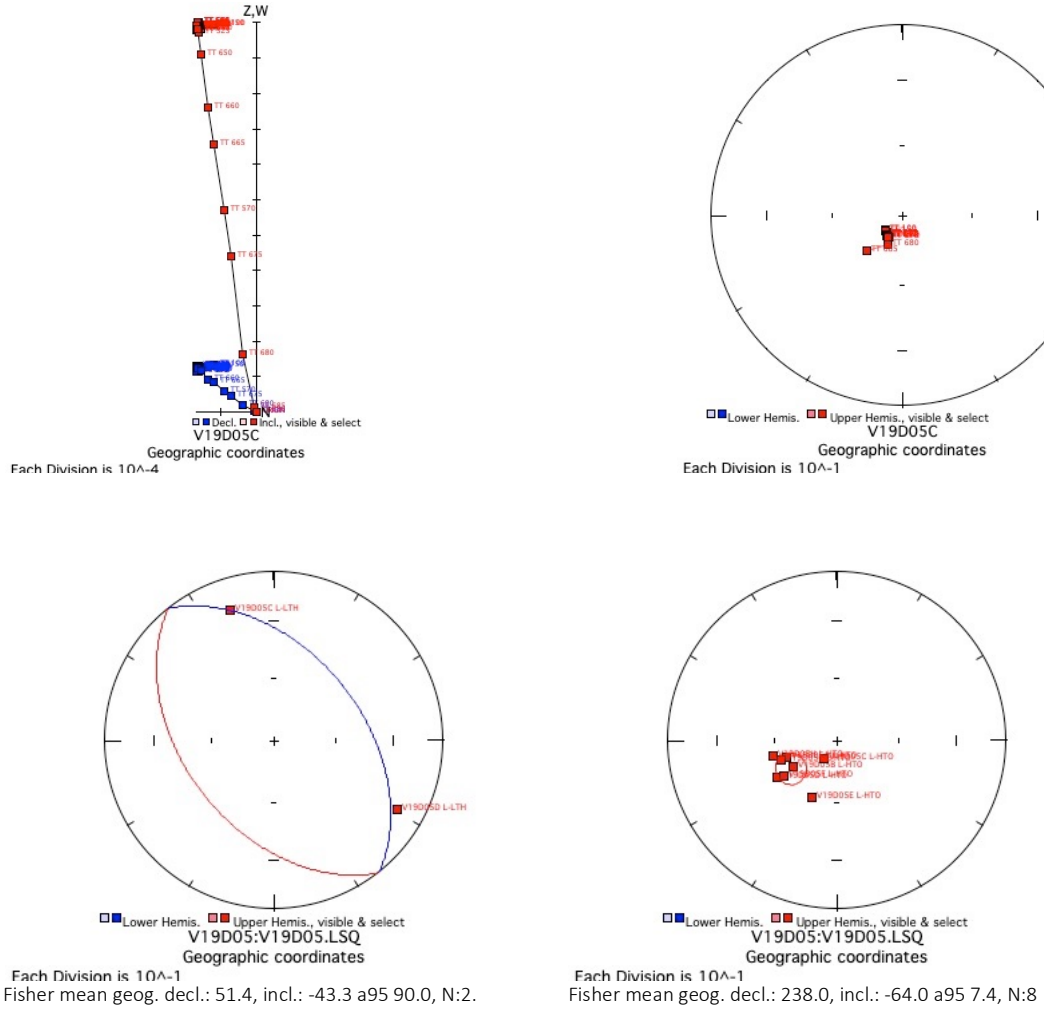

Figure 26: Representative demagnetization behavior from site V19D05. Starting from top row left to right: (a) Zijderveld diagram of sample V19D05C, showing one component of the NRM. (b) Equal-area stereonet diagram of sample V19D05C. (c) Equal-area plot of the LTH component with Fisher statistics 95% confidence ellipse. (d) Equal-area plot of the HTO component with Fisher statistics 95% confidence ellipse.

D06: Seven samples were drilled from pinkish-purple quartzite. All NRMs had magnetic moments of ca. 10e-4 emu. Two samples displayed a low-temperature thermal component (LTH) from 100°C to 300°C (A), or 230°C to 530°C (D). However, both of these samples produced contrasting upward LTH directions. All samples produced well defined high-temperature components (HTO) that decayed to the origin, starting the earliest at sample A at 370°C and starting for all other samples at 470°C (B), 560°C (D), 615 °C (C), and at step 673°C (E, F, and G). All samples remained stable at the hematite unblocking temperature and continued to decay until step 686°C. The HTOs produced a precise cluster of steep, upward, southeast directions. Due to the low a95 error of 3.5 degrees, a VGP is able to be calculated from this site. (Figure 27)

D07: Eight samples were drilled out of a metabasalt with chlorite and epidote present, as well as thick amygdaloidal layers. All NRMs produced magnetic moments of ca. 10e-4 emu. Low-temperature components were seen in 5 samples (A, B, D, E, and G), with demagnetization occurring between the NRM step and at either the 150°C, 500°C, or 586°C steps. However, the LTH components did not produce consistent directions. Samples E and G also displayed a second low thermal (LT2) component between steps 230°C (E) or 500°C (G), until step 578°C (G) and 586°C (E). However, both LT2 components produced contrasting magnetic directions. 3 samples (C, F, and H) produced a low-temperature decay directly to the origin (LTO), with a clear line of demagnetization occurring until 640°C or 650°C and through the origin. Although all LTO components produced a generally shallow southeast direction, there were large differences in the sample's declinations. High-temperature decay to origin components were observed in samples A, B, D, E, and G, with demagnetization occurring from step 500°C, 582°C, or 610°C, until steps 640°C or 650°C. All samples generally displayed directions ranging from

south to south-west, although due to the large a95 error a VGP was not calculated for this pole. (Figure 28)

D08: 8 samples were collected from a metabasalt that potentially was produced from the same flow as V19D07. The NRMs all had magnetic moments of ca. 10e-3 emu. All samples displayed prominent low-temperature thermal components that started from the NRM step to 230°C and typically ended at one of the steps between the 500°C to 600°C range. All LTHs produced generally westward oriented directions, although all had varying declinations and steepness. Two samples (G and H) produced secondary low-temperature thermal components (LT2) between the 230°C step and the 565°C step (G) or the 575°C step (H). However, both LT2 components produced different directions making one unable to identify a singular magnetic component. Sample A produced a low-temperature direct decay to the origin, with a downwards shallow north-northwest direction. The rest of the samples produced a high-temperature decay to the origin (HTO) starting at steps ranging from 570°C to 580°C with a well-defined decay until either the 640°C or 650°C step. The HTOs were precisely clustered at a moderately shallow, upwards south-southwest declination. Due to the tight cluster of the HTOs a VGP is calculated from this pole. (Figure 29)

D09: Eight samples were extracted from the base of an amygdaloidal basalt layer, as the lower member of two flows that were separated by an amygdaloidal flow top. The NRMs all had magnetic moments of ca. 10e-3 emu. In general, most samples displayed two distinct NRM components. Low thermal components were generally observed in samples at temperatures around 150°C until temperatures of around 370°C, or between 535°C -555°C. No consistent direction was observed within the LTH components of the samples. Sample G also displayed a secondary low thermal component (LT2) from step 150°C to 573°C that produced a shallow,

downwards east-northeast direction. A well-defined high-temperature decay to origin (HTO) was observed in all samples, generally starting at step 580°C or 610°C and demagnetizing until step 670°C or 675°C. The HTOs produced a tight cluster of directions giving an overall direction of moderately shallow, upwards south-southwest. This site is able to be used to calculate a VGP. (Figure 30)

D10: Eight samples were extracted from the upper of the two flows located at D09. The NRMs all had magnetic moments of ca. 10-3 emu. Low-temperature thermal components (LTH) were observed across all samples, generally starting at steps ranging from LN2 to 230°C, and displaying a well-defined decay until steps 500 °C, 515°C, 550°C, 586°C or 630°C. The LTH components generally displayed a downwards east direction, although with varying amounts of inclination. Two samples displayed a secondary low-temperature thermal direction (LT2) (samples A and F), decaying from 550°C (A) or 555°C (F). However, neither sample A nor sample F displayed similar LT2 directions. All samples displayed a well-defined high-temperature component (HTO) that decayed to the origin starting at 610°C, 630°C, or 660°C and continued to decay linearly until the 675°C step. The HTO directions were all moderately shallow, upwards, south-southwest with the exception of the sample H anomaly; H was subsequently removed from the Fisher statistics 95% confidence ellipse. Overall the tight clustering of the HTO components indicate a VGP can be calculated from this site. (Figure 31)

V19D06:

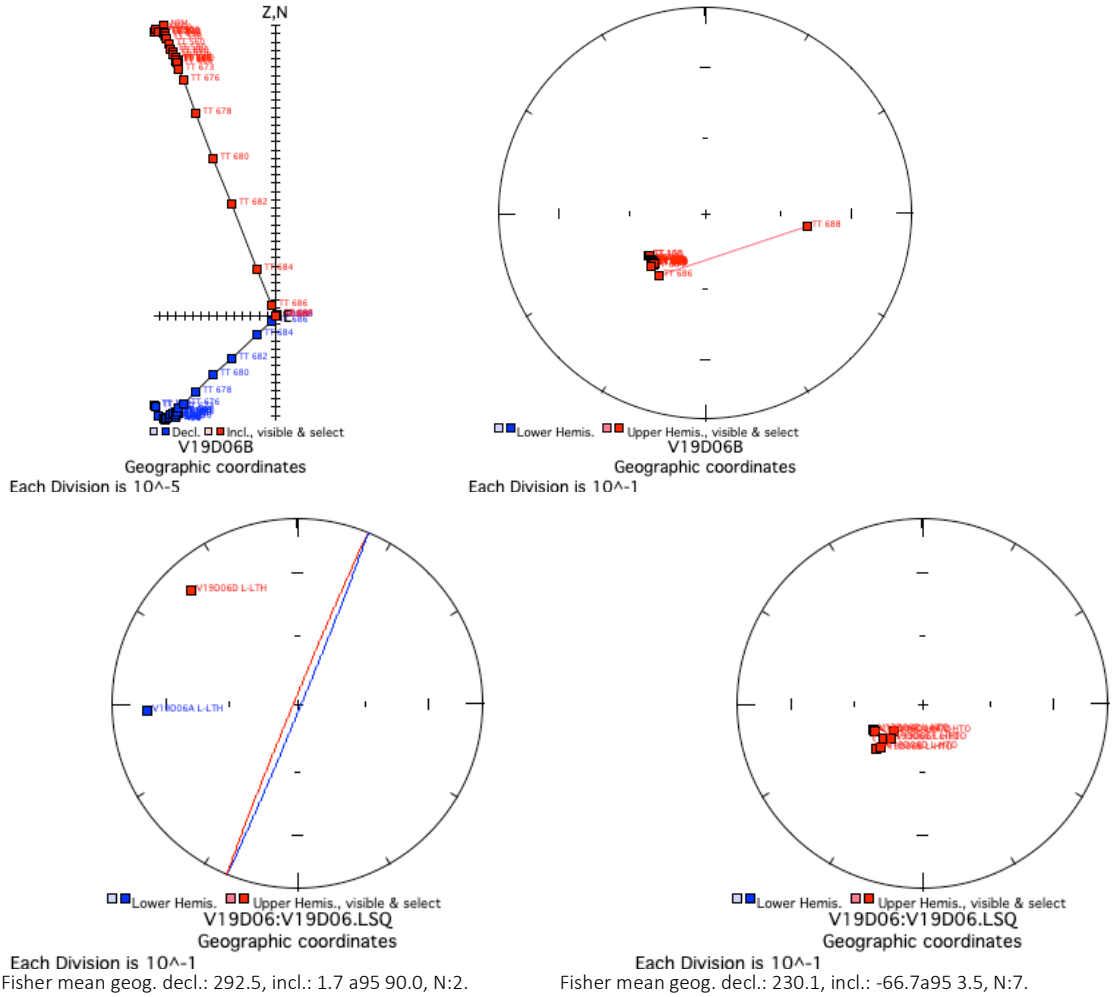

Figure 27: Representative demagnetization behavior from site V19D06. Starting from top row left to right: (a) Zijderveld diagram of sample V19D06B, showing one component of the NRM. (b) Equal-area stereonet diagram of sample V19D06B. (c) Equal-area plot of the LTH component with Fisher statistics 95% confidence ellipse. (d) Equal-area plot of the HTO component with Fisher statistics 95% confidence ellipse.

V19D07:

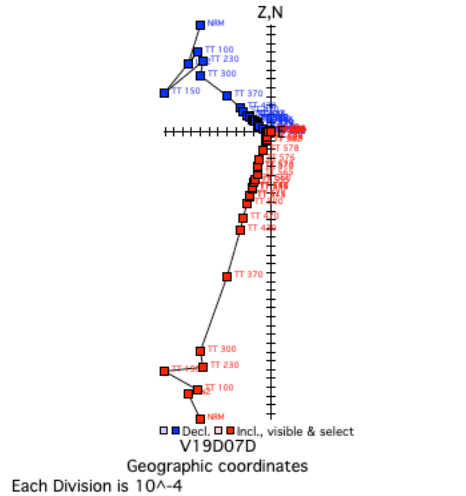

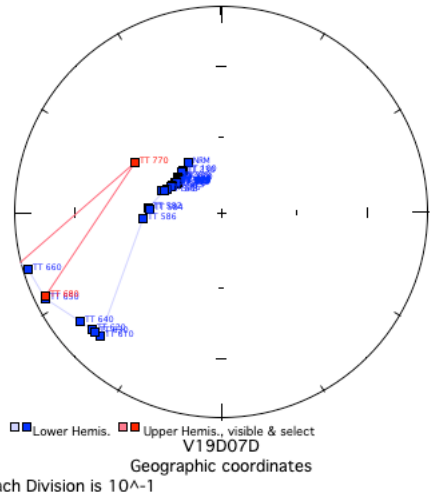

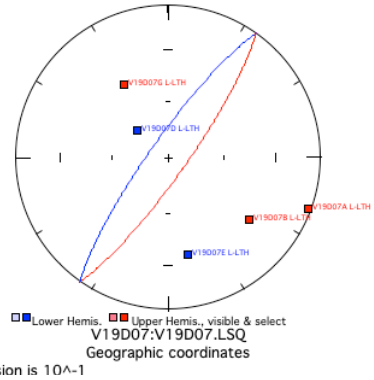

Fisher mean geog. decl.: 125.4, incl.: 9.8 a95 90.0, N:5

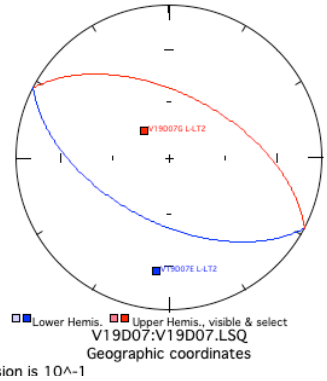

Fisher mean geog. decl.: 207.4, incl.: -34.6 a95 90.0, N:2

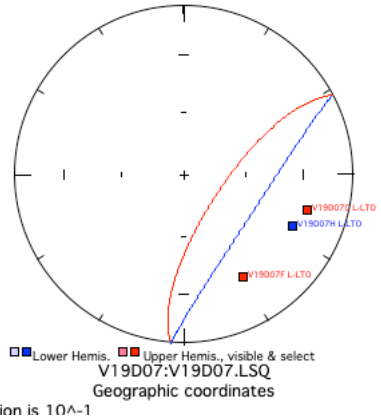

Fisher mean geog. decl.: 123.1, incl.: -9.9 a95 61.7, N:3

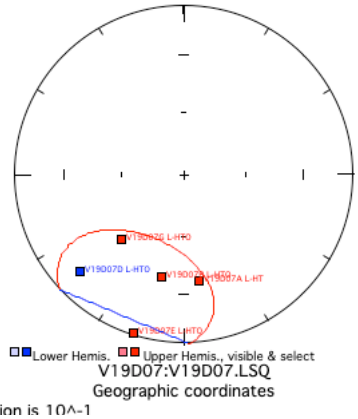

Fisher mean geog. decl.: 202.7, incl.: -23.0 a95 33.0, N:5

Figure 28. Representative demagnetization behavior from site V19D07. Starting from top row left to right: (a) Zijderveld diagram of sample V19D07D, showing two components of the NRM. (b) Equal-area stereonet diagram of sample V19D07D. (c) Equal-area plot of the LTH component with Fisher statistics 95% confidence ellipse. (d) Equal-area plot of the LT2 component with Fisher statistics 95% confidence ellipse. (e) Equal-area plot of the LTO component with Fisher statistics 95% confidence ellipse. (f) Equal-area plot of the HTO component with Fisher statistics 95% confidence ellipse.

V19D08:

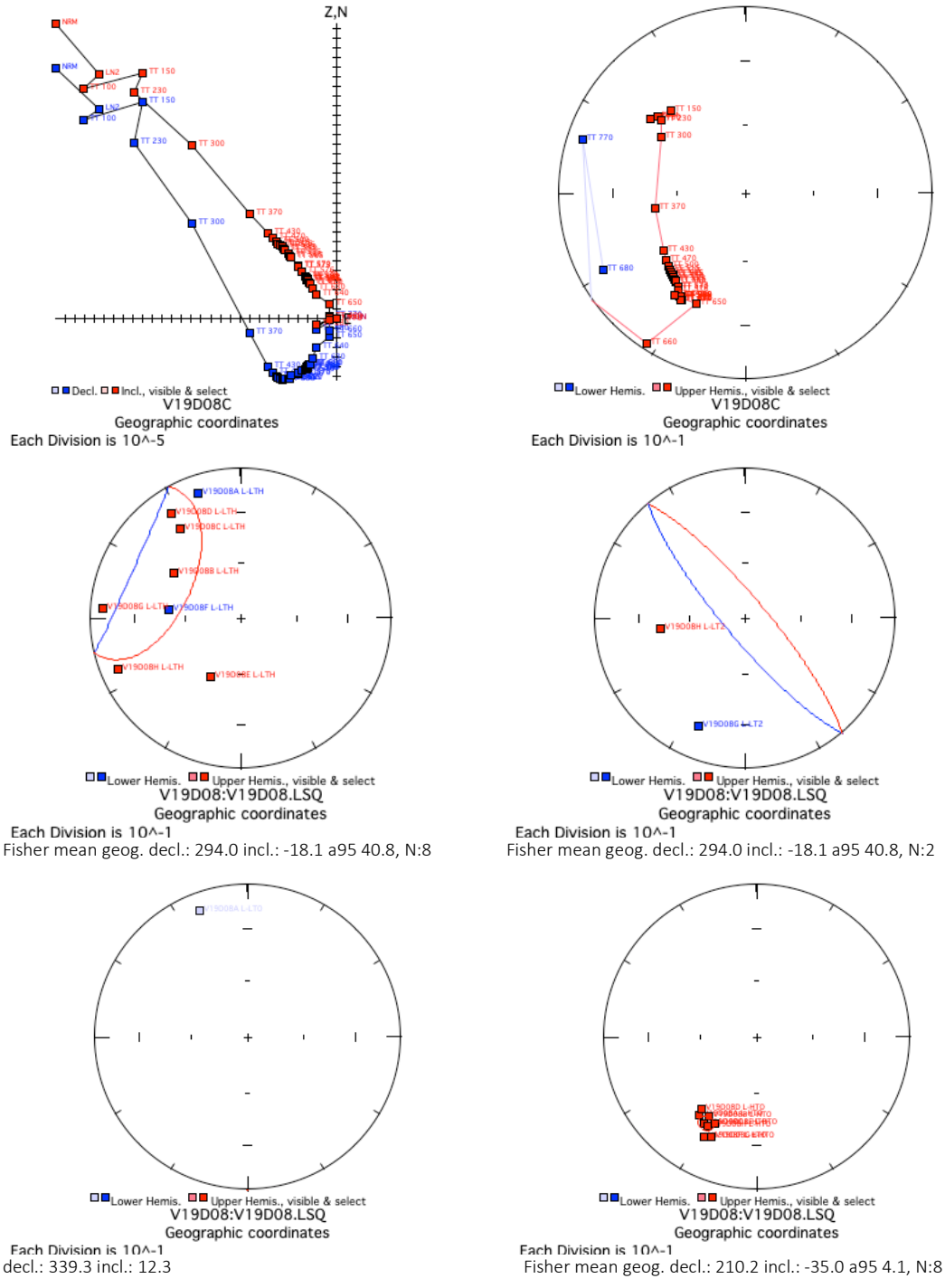

Figure 29. Representative demagnetization behavior from site V19D08. Starting from top row left to right: (a) Zijderveld diagram of sample V19D08C, showing two components of the NRM. (b) Equal-area stereonet diagram of sample V19D08C. (c) Equal-area plot of the LTH component with Fisher statistics 95% confidence ellipse. (d) Equal-area plot of the LT2 component with Fisher statistics 95% confidence ellipse. (e) Equal-area plot of the LTO component. (f) Equal-area plot of the HTO component with Fisher statistics 95% confidence ellipse.

V19D09:

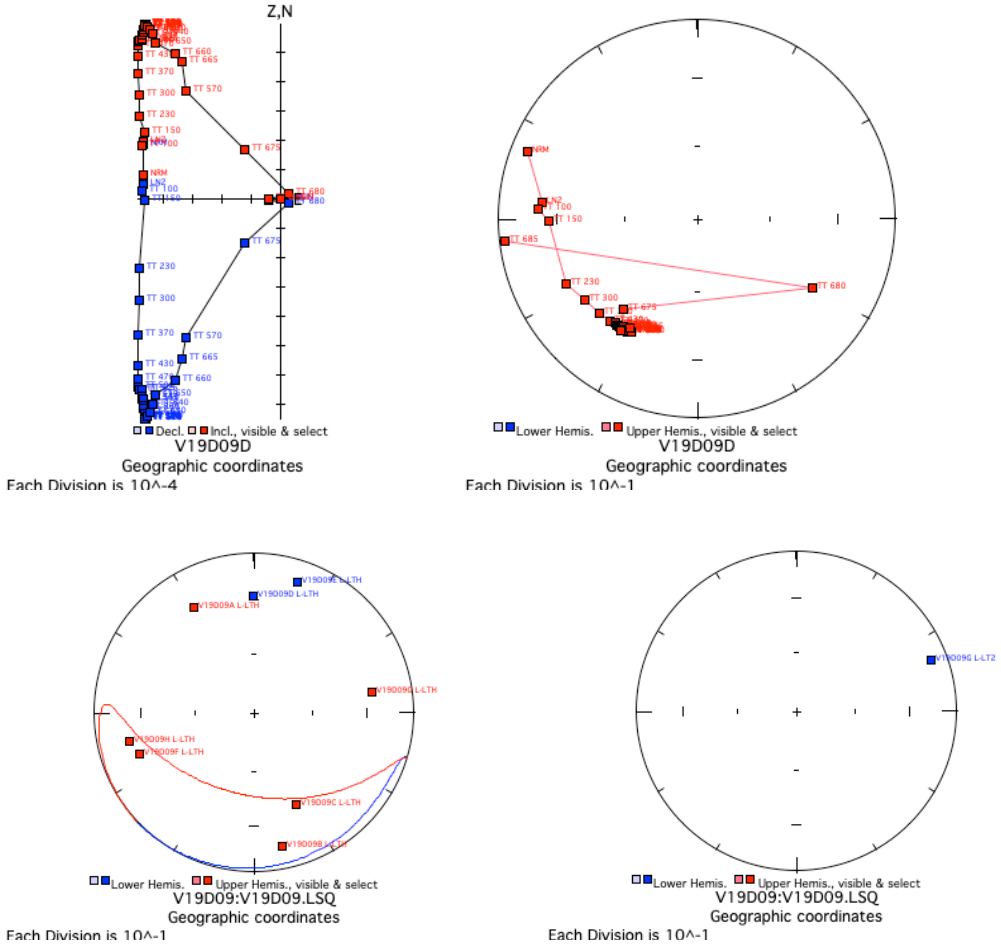

Figure 30: Representative demagnetization behavior from site V19D09. Starting from top row left to right: (a) Zijderveld diagram of sample V19D09D, showing two components of the NRM. (b) Equal-area stereonet diagram of sample V19D09D. (c) Equal-area plot of the LTH component with Fisher statistics 95% confidence ellipse. (d) Equal-area plot of the LT2 component. (e) Equal-area plot of the HTO component.

V19D10:

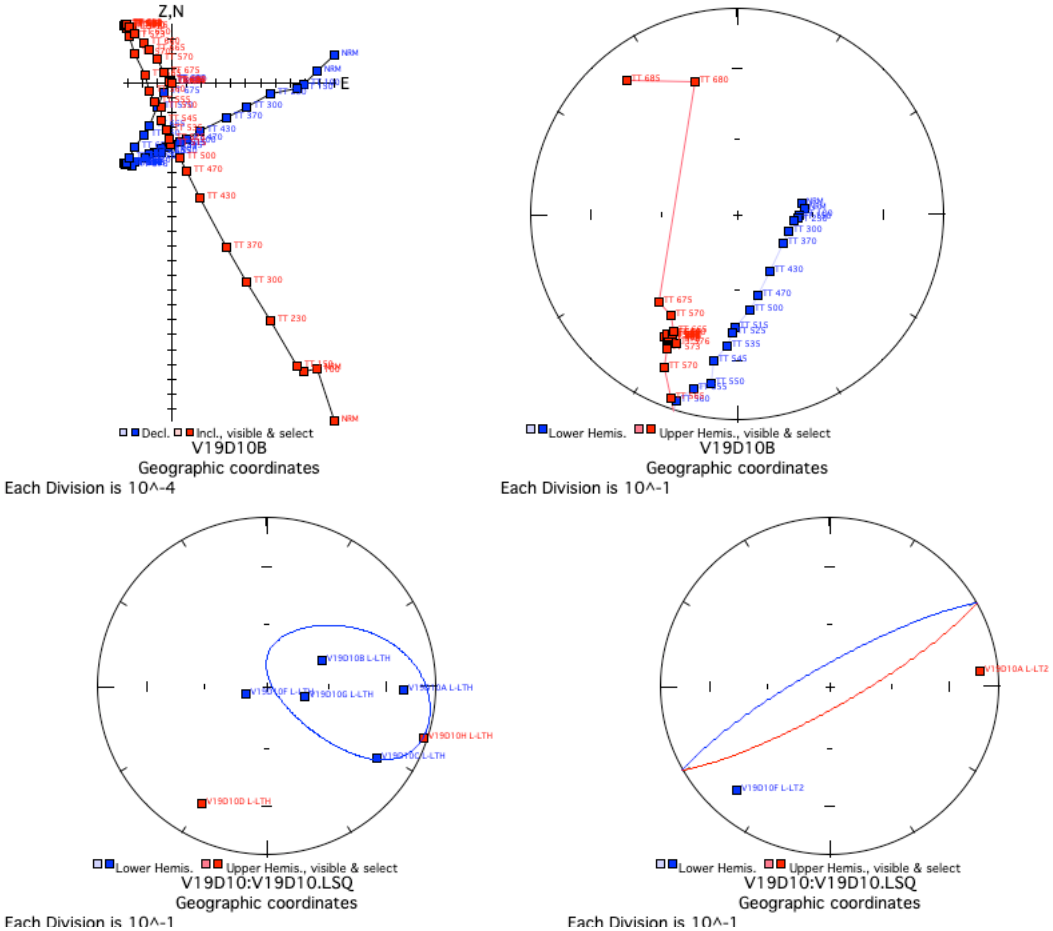

Bingham mean geog. decl.: 91.6, incl.: 46.3 a95 26.7, 45.7, N: 7. Fisher mean geog. decl.: 150.4, incl.: 10.0 a95 90.0, N: 2

Fisher mean geog. decl.: 209.9, incl.: -35.6 a95 1.9, N: 7

Figure 31: Representative demagnetization behavior from site V19D10. Starting from top row left to right: (a) Zijderveld diagram of sample V19D10B, showing two components of the NRM. (b) Equal-area stereonet diagram of sample V19D10B. (c) Equal-area plot of the LTH component with Bingham statistics 95% confidence ellipse. (d) Equal-area plot of the LT2 component with Fisher statistics 95% confidence ellipse. (e) Equal-area plot of the HTO component with Fisher statistics 95% confidence ellipse

Uisib:

Table 3: Paleomagnetic Site information for the Uisib River Valley

Name	Location	N	Lithology	Susceptibility (SI)	Width (m)	Altitude(m)	RHS(°)/DIP(°)	Notes
C19U1	23.13403°S 17.20060°	8	Mafic dyke intruding auegn gneiss	630-13,500*10e-6	14m	1467 m	270° strike	Low outcrop
C19U2	23.13111°S 17.19835°E	8	Medium-grained diabase	7740923*10e-6	9m	1467 m	270° strike	Greenish drilling mud

U1: Eight samples were drilled from a mafic dyke located on a low outcrop in the Uisib River. All NRMs displayed a magnetic moment of ca. 10e-2 emu, apart from sample H which displayed a moment of ca. 10e-2 emu. A low-temperature thermal component (LTH) was removed between steps 100°C or 150°C until 515°C to 560°C. Eastwards directions are produced, all with varying declinations. Some samples also displayed a secondary low-temperature component (such as H), which demagnetized from 550°C until 660°C. Well-defined high-temperature decay to the origin was seen across all samples, apart from A which displayed low-temperature decay to the origin (LTO). Due to the strong magnetization, it was evident that the majority of U1 sample sites had been struck by lightning. However, a cluster of points (A, F and H) displayed similar decay-to-origin directions and seemed to be less strongly magnetized (10e-4 emu) than the other samples. As a result in our fisher statistics ellipse, we only includeed A, F, and H. The a95 error was above the cutoff of 20 degrees, but we excuse this as only 3 points are used to calculate the mean direction, with a similar direction to that of the Bitterwater samples. As a result, one is able to calculate a VGP from this site. (Figure 32)

U2: 8 samples were extracted from a medium-grained diabase dyke in the Uisib River Valley. The NRMs had magnetic moments of ca. 10e-6 emu, although the data was extremely

noisy and crashed at low temperatures, making it difficult to identify any lines of best fit. Prominent LN2 components were seen in samples B, E, C, and G, although no consistent direction was seen. Poorly-defined low-temperature decay to origin components was present (LTO), with the demagnetization occurring between steps NRM or LN2 and 230°C or 470°C. The LTO directions produced a cluster of points that represents the present-day overprint (shallow north-northwest up). Overall, due to the large amounts of noise and error produced in this dataset, a VGP was not calculated from this site. (Figure 33)

C19U1:

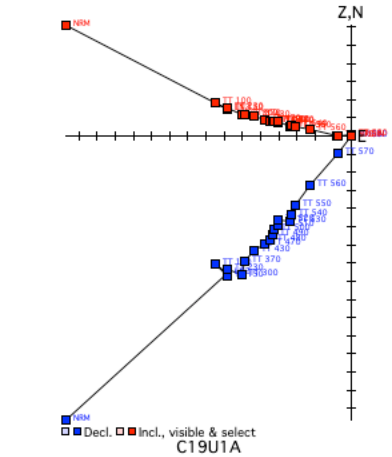

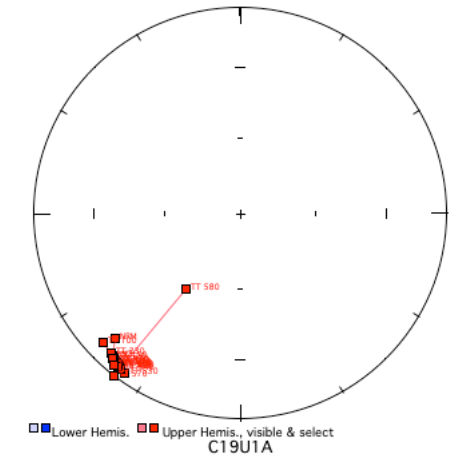

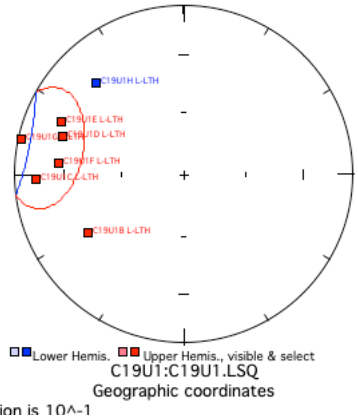

Fisher mean geog. decl.: 280.9, incl.: -15.5 a95 23.5, N: 7

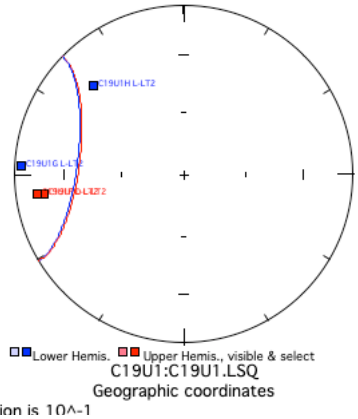

Fisher mean geog. decl.: 276.8, incl.: 0.6 a95 37.5, N: 4

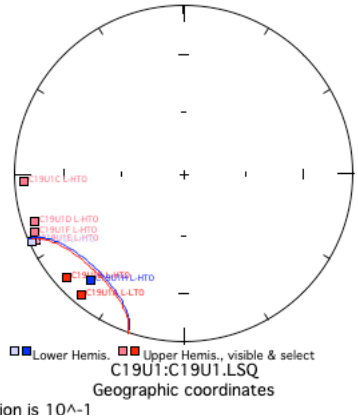

Fisher mean geog. decl.: 223.3, incl.: 0.7 a95 24.0, N: 3

Figure 32. Representative demagnetization behavior from site C19U1. Starting from top row left to right: (a) Zijderveld diagram of sample C19U1A, showing two components of the NRM. (b) Equal-area stereonet diagram of sample C19U1A. (c) Equal-area plot of the LTH component with Fisher statistics 95% confidence ellipse. (d) Equal-area plot of the LT2 component with Fisher statistics 95% confidence ellipse. (e) Equal-area plot of the HTO and LTO components with Fisher statistics 95% confidence ellipse.

C19U2:

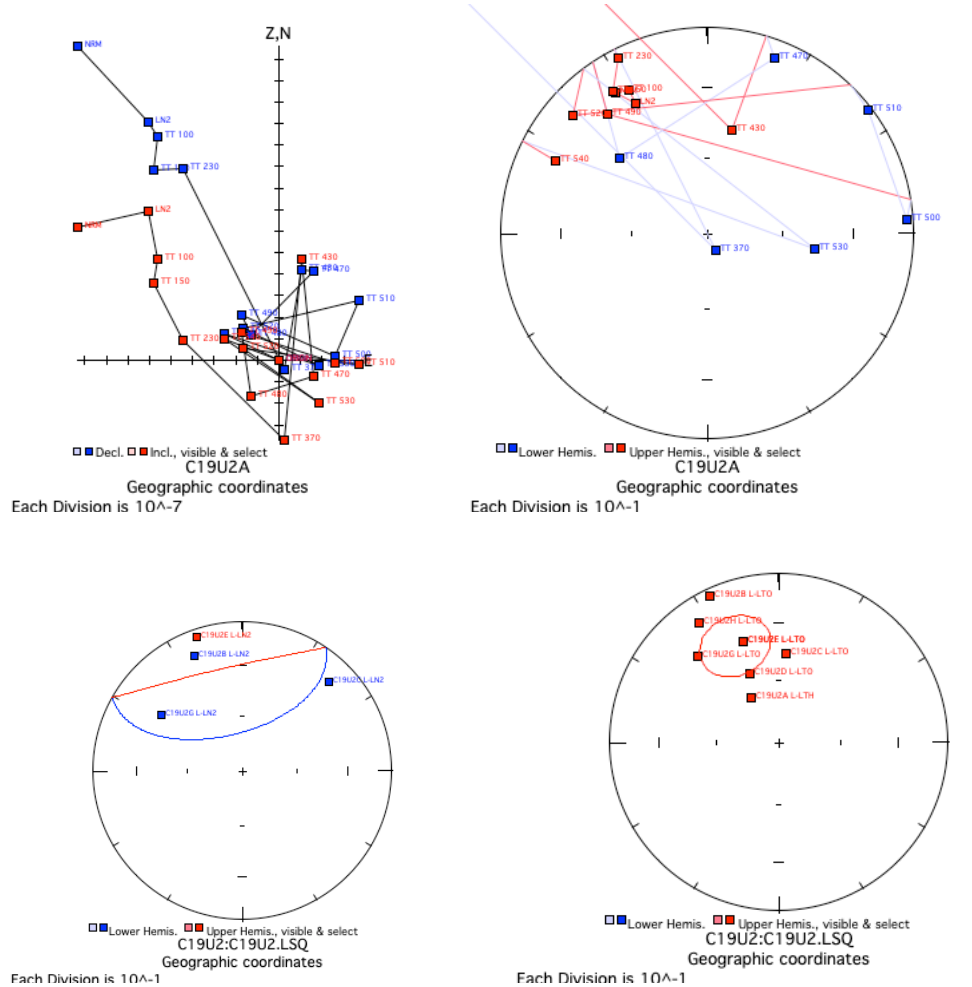

Fisher mean geog. decl.: 346.8, incl.: 19.3 a95 50.2, N: 4 Fisher mean geog. decl.: 335.7, incl.: -36.9 a95 15.8, N: 8

Figure 33. Representative demagnetization behavior from site C19U2. Starting from top row left to right: (a) Zijderveld diagram of sample C19U2A, showing two components of the NRM. (b) Equal-area stereonet diagram of sample C19U2A. (c) Equal-area plot of the LN2 component with Fisher statistics 95% confidence ellipse. (d) Equal-area plot of the LTO component with Fisher statistics 95% confidence ellipse.

Rehoboth:

Table 4: Paleomagnetic site information for the Rehoboth Dykes

Name	Location	N	Lithology	Susceptibility (SI)	Width (m)	Altitude(m)	RHS(°)/DIP(°)	Notes
C19R1	23.295325°S 17.02952°E	8	Medium grained dolerite	1200-2100*10e-6	10 m	N/A	280°/200°	
C19R2	23.29474°S 17.02701°E	8	Medium grained dolerite.	1500-6640*10e-6	N/A	N/A	112°/33°	

R1: Eight samples were drilled from a medium-grained dolerite dyke. The NRMs displayed magnetic moments of ca. 10e-3 emu. 2 samples (F and H), displayed prominent LN2 components that occurred with a shallow downwards southeast direction. Samples A, D, E, F, G, and H, all produced well-defined low-temperature thermal components (LTH) where the magnetism was removed between either the NRM or 100°C step, until the 230°C steps. No consistent LTH direction was observed. 2 samples displayed secondary thermal components (LT2) between steps 300°C and 490°C or 530°C, with steep downwards northeast directions. Two well-defined low-temperature decay to origin components were observed, although these directions were combined with the high temperature to origin components (HTO), from step 300°C to step 560°C. Two approximate clusters of downwards directions were produced: northwest and southeast. It is likely that these directions were due to a Pre-Cambrian overprint; due to the high error a VGP was not calculated from site R1. (Figure 34)

R2: Eight samples were drilled out of a dolerite dyke. The NRM magnetic moments were all ca. 10e-3 emu. 5 samples displayed prominent LN2 directions with a northwest direction. For samples G and H, over 60% of the magnetism was removed during the LN2 step. A well-defined low-temperature component was observed up until 150°C, 230°C, or 430°C, producing one cluster of downwards steep east directions, as well as another cluster of upwards north directions.

A second low thermal temperature component was measured across samples from 230°C or 300°C to 470°C or 480°C, with most samples producing steep downwards directions. A well-defined high-temperature component (HTO) was also demagnetized between 480°C or 510°C until 570°C or 580°C, roughly at the magnetite unblocking temperature. The HTO components produced a cluster of steep, downwards east directions, apart from clear outliers G and H. It is possible that samples G and H were struck by lightning, as they displayed strong magnetic moments and a large proportion of demagnetization at the LN2 step. As a result, a VGP was calculated from this site, although only incorporating samples A-F. (Figure 35)

C19R1:

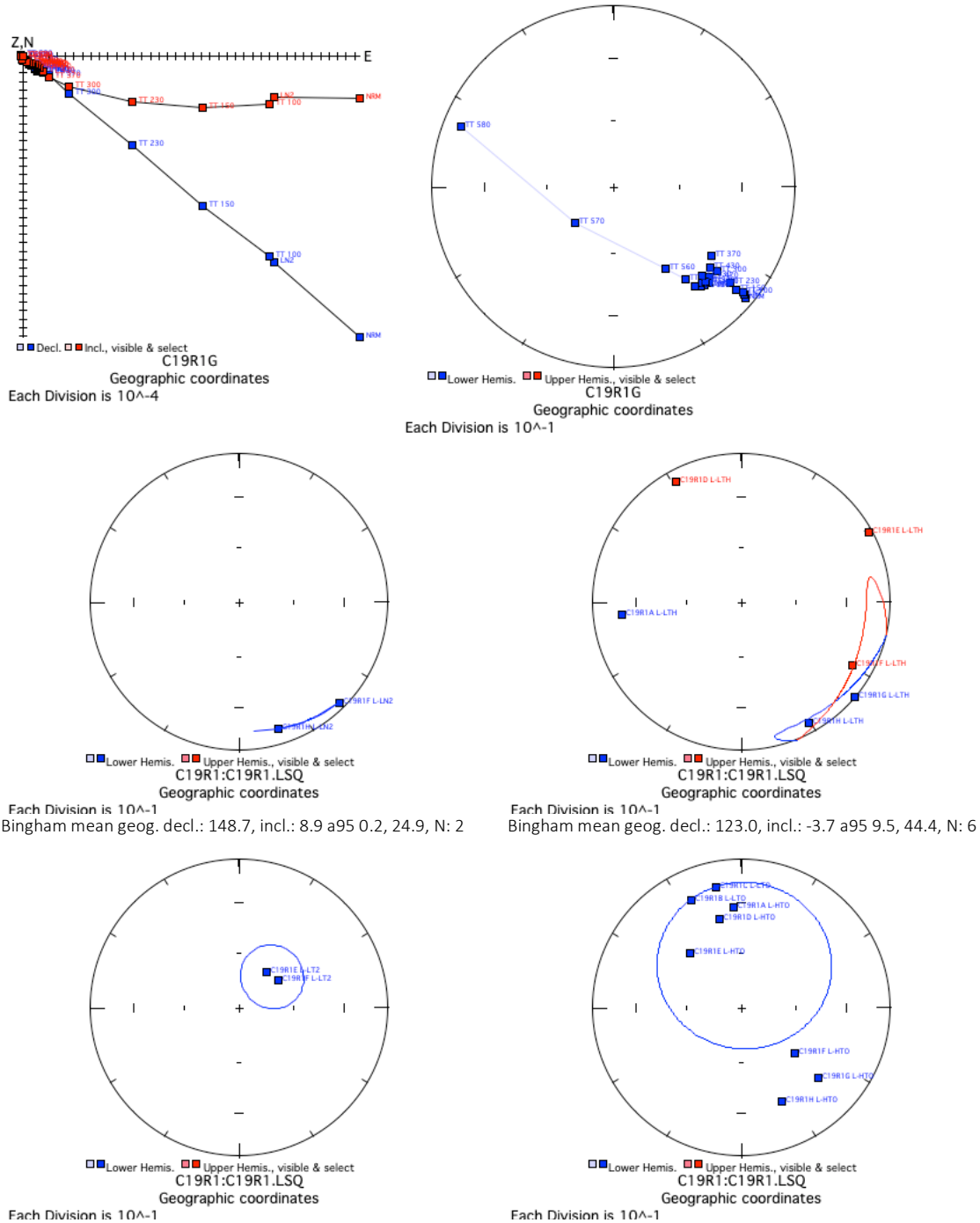

Bingham mean geog. decl.: 148.7, incl.: 8.9 a95 0.2, 24.9, N: 2

Bingham mean geog. decl.: 123.0, incl.: -3.7 a95 9.5, 44.4, N: 6

Fisher mean geog. decl.: 47.0, incl.: 64.8 a95 17.4, N: 2

Fisher mean geog. decl.: 4.2, incl.: 64.5 a95 47.8, , N: 8

Figure 34: Representative demagnetization behavior from site C19R1. Starting from top row left to right: (a) Zijderveld diagram of sample C19R1G, showing two components of the NRM. (b) Equal-area stereonet diagram of sample C19R1G. (c) Equal-area plot of the LN2 component with Bingham statistics 95% confidence ellipse. (d) Equal-area plot of the LTH component with Bingham statistics 95% confidence ellipse. (e) Equal-area plot of the LT2 component with Fisher statistics 95% confidence ellipse. (f) Equal-area plot of the HTO and MTO components with Fisher statistics 95% confidence ellipse.

C19R2:

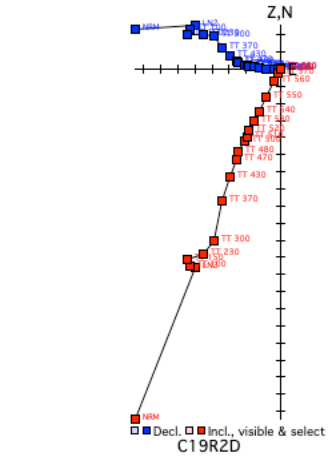

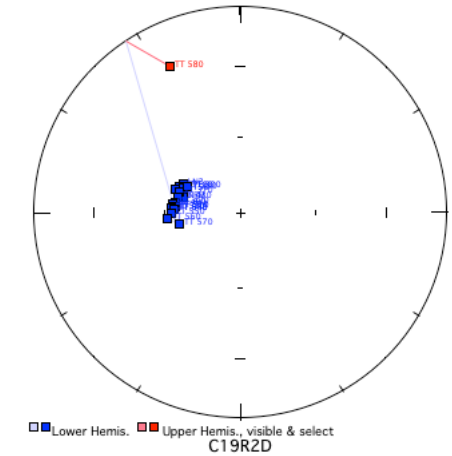

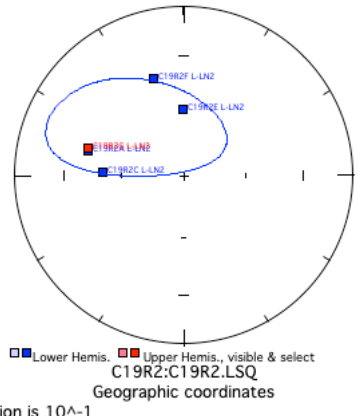

Bingham mean geog. decl.: 314.3, incl.: 55.8 a95 23.3, 45.1, N: 5

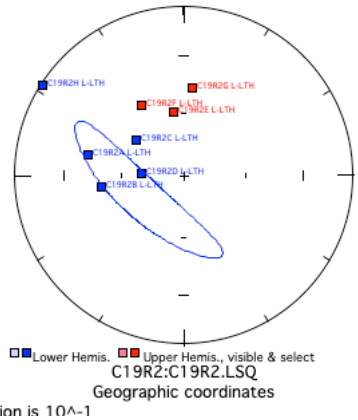

Bingham mean geog. decl.: 243.5, incl.: 66.7 a95 9.9, 48.1, N: 8

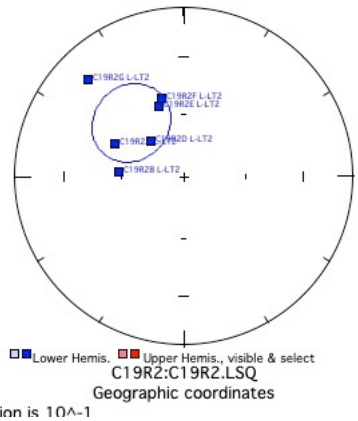

Fisher mean geog. decl.: 315.7, incl.: 53.0 a95 18.9 N: 6

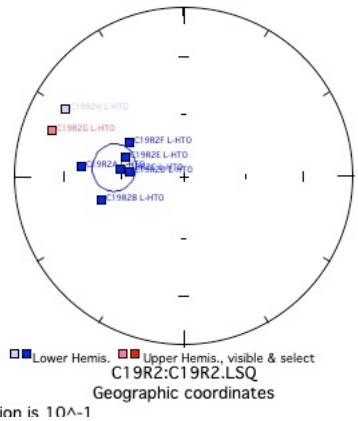

Fisher mean geog. decl.: 277.3, incl.: 55.8 a95 10.9 N: 6

Figure 35: Representative demagnetization behavior from site C19R2. Starting from top row left to right: (a) Zijderveld diagram of sample C19R2D, showing three components of the NRM. (b) Equal-area stereonet diagram of sample C19R2D. (c) Equal-area plot of the LN2 component with Bingham statistics 95% confidence ellipse. (d) Equal-area plot of the LTH component with Bingham statistics 95% confidence ellipse. (e) Equal-area plot of the LT2 component with Fisher statistics 95% confidence ellipse. (f) Equal-area plot of the HTO component with Fisher statistics 95% confidence ellipse.

DISCUSSION:

Bitterwater Fold Test:

All Bitterwater sites were able to produce precise primary remanent directions with the exception of V19D07. Therefore all sites apart from V19D07 were used in a fold test in order to better determine the amount of site mean clustering. A fold test will enable us to determine whether the remanent magnetic direction for the Bitterwater sites was obtained either during or before a potential folding event. The locality mean produced maximum k-values (precision) at 60% partial unfolding. (Figure 35d). The 95% confidence was tested using a 2.5% F-ratio test (Fisher et al. 1987). The population size was set to n=9 (16 x 16 degrees of freedom). For 0-100% unfolding, the k-value ratio (1.5480915) was significantly smaller than the critical F-value (2.76135911). This means that the variation in k-values from 0% to 100% unfolding was statistically insignificant. When setting the k value-ratio at 0-60% unfolding, the k-value (1.940751) was still smaller than the critical F-value, resulting in 0% to 60% unfolding to still be statistically insignificant. However, when calculating a mean VGP for the site, we used the mean remanent direction at 60% unfolding as this level of folding still showed the tightest cluster of the site means with the least amount of noise.

Overall it is clear that a syn-folding event should have occurred around the time of magnetization. The only major folding event known to have affected the Rehoboth Basement Inlier in the last 1100 Ma was the formation of the Damara Orogen at around 550 Ma. (Goscombe et al. 2020) However, it is likely that the Bitterwater anticline sampled in our fold test occurred at an earlier point in time than the Damara Orogenesis due to the shallow inclinations observed in the remanent directions. Therefore the magnetism must have originated from an older, unknown folding event. Kasbohm et. al. 2015 proposed a 1100 Ma late-Namaqua

folding event occurring in the Sinclair region (adjacent to the RBI) during their paleomagnetic study of the Auberes Formation. From our results, it is possible that the same folding event also influenced the Rehoboth Basement Inlier, and the remanent magnetism seen in our results exists as an overprint of such an event.

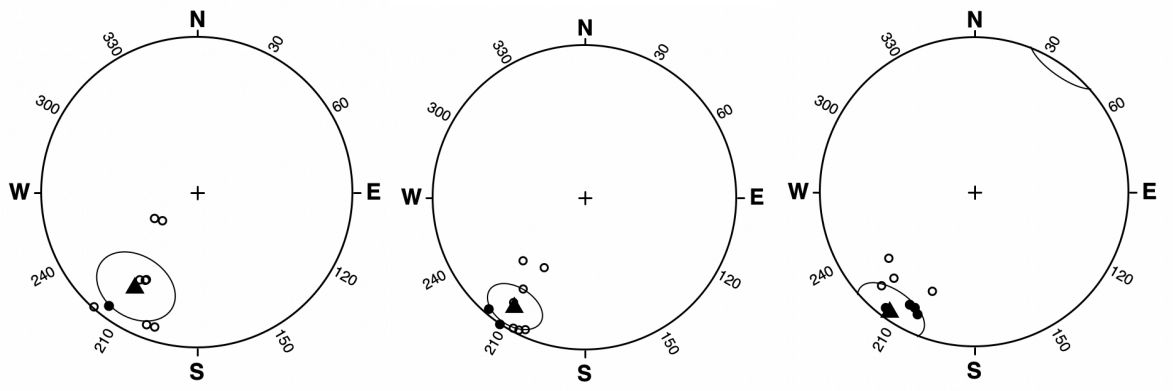

0% Unfolding 60% Unfolding 100% Unfolding

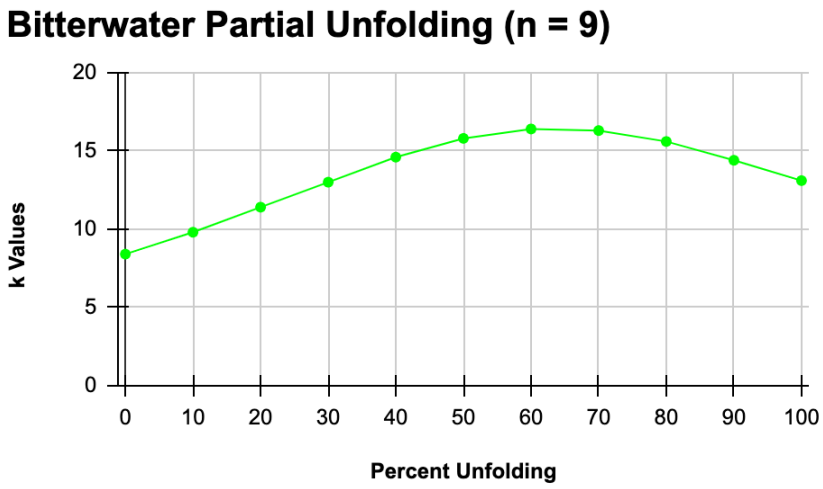

Figure 36: A diagram portraying the Bitterwater Fold Test. From top left to right: (a) Equal area plot of the mean direction at 0% unfolding (b) Equal area plot of the mean direction at 60% unfolding (c) Equal area plot of the mean direction at 100% unfolding. (d) A graph showing the variation of k values with percent unfolding.

Calculations of VGPs:

From our data, seven virtual geomagnetic poles (VGPs) were able to be calculated, with a minimum of one pole for every area sampled. We were able to calculate a pole representing the mean remanent direction from the Bitterwater fold test at 60% unfolding, four poles from the Swartkoppies region (S12, S13, S14, and S16), one pole from the Rehoboth region (R2), and one pole from the Uisib River Valley (U1). The calculated VGPs and their corresponding paleogeographic locations are shown in Table 5.

Table 5: A table of virtual geomagnetic poles calculated in this study.

Name/(VGP name)	Site Latitude (°N)	Site Longitude (°E)	Geographic Declination	Geographic Inclination	k	a95	Pole Latitude (°N)	Pole Longitude (°E)	A95
V19D (D)	-22.9	17.8	212.5	-15.8	17.1	12.8	44.9	66.7	8.1
S12	-23.1	17.5	343.6	29.9	N/A	13.8	47.7	-6.3	11.23
S13	-23.1	17.5	338.5	37.0	N/A	15.2	41.5	-9.8	13.6
S14	-23.1	17.5	206.9	1.2	N/A	5.5	55.5	70.6	3.9
S16	-23.1	17.5	333.3	28.0	N/A	14.8	43.9	-19.6	11.23
U1	-23.1	17.2	222.3	0.7	N/A	24.0	43.1	84.3	24.0
R2	-23.2	26.0	277.3	55.8	N/A	10.9	-8.0	-27.8	10.9

These new poles were then compared with previously discovered poles on the Kalahari craton's apparent polar wander path (APW), as shown in Figure 37.

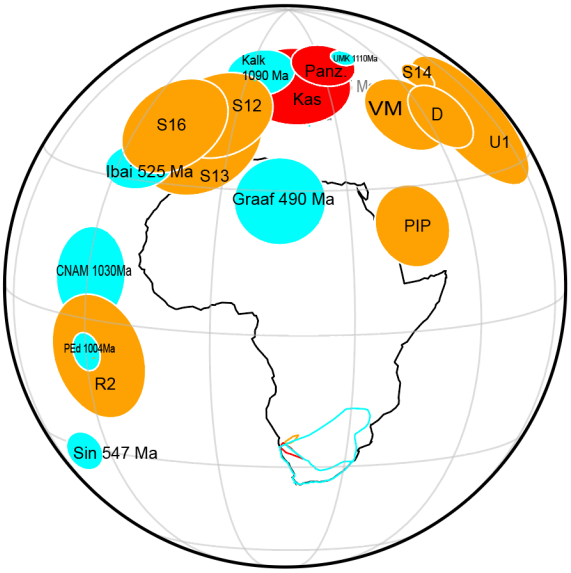

Figure 37: A map comparing the newly discovered VGPs with previously discovered poles on the Kalahari craton's Apparent Polar Wander Path. The red poles are part of the Konkiep, the orange poles were derived from the Rehoboth Basement Inlier, and the cyan poles are associated with the wander path of the Kalahari craton. Poles not discovered in this study are shown in Table 6. *It should be noted that Itabaiana and Sinyai poles are not directly Kalahari poles; Itabaiana is from South America and Sinyai is from Tanzania. However, at the time of their remanent magnetization they had rotated into Southern Africa (Gondwanaland formation), thus can be used for comparison to the poles of the RBI.

From Figure 37, three clusters of the new poles emerged. The Bitterwater mean pole (D) clustered with S14 and U1, whilst S12, S13 and S16 clustered together, and R2 existed on its own. The S12, S13 and S16 cluster and R2 both clearly followed the Cambrian Polar Wander Path (APW) marked by single representative poles, such as Sinyai, Itabaiana and Graafwater. S14 was not part of the Swartkoppies cluster, which was to be expected as it crosscut S15 and S16, thus we expected it to be of a different dyke generation. S14 formed a cluster with U1, D, and a new VGP calculated by Mai et al. 2021. What was surprising about this cluster was that although their maximum age constraint was 1100 Ma, they were all located much more easterly than one would expect for Kalahari poles of that age; the new poles were skewed at an angle from the Kalahari craton's strongly supported 1100 Ma paleopole location.

Table 6: List of poles used for comparison.

Name	Code	Age (Ma)	Latitude (°N)	Longitude (°E)	A95	Reference
Doornport Post-Fold	PIP	ca. 500	21.8	44.9	8.65	Piper et al. 1975
Umkondo LIP	UMK	ca. 1110	64.0	42.1	2.6	Swanson-Hysell et al. 2015
Aubures Formation	Kas	ca. 1100	56.7	18.3	11.5	Kasbohm et al. 2015
Guperas Dykes	Panz	ca. 1105	62.3	31.9	6.9	Panzik et al. 2016
Kalkpunt Formation	Kalk	ca. 1090	57.0	3.0	7	Briden et al. 1979
Itabaiana Mafic Dykes	Ibai	ca. 525	34.7	334.8	7.3	Trindade et al., 2006
Sinyai Metadolerite	Sin	ca. 547	-29.0	319.0	3.9	Meert and Van der Voo 1996
Central Namaqua	CNAM	ca.1030	9.0	-30.0	10	Onstott et al.,1986
Port Edward Charnockite	PEd	ca. 1004	-7.0	-30.0	4	Gose et al. 2004
Graafwater	Graaf	ca. 490	28.0	14.0	9.4	Bachtadse et al. 1987
Doornport Syn-Fold	VM	N/A	46.9	54.2	9.4	Mai, 2021

The skewed result was similar to that of a pole from Piper, 1975's paleomagnetic study on the sediments of the Doornpoort formation (PIP), also located in the RBI. The Doornpoort pole he obtained was thought to be anomalous at the time, and simply a metamorphic overprint caused by Damaran folding. (Piper, 1975) However, Piper's pole was skewed at the same angle as our data. Therefore, it was possible that the RBI had rotated as a singular micro-continental block relative to the rest of the Kalahari craton at an unspecified point in time.

We tested this hypothesis by rotating our poles 30 degrees counterclockwise around the southwestern edge of the RBI. (Figure 38) After this rotation, all our poles matched previously published reference poles from the ca. 1100 Ma Kalahari Craton, or Cambrian Gondwanaland

poles when shown in South African coordinates. The Mesoproterozoic poles (D, U1 and S14) were now situated in the same location as the other 1100 Ma poles including Kasbohm et al. 2015, as well as Panzik et al. 2016. The Cambrian Poles (S12,S13, S16 and R2) were now also rotated and had moved south, which also meant that their estimated age constraints had now changed. Pre-rotation, the location of R2 overlapped with the 1004 Ma Port Edward Charnockite Pole (Gose et al. 2004), a 1030 Ma pole calculated by Onstott et al. 1986, as well as unmarked 540 Ma and 530Ma poles from the APW of Torsvik et al., 2012. However, after rotation, the R2 pole now sat directly over the Sinyai 547 Ma pole (Meert and Van der Voo, 1996), which although is from Tanzania, is known to be a reliable pole for Gondwanaland thus can be a reference point for the Kalahari craton.

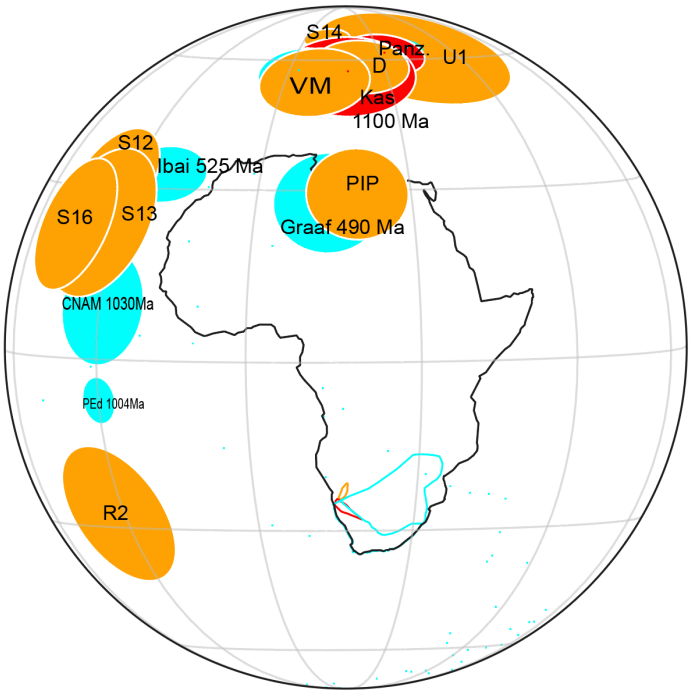

Figure 38: A map containing the newly discovered VGPs after a 30° rotation.

However, after rotation, the locations of the Swartkoppies poles overlap with Onstott et al. 1986's Central Namaqua pole at ca. 1030 Ma, as well as the Itabaiana 525 Ma Pole from Brazil, South America (Trinidade et al. 2006). As none of our VGPs have been directly dated, we are unable to make a definitive decision on the age of these dykes. If the magnetism of the Swartkoppies poles is a Cambrian overprint, the age of magnetism would be much more likely to be 525 Ma. However, it is important to note that the older ca. 1100 Ma S14 dyke crosscuts S16. Therefore if a Cambrian overprint was present in S16, it would be likely to be present in the data for S14. Comparing the data from the LT2 components of S14 and the MTO components of S16, in figures 18 (f) and figure 20 (h), this appears to be true. Both figures display the same moderately shallow north-northwest direction, which indicates that a Cambrian overprint most likely has occurred on the Swartkoppies dykes, although site S14 was affected to a lesser degree by the overprint than the other Swartkoppies dykes. This means that the age of the S12, S13 and S16 poles is much more likely to be ca. 525 Ma than 1030 Ma, although this argument can be strengthened further with additional geochronology and paleomagnetic field stability tests. Petrographic or more magnetic studies should be done on these sites in the future to evaluate each site's remagnetization susceptibility through magnetic mineralogy and grain size analysis.

Overall it is clear that at some point in the RBI's history, a 30-degree clockwise rotation took place. This rotation is limited to the RBI alone. Kasbohm et al. 2016's 1100 Ma pole was calculated from the Sinclair Region, located directly adjacent to the RBI. Since Kasbohm et al. 2016's pole did not show any signs of rotation, this indicates that the RBI rotated relative to the rest of the Kalahari craton.

This rotation most likely occurred sometime in the past 500 Ma. When Piper 1975's pole is restored by the same amount as bringing the Bitterwater pole to lie atop Umkondo and post-

Guperas poles at ca. 1100 Ma, it was directly overlain on top of the 490 Ma Graafwater Pole, indicating that Piper's pole most likely had an age of ca. 500 Ma. Since rotation needed to occur after both the poles calculated in this paper and Piper's pole were both fully magnetized, we can constrain the maximum age of rotation to be 500 Ma.

There is no clear reason for the rotation's origin. One potential cause for the rotation could be a folding event, such as the formation of the Damara Orogen, or due to the associated ocean closure. (Meert et al. 2008) It is possible that the rotation could have occurred with the breakup of Pangea, and the opening Southern Atlantic Ocean ca. 130 Ma. However, if this was the case, one would expect to see sedimentary basins with cretaceous clastic strata, which has not been observed around the RBI. However, Cambrian-Ordovician clastic strata of the Fish River Subgroup (Nama Group) has been observed. (Gerd 1995). The later stages of Damara Orogenesis therefore cannot be ruled out as a cause of rotation. However, more data is needed to investigate these hypotheses further and accurately determine the cause of rotation.

CONCLUSION:

Overall, our 2019 paleomagnetic reconnaissance study on the Northern Rehoboth Basement Inlier provides new information on the history of the entire Rehoboth Basement Inlier. The investigated volcanics were likely emplaced, deposited or erupted before 1100 Ma. During the Mesoproterozoic, at ca. 1100 Ma, a syn-folding event occurred, magnetizing the samples. Afterward, the RBI drifted with the Kalahari craton in and out of the Rodinia Supercontinent. At some point within the last 500 Ma, the Rehoboth Basement Inlier rotated as its own 'micro-plate, with a 30 degrees clockwise rotation relative to the rest of the Kalahari craton. Our studies also indicate that certain regions of the RBI, such as the Swartkoppies, were likely affected by a Cambrian overprint caused by the Damara Orogenesis. This study opens the door for new investigations. The Swartkoppies dykes need to undergo more extensive geochronological dating and petrographical analysis in order to better determine their ages and understand the factors causing differences of the region's Cambrian overprint. In addition, more knowledge is needed with regards to the 1100 Ma folding event and the cause of the RBI's rotation. Answering these questions is vital to having a more thorough understanding of the evolution of the Rehoboth Basement Inlier.

ACKNOWLEDGEMENTS:

I would like to thank Rene Krafft of Protea Farm, Erika and Harald Rotkegel of Bitterwater Farm, Given Bock of Swartkoppies Farm, Nico and Michael Van Wijk, and Aubry Bock at Uisib River for giving us permission to do fieldwork on their farms. I would also thank Anna Nguno at the Geological Survey of Namibia for official endorsement of our sampling, as well as Charlie Hoffman for perennial insights. Thank you to Ben Mapani, Martin Klausen, and most notably Johanna Salminen for accompanying us in the field. I would also like to thank my parents and my friends for always supporting me.

I would also like to thank the members of the Yale Paleomagnetic Laboratory. Thank you to Zheng Gong for helping me in the laboratory from day one. I would also like to give a huge thank you to Dr. Jikai Ding who helped me run my samples; due to the intense time constraints produced by COVID-19, it is unlikely that I would have finished my sample demagnetizations without Jikai. I would also like to thank Vuong Mai for supporting me both in and outside of fieldwork. I want to give the largest thank you my advisor Professor David Evans. Professor Evans has taught me so much about not only about paleomagnetism but also about general outdoor survival skills. Professor Evans' patience and enthusiasm has always inspired me to learn and grow more as a geologist. It is thanks to Professor David Evans' guidance that I was able to complete this thesis today.

REFERENCES

Bachtadse, V., Van der Voo, R., Hälbich I., (1987). Paleomagnetism of the western Cape Fold belt, South Africa, and its bearing on the Paleozoic apparent polar wander path for Gondwana. *Earth and Planetary Science Letters 84 (4):487-499.*

Becker, T., Wiegand, B., Hansen, B.T. and Weber, K. (2004). Sm-Nd, Rb-Sr and U-Pb data from the Rehoboth Basement Inlier, Namibia: Evidence of a Paleoproterozoic magmatic arc. *Communications of the Geological Survey of Namibia, 13*, 75-84.

Becker, T. (2005). The Mesoproterozoic event within the Rehoboth Basement Inlier of Namibia: review and new aspects of stratigraphy, geochemistry, structure and plate tectonic setting. *South African Journal of Geology*, *108*(4), 465–492.

Borg, G., & Maiden, K. (1989). The Middle Proterozoic Kalahari copperbelt of Namibia and Botswana. *Geological Association of Canada - Special Paper*, 525–539.

Briden, J.C., Duff, B.A., Kröner, A., 1979. Paleomagnetism of the Koras Group, Northern Cape Province. South Africa, *Precambrian Res.,* 10, 43-57.

Fisher, R. (1953). Dispersion on a Sphere. *Proceedings of the Royal Society A: Mathematical, Physical and Engineering Sciences*, *217*(1130), 295–305. https://doi.org/10.1098/rspa.1953.0064

Fisher, N., Lewis, T., & Embleton, B. (1987). *Statistical Analysis of Spherical Data*. Cambridge: Cambridge University Press.

Goscombe, B., Foster, D. A., Gray, D., & Wade, B. (2020). Assembly of central Gondwana along the Zambezi Belt: Metamorphic response and basement reactivation during the Kuunga Orogeny. *Gondwana Research*, *80*, 410–465.

Gose, W. A., Johnston, S. T., & Thomas, R. J. (2004). Age of magnetization of Mesoproterozoic rocks from the Natal sector of the Namaqua-Natal belt, South Africa. *Journal of African Earth Sciences*, *40*(3-4), 137–145.

Jones, C. H., User-driven Integrated Software Lives: “PaleoMag” Paleomagnetics Analysis on the Macintosh, Computers and Geosciences, 28 (10), 1145-1151, 2002.

Kasbohm, J., Evans, D.A., Panzik, J.E., Hofmann, M., & Linnemann, U. (2015). Palaeomagnetic and geochronological data from Late Mesoproterozoic redbed sedimentary rocks on the western margin of Kalahari craton. *Geological Society, London, Special Publications, 424,* SP424-4.

McElhinny, M. W., Powell, C. M. A., & Pisarevsky, S. A. (2003). Paleozoic terranes of eastern Australia and the drift history of Gondwana. *Tectonophysics*, *362*(1-4), 41–65.

Meert, J. G., & Van Der Voo, R. (1996). Paleomagnetic and40Ar/39Ar Study of the Sinyai Dolerite, Kenya: Implications for Gondwana Assembly. *The Journal of Geology*, *104*(2), 131–142.

Meert, J. G., & Lieberman, B. S. (2008). The Neoproterozoic assembly of Gondwana and its relationship to the Ediacaran–Cambrian radiation. *Gondwana Research*, *14*(1-2), 5–21.

Miller, R. M. G., Becker, T., & Shalk, K. (2008). The Geology of Namibia: Archaean to Mesoproterozoic. In *The geology of Namibia* (Vol. 1). essay, Ministry of Mines and Energy, Geological Survey.

Mitchell, R. N., Evans, D. A. D., & Kilian, T. M. (2010). Rapid Early Cambrian rotation of Gondwana. *Geology*, *38*(8), 755–758.

Müller, R. D., Cannon, J., Qin, X., Watson, R. J., Gurnis, M., Williams, S. (2018). GPlates: Building a virtual Earth through deep time. *Geochemistry, Geophysics, Geosystems, 19.*

Onstott, T. C., Hargraves, R. B., Joubert, P., Reid D. L.. (1986) Constraints on the tectonic evolution of the Namaqua Province; I, Palaeomagnetic and ^{40} Ar/ ^{39} Ar results from the Richtersveld Subprovince. *South African Journal of Geology, 89* (2), 117–142.

Panzik, Joseph & Evans, David & Kasbohm, J. & Hanson, Richard & Gose, W. & Desormeau, J. (2015). Using palaeomagnetism to determine late Mesoproterozoic palaeogeographic history and tectonic relations of the Sinclair terrane, Namaqua orogen, Namibia. *Geological Society, London, Special Publications.*

Piper, J. D. (1975). The Palaeomagnetism of Precambrian Igneous and Sedimentary Rocks of the Orange River Belt in South Africa and South West Africa. *Geophysical Journal International, 40(3), 313–344.*

Salminen, J., Hanson, R., Evans, D. A. D., Gong, Z., Larson, T., Walker, O., … Ernst, R. (2018). Direct Mesoproterozoic connection of the Congo and Kalahari cratons in proto-Africa: Strange attractors across supercontinental cycles. *Geology*, *46*(11), 1011–1014.

Schalk, K. (2006). *Sheet 2217D Dordabis (Provisional)*. Windhoek, Namibia; Geological Survey of Namibia .

Schwartz, M. O., Kwok, Y. Y., Davis, D. W., & Akanyang, P. (1996). Geology, geochronology and regional correlation of the Ghanzi Ridge, Botswana . *South African Journal of Geology*, *99*(3), 245–250.

Swanson-Hysell, N. L., Kilian, T. M., & Hanson, R. E. (2015). A new grand mean palaeomagnetic pole for the 1.11 Ga Umkondo large igneous province with implications for palaeogeography and the geomagnetic field. *Geophysical Journal International*, *203*(3), 2237–2247.

Trindade, R. I. F.; D'Agrella Filho, M.S.; Epof, I.; Neves, B.B.B. (2006). Paleomagnetism of Early Cambrian Itabaiana mafic dikes (NE Brazil) and the final assembly of Gondwana. *Earth and Planetary Science Letters, 244,* 361-377.

van Schijndel, V., Cornell, D. H., Frei, D., Simonsen, S. L., & Whitehouse, M. J. (2014). Crustal evolution of the Rehoboth Province from Archaean to Mesoproterozoic times: Insights from the Rehoboth Basement Inlier. *Precambrian Research*, *240*, 22–36.

Ziegler, U., & Stoessel, G. F. (1993). *Age determinations in the Rehoboth Basement Inlier, Namibia*. Geological Survey of Namibia, Ministry of Mines and Energy.

Ziegler, U., & Stoessel, G. (1990). Isotope Geology and Geochemistry of the Rehoboth Basement Inlier, Namibia/S.W. Africa; a Multimethod Case History. *Bulletin Swiss Association of Petroleum Geologists and Engineers*, *56*(130), 13–33.

APPENDIX:

Least Squares Analyses:

C19S01:

Sample	ID	NRM	LN2	100	150	230	300	350	375	400	425	450	475	500	515	530	540	550	555	560	565	575	580	Origin	Geographic Declination	Geographic Inclination	Stratigraphic Declination	Stratigraphic Inclination	MAD (6 degree cutoff)
A	LTH		X	X																					310.4	48.9	310.4	48.9	0
	LT2			X		X	X																		47.1	-63.9	47.1	-63.9	8.961973
	HTH						X	X	X	X							X								71.6	21.3	71.6	21.3	9.262975
	MTO																X						X	X	100.4	-32.1	100.4	-32.1	2.7
B	MTO	X	X	X	X	X	X	X	X	X	X	X	X	X	X	X	X	X	X	X	X	X	X	X	40.4	31.2	40.4	31.2	4.5
C	LTH		X	X																					271.1	43.1	271.1	43.1	0
	LT2			X	X	X	X																		351.3	-34.3	351.3	-34.4	4.5
	MTO						X	X	X	X	X	X	X	X	X	X	X	X	X	X	X	X	X	X	334.8	30	334.8	30	5.7
D	LTH		X	X																					205.2	54.4	205.2	54.4	0
	LT2			X	X	X	X																		347.4	-40.7	347.3	-40.7	2.4
	MTO						X	X	X	X	X	X	X	X	X	X	X	X	X	X	X	X	X	X	334.4	34.9	334.4	34.9	5.8
E	LTH		X	X																					259.7	45.3	259.7	45.3	0
	LT2			X	X	X	X																						
	HTH							X	x	x	x	x	x	x	x										4.2	17.5	4.2	17.5	7.3
	MTO														x	x								x	63.5	55.5	63.5	55.5	6.9
F	LTH	X	X	x																									
	LT2			x	x	x	x																						
	MTO						x	x	x	x	x	x	x	x		x	x							x	358.7	34.1	358.7	34.1	5.3
G	LTH	x	x																						100.7	45.5	100.7	45.5	0
	LT2			x	x	x	x																						
	HTH						x	x	x	x	x	x	x	x											3.9	26.1	3.9	26.1	7.4
	MTO													x	x	x								x	46.4	-35.9	46.4	-35.9	6.8
H	LTH	X	X	x																					186.4	74	186.4	74	7.6
	LT2			x	x	x	x																		6.7	-46.3	6.7	-46.3	2.1
	MTO						x	x	x	x	x	x	x	x	x	x								x	353.5	30.3	353.5	30.3	6

C19S02:

Sample	ID	NRM	LN2	100	150	230	300	330	375	400	425	450	475	500	515	530	540	550	565	560	565	575	580	Origin	Geographic Declination	Geographic Inclination	Stratigraphic Declination	Stratigraphic Inclination	MAD (6 degree cutoff)
A	LTH	x	x	x	x																				326.1	65.4	326.1	65.4	6.9
	MTO				X	X	X	X	X	X	X	X	X	X	X	X	X	X	X	X	X	X	X	X	289.6	62.4	289.6	62.4	1.2
B	LTH	X	X	X	X	X																			347.7	82.4	347.7	82.4	3.6
	MTO					X	X	X	X	X	X	X	X	X	X	X	X	X	X	X	X	X	X	X	1.6	88.4	1.6	88.4	1.3
C	LTH	X	X	X	X																				84.9	28.1	84.9	28.1	17.6
	MTO				X	X	X	X	X	X	X	X	X	X	X	X	X	X	X	X	X	X	X	X	101.3	32.5	101.3	32.5	3.6
D	LTH	X	X																						81.4	35	81.4	35	0
	MTO				X	X	X	X	X	X	X	X	X	X	X	X	X	X	X	X	X	X	X	X	99.3	35.1	99.3	35.1	2.1
E	LTH		X	X																					57.4	-8.7	57.4	-8.7	0
	MTO			X	X	X		X	X	X	X	X	X	X						X	X	X	X	X	315.9	-47.4	315.9	-47.4	5.1
F	LTH	X		X	X																				342.8	-35.1	342.8	-35.1	7.8
	MTO				X	X	X	X	X	X	X	X	X	X	X	X	X	X	X	X	X	X	X	X	284.5	-58.6	284.5	-58.6	5.2
G	LTH	X	X	X	X																				313.9	-40.5	313.9	-40.5	3.1
	MTO				X	X	X	X	X	X	X	X	X	X	X	X	X	X	X	X	X	X	X	X	312.5	-50.5	312.5	-50.5	3.4
H	LTH		X	X																					35.1	-55.4	35.1	-55.4	0
	MTO			X	X	X	X	X	X	X	X	X	X	X	X	X	X	X	X	X	X	X	X	X	325.4	-4.5	325.4	-4.5	5.2

C19S03:

Sample	ID	NRM	LN2	100	150	230	300	350	375	400	425	450	475	500	515	530	54	550	555	560	565	570	575	580	Origin	Geographic Declination	Geographic Inclination	Stratigraphic Declination	Stratigraphic Inclination	MAD (6 degree cutoff)
A	MTO	X	X	X	X	X	X	X	X	X	X	X	X	X	X	X	X	X	x	X	X	X	X	X	X	358.5	33.4	358.5	33.4	1.3
B	MTO	X	X	X	X	X	X	X	X	X	X	X	X	X	X	X	X	X	x	X	X	X	X	X	X	355.3	61.6	355.3	61.6	0.9
C	LTH		X	X	X	X	X																			37.5	29.9	37.5	29.9	5.9
	MTO								x				x		x										x	62	37	62	37	1.9
D	LTH	x	x	x																						41.9	-33.7	41.9	-33.7	3.8
	MTO					x	x	x																	x	54.8	-38.6	54.8	-38.6	6
E	LN2	x	x																							171.4	-30.6	171.4	-30.6	0
	LTH			x	x	x																				125.3	-58.1	125.3	-58.1	2.1
	MTO						x			x															x	194.1	-59.4	194.1	-59.4	4.8
F	LTH		X	X	X	X																				105.4	-68.8	105.4	-68.8	8.9
	MTO					X	X	X			X		X												X	159.9	-54.6	159.9	-54.6	3.5
G	LTH			x	x	x																				146.7	-53.7	146.7	-53.2	4.7
	MTO						x	x		x	x		x	x				x	x						x	174.8	-46.7	174.8	-46.7	7.2
H	LTH		X	X	X	X																				105.4	-68.8	105.4	-68.8	8.9
	MTO					X	X	X			X		X												X	159.9	-54.6	159.9	-54.6	3.5

C19S04:

Sample	ID	NRM	LN2	100	150	230	300	350	375	400	425	450	475	500	515	530	540	550	555	560	565	570	575	580	Origin	Geographic Declination	Geographic Inclination	Stratigraphic Declination	Stratigraphic Inclination	MAD (6 degree cutoff)
A	LTH	X	X	X	X																					216.3	54.1	216.3	54.1	8.9
	MTO					X	X	X	X	X	X	X	X	X	X	X	X	X	X	X	X	X	X	X	X	213.3	60.8	213.3	60.8	6.8
B	LTO		X	X	X	X	X	X	X	X	X	X	X	X	X	X	X	X	X	X	X	X	X	X	X	115.3	43	115.3	43	1.3
C	LTO	X	X	X	X	X	X	X	X	X	X	X	X	X	X	X	X	X	X	X	X	X	X	X	X	269.5	-25.7	269.5	-25.7	4.5
D	LTO	X	X	X	X	X	X	X	X	X	X	X	X	X	X	X	X	X	X	X	X	X	X	X	X	318.9	4	318.9	4	3.4
E	LTO	X	X	X	X	X	X	X	X	X	X	X	X	X	X	X	X	X	X	X	X	X	X	X	X	247.7	59.7	247.7	59.7	3.8
F	LTO	X	X	X	X	X		X	X	X	X	X	X	X	X	X	X	X	X	X	X	X	X	X	X	165.8	-4.3	165.8	-4.3	1.7
G	LTO	X	X	X	X	X	X	X	X	X	X	X	X	X	X	X	X	X	X	X	X	X	X	X	X	137.6	40.6	137.6	40.6	2.7
H	LTO	X	X	X	X	X	X	X	X	X	X	X	X	X	X	X	X	X	X	X	X	X	X	X	X	237.3	-54.6	237.3	-54.6	1.2

C19S05:

Sample	ID	NRM	LN2	100	150	230	300	350	375	400	425	450	475	500	515	530	540	550	555	560	565	570	575	580	Origin	Geographic Declination	Geographic Inclination	Stratigraphic Declination	Stratigraphic Inclination	MAD (6 degree cutoff)
A	LTH		X	X	X	X																				3.6	-42.2	3.6	-42.2	1.2
	MTO									X	X	X	X	X	X	X		X	X	X	X	X	X	X	X	230.1	16.9	230.1	16.9	3.7
B	LTH		X	X	X	X																				18.4	-28.3	18.4	-28.3	8.5
	LT2					X	X	X	X	X	X															19.8	75.7	19.8	75.7	3.6
	MTO											X	X	X	X	X	X	X	X	X	X	X	X	X	X	96.5	80.2	96.5	80.2	0.7
C	LTH			X	X	X																				357	-46.6	357	-46.6	5.3
	LT2					X	X			X	X															347.3	18.8	347.3	18.8	2.4
	MTO											X	X	X	X	X	X	X	X	X	X	X	X	X	X	323.7	-21.6	323.7	-21.6	4.9
D	LTO	X	X	X	X	X	X	X	X	X	X	X	X	X	X	X	X	X	X	X	X	X	X	X	X	51.8	-42.5	51.8	-42.5	3.7
E	LTH		X	X				X	X	X	X															16.5	40.3	16.5	40.3	5.7
	MTO										X	X	X	X	X	X	X	X	X	X	X	X	X	X	X	108.4	72	108.4	72	1.2
F	LTO	X	X	X	X	X	X	X	X	X	X	X	X	X	X	X	X	X	X	X	X	X	X	X	X	352.6	-74	352.6	-74	3.2

C19S06:

Sample	ID	NRM	LN2	100	150	230	300	350	375	400	425	450	475	500	515	530	540	550	555	560	565	570	575	580	Origin	Geographic Declination	Geographic Inclination	Stratigraphic Declination	Stratigraphic Inclination	MAD (6 degree cutoff)
A	LTO		X	X	X	X	X	X	X	X	X	X	X	X	X	X	X	X	X	X	X	X	X	X	X	36.4	-19	36.4	-19	2.2
B	LTO		X	X	X	X	X	X	X	X	X	X	X	X	X	X	X	X	X	X	X	X	X	X	X	71	55.3	71	55.3	2.6
C	LTH		X	X	X	X																				46.9	-29.6	46.9	-29.6	7.2
	LT2						X	X	X	X	X															223	-33.1	223	-33.1	3.9
	HTO											X	X	X	X	X	X	X	X	X	X	X	X	X	X	75.9	26.9	75.9	26.9	2.6
D	LTO	X	X				X	X	X	X	X	X	X	X	X	X	X	X	X	X	X	X	X	X	X	279.4	36.7	279.4	36.7	5.3
E	LTH		X	X	X	X		X	X	X	X															185.2	-30.8	185.2	-30.8	4.8
	HTO											X	X	X	X	X	X	X	X	X	X	X	X	X	X	146.2	-25.4	146.2	-25.4	5.7
F	LTO		X	X	X	X	X	X	X	X	X	X	X	X	X	X	X	X	X	X	X	X	X	X	X	188.8	-3.8	188.8	-3.8	2
G	LTO		X	X	X	X	X	X	X	X	X	X	X	X	X	X	X	X	X	X	X	X	X	X	X	293.9	20.3	293.9	20.3	2.2
H	LTO		X	X	X	X	X	X	X	X	X	X	X	X	X	X	X	X	X	X	X	X	X	X	X	265.1	36.2	265.1	36.2	3

C19S07:

Sample	ID	NRM	LN2	100	150	230	300	350	375	400	425	450	475	500	515	530	540	550	555	560	x	565	575	580	Origin	Geographic Declination	Geographic Inclination	Stratigraphic Declination	Stratigraphic Inclination	MAD (6 degree cutoff)
A	LTO		X	X	X	X	X	X	X	X	X	X	X	X	X	X	X	X	X	X	x	X	X	X	X	298.9	16.3	298.9	16.3	2.1
B	LTC		X		X		X	X																		316.6	-1.9	316.6	-1.9	7.5
	MTO								X	X	X	X	X	X	X	X	X	X	X	X	x	X	X	X	X	290.9	18.6	290.9	18.6	2.1
C	LTC		X		X	X																				346.2	-33.1	346.2	-33.1	6.5
	MTO					X	X	X	X		X	X					X	X	X								328.4	44.8	328.4	44.8	6.1
D	LN2	x	x																							35.2	51.8	355.2	51.8	0
	LTH			x	x	x																				345.5	-43.6	345.5	-43.6	0.4
	HTO								x	x	x														x	289	61.1	289	61.1	9.5
E	LTC	X	X	X	X	X																				205.4	73.6	205.4	73.6	5.4
	LT2					x	x	x	x																	179.1	59.4	179.1	59.4	3.1
	MTO	x	x		x	x	x	x	x																x	189.3	65.2	189.3	65.2	2
F	LTO				x	x	x	x	x	x	x	x	x	x	x	x	x	x	x	x	x	x	x	x	x	130.4	41.8	130/4	41.8	2.4
G	LTO	x	x	x	x	x	x	x	x	x																209.7	36	29.7	36	2.2
H	LTC			x	x	x																				13.3	-45.9	13.3	-45.9	4.9
	MTO					x	x	x	x	x																346.8	44.5	346.8	44.5	8.5
I	LTC	x	x	x																						348.8	7.5	348.8	7.5	5.9
	MTO						x	x	x																	330	27.8	330	27.8	6.2

C19S08:

Sample	ID	NRM	LN2	100	150	230	300	350	375	400	425	450	475	500	515	530	540	550	555	560	565	570	575	580	Origin	Geographic Declination	Geographic Inclination	Stratigraphic Declination	Stratigraphic Inclination	MAD (6 degree cutoff)
A	LTO	x	x	x	x	x	x	x	x	x	x	x	x	x	x	x	x	x	x	x	x	x	x	x	x	287.9	10.3	287.9	10.3	3.5
B	LTH		x	x	x	x																				333.3	-20.8	333.3	-20.8	6.8
	HTO					x	x	x	x	x	x	x	x	x	x	x	x	x	x	x	x					326.4	34	326.4	34	3.7
C	LTO				X	X	X	X	X	X	X	X	X	X	X	X	X	X	X	X	X	X	X	X	X	165.6	34.2	165.5	34.2	6.1
D	LTH		X	X		X																				35	51.2	35	51.2	5.5
	HTO					X	X	X	X	X	X	X	X	X	X	X	X	X	X	X	X	X	X	X	X	154.1	16.9	154.1	16.9	1.8
E	LTO		X	X	X	X	X	X	X	X	X	X	X	X	X	X	X	X	X	X	X	X	X	X	X	337.7	56.1	337.7	56.1	1.7
F	LTH	X	X	X		X																				7.6	-70.1	7.6	-70.1	6.2
	LT2					X	X	X																		8.9	-52.2	8.9	-52.2	2.1
	HTO								X	X	X	X	X	X	X	X	X	X	X	X	X	X	X	X	X	7.8	-19.8	7.8	-19.8	2.5
G	LTO		X		X	X	X	X	X	X	X	X	X	X	X	X	X	X	X	X	X	X	X	X	X	139	40.4	139	40.4	2.2
H	LTO		X			X	X	X		X	X	X		X	X	X	X	X	X	X	X	X	X	X	X	158.7	58.9	158.7	58.9	1.9

C19S09:

Sample	ID	NRM	LN2	100	150	230	300	350	375	400	425	450	475	500	515	530	540	550	555	560	565	570	575	580	Origin	Geographic Declination	Geographic Inclination	Stratigraphic Declination	Stratigraphic Inclination	MAD (8 degree cutoff)
A	LTO	X	X	X	X	X	X	X	X	X	X	X	X	X	X	X	X	X	X	X	X	X	X	X	X	84.3	53.1	84.3	53.1	2.7
B	LTO	X	X	X	X	X	X	X	X	X	X	X	X	X	X	X	X	X	X	X	X	X	X	X	X	2.1	57.2	2.1	57.2	1.4
C	LTH		X	X	X	X	X	X	X	X	X	X	X	X	X	X	X									42.8	60	42.8	60	6.4
	HTO																X	X	X	X	X	X	X	X	X	74.8	68.8	74.8	68.8	2
D	LTO	X	X	X	X	X	X	X	X	X	X	X	X	X	X	X	X	X	X	X	X	X	X	X	X	130.9	54.5	130.9	54.5	1.1
E	LTH		X		X	X																				32.3	-42.7	32.3	-42.7	2.2
	HTO						X	X		X	X	X	X	X	X	X	X	X	X	X	X	X	X	X	X	53	27.6	53	27.6	2.5
F	LTH		X	X	X	X	X																			2.5	-33	2.5	-33	7.3
	LT2						X	X		X			X	X	X											8	-7.7	8	-7.7	5.2
	HTO														X	X	X	X	X	X	X	X	X	X	X	1.1	-7.3	1.1	-7.3	3.4
G	LTH	X	X	X	X	X																				45.9	-8.5	45.9	-8.5	3.7
	HTO						X	X	X	X	X	X	X	X	X	X	X	X	X	X	X	X	X	X	X	51.1	4.2	51.1	4.2	1.5
H	LTH		X	X		X	X	X	X	X	X															286.8	52.5	286.8	52.5	5.5
	HTO											X	X	X	X	X	X	X	X	X	X	X	X	X	X	286	61.3	286	61.3	1.4

C19S10:

Sample	ID	NRM	LN2	100	150	230	300	350	375	400	425	450	475	500	515	530	540	550	555	560	565	570	575	580	Origin	Geographic Declination	Geographic Inclination	Stratigraphic Declination	Stratigraphic Inclination	MAD (8 degree cutoff)
A	LTO	X	X	X	X	X	X	X	X	X	X	X	X	X	X	X	X	X	X	X	X	X	X	X	X	306.9	-47.2	306.9	-47.2	1.2
B	LTH		X	X	X		X																			21.6	-32.7	21.6	-32.7	7.3
	LT2						X	X	X	X	X															13.2	30.3	13.2	30.3	4.1
	MTO										X	X	X	X	X	X	X	X	X	X	X			X	X	14.9	10.2	14.9	10.2	6.9
C	LTH	X	X	X																						48.3	12.9	48.3	12.9	7.6
	MTO						X	X	X	X	X	X	X	X	X	X	X	X	X	X	X	X	X	X	X	21.3	31.5	21.3	31.5	4
D	LTH	X	X	X																						48.7	-8.3	48.7	-8.3	5.9
	LT2					X	X	X	X	X	X															0.4	11.1	0.4	11.1	9.1
	MTO												X	X	X		X	X				X			X	337.4	-44.5	337	-44.5	5.2
E	LTH	X		X	X	X																				351.7	-45.2	351.7	-45.2	1.3
	LT2						X	X	X	X	X	X														356	17.5	356	17.5	3.8
	MTO											X	X	X	X						X				X	347.7	-34.9	347.7	-34.9	4.9
F	LTO	X		X	X	X	X	X	X	X	X	X	X	X	X	X	X	X	X	X	X	X	X	X	X	27	21.9	27	21.9	0.4
G	LTH		X	X																						59.7	1	59.7	1	0
	LT2			X	X	X																				359	-41	359	-41	3.6
	MTO					X	X	X	X	X	X	X	X	X	X										X	12.8	43.3	12.8	43.3	2.9
H	LTH			X	X	X																				359.9	-49	359.9	-49	1.6
	MTO					X	X	X	X	X	X	X	X					X							X	359.5	33.5	359.5	33.5	4.1

C19S11:

Sample	ID	NRM	LN2	100	150	230	300	370	420	470	480	490	500	510	520	530	540	550	560	570	580	Origin	Geographic Declination	Geographic Inclination	Stratigraphic Declination	Stratigraphic Inclination	MAD (8 degree cutoff)
A	LTH			x	x	x																	326	-37.7	326	-37.7	8.2
	LT2					x	x	x															306.8	-4.8	306.7	4.8	7.2
	HTO												X	X								X	5.2	73.3	5.2	73.3	1
B	LTO	X	X	X	X	X	X	X		X	X	X	X	X	X	X	X	X	X	X	X	X	38.9	37.1	38.9	37.1	2.6
C	LN2	x	x																				101.4	15.8	101.4	15.8	0
	LTH			x	x	x																	11.6	-55.8	11.6	-55.8	5.1
	HTO										x		x	x	x	x						x	105.6	1.9	105.6	1.9	3.2
D	LTH	x	x	x																			70.4	73	70.4	73	5.3
	LTO				x	x	x															x	29.6	-69.1	29.6	-69.1	5.5
E	LTH	x	x	x																			156.9	-63.6	156.9	-63.6	5.8
	LT2				x	x	x																46.8	-39.5	46.8	-39.5	2.7
	HTO						x	x	x													x	342.6	25	342.6	25	13
F	LN2	x	x																				166	-23.2	166	-23.2	0
	LTH			x	x	x																	349.2	-57.3	349.2	-57.3	4.5
	HTO						x	x	x													x	332.8	32.6	332.8	32.6	7.2
G	LTH	x	x	x																			134.6	-73.4	134.6	-73.4	6.7
	LT2			x	x	x																	343.8	-2.2	343.8	-52.2	6.4
							x	x	x													x	331.7	32.1	331.7	32.1	5.7
H	LN2	x	x																				195.6	-42.5	195.6	-42.5	0
	LTH			x	x	x																	310.2	-51.4	310.2	-51.4	6.4
	HTO						x	x	x													x	344.8	37.9	344.8	379	7.6

C19S12:

Sample	ID	NRM	LN2	100	150	230	300	370	430	470	480	490	500	510	520	Origin	Geographic Declination	Geographic Inclination	Stratigraphic Declination	Stratigraphic Inclination	MAD (6 degree cutoff)
A	LTH	x	x	x													314.3	-45	314.3	-45	2
	LT2				x	x	x										352.9	-54	352.9	-54	3.8
	HTO						x	x	x								341.3	9.5	341.3	9.5	6.5
B	LTH	x	x	x	x	x											343.4	-51.8	343.4	-51.8	2.8
	HTO						x	x	x								349.7	-9.2	349.7	-9.2	5.9
C	LTH	x	x	x	x	x											354.6	-41.8	354.6	-41.8	5
	HTO						x	x	x							x	333.3	39.3	333.3	39.3	8.5
								0													
D	LTH	x	x	x	x												342.6	-41.9	342.6	-41.9	3.7
	HTO					x	x	x								x	341.9	21.8	341.9	21.8	5.6
E	LTH	X	X	X	X												345.4	-47	345.4	-47	4.9
	HTO					X	X	X								X	349.1	21.1	349.1	21.1	5.2
F	LTH	X	X	X													356.2	-31.2	356.2	-31.2	4.5
	HTO						X	X				x				X	342.6	34.5	342.6	34.5	13.3
G	LTH	x	x	x	x												342.1	-62.9	342.1	-62.9	7.2
	HTO						x	x								x	355.8	52.2	355.8	52.2	9
H	LTO	x	x	x		x	x	x								x	3	-31.3	3	-31.3	13.3

C19S13:

Sample	ID	NRM	LN2	100	150	230	300	370	420	470	480	490	500	510	520	530	540	550	560	570	580	Origin	Geographic Declination	Geographic Inclination	Stratigraphic Declination	Stratigraphic Inclination	MAD (6 degree cutoff)
A	LN2	x	x																				162.5	-36.9	162.5	-36.9	0
	LTO			x	x	x	x															x	6.4	29.1	6.4	29.1	26.4
B	LTH	x	x	x																			357.6	16.8	357.6	16.8	7.9
	LT2			x	x	x																	335.9	-58.2	335.9	-58.2	6.5
	HTO						x			x	x	x										x	335.6	12.3	335.6	12.3	7.1
C	LN2	x	x																				182.2	-64	182.2	-64	0
	LTH		x	x	x	x																	347.8	-60	347.9	-60	6.3
	HTO						x	x	x		x											x	339.1	40.9	339.1	40.9	4.8
D	LN2	x	x																				186.2	-22.9	186.2	-22.9	0
	LTH			x	x	x																	25.3	-70.2	25.3	-70.2	6.2
	HTO								x	x	x	x	x		x								187.7	-6.7	187.7	-6.7	3.8
E	LN2	x	x																				0.1	36	0.1	36	0
	LTO					x	x	x	x	x	x	x	x	x	x	x	x	x	x	x		x	346.5	43.8	346.5	43.8	1.4
F	LN2	x	x																				256.5	-55.8	256.5	-55.8	0
	LTH		x	x	x	x																	337.1	-54.7	337.1	-54.7	6.2
	HTO					x	x	x	x													x	342.2	38.8	342.2	38.8	5.4
G	LN2	x	x																				251.8	-39.8	251.8	-39.8	0
	LTH			x	x	x																	302.8	-53.8	302.8	-53.8	2
	MTO						x	x														x	323.8	47.9	323.8	47.9	4.9
H	LN2	x	x																				205.6	-44.5	205.6	-44.5	0
	LTH			x	x	x																	354.7	-60.2	354.7	-60.7	4.9
	MTO						x	x	x													x	351.4	43	351.4	43	4.3

C19S14:

Sample	ID	NRM	LN2	100	150	230	300	370	420	470	480	490	500	510	520	530	540	550	560	570	580	Origin	Geographic Declination	Geographic Inclination	Stratigraphic Declination	Stratigraphic Inclination	MAD (6 degree cutoff)
A	LN2	x	x																				138.6	17.6	138.6	17.6	0
	LTH			x	x	x																	346.7	-44.6	346.7	-44.6	2.9
	LT2					x	x	x	x	x													338.2	31.9	338.2	31.9	4.5
	MTO										x	x	x	x			x	x				x	204.8	4.2	204.8	4.2	6.9
B	LN2	x	x																				31.1	23.1	31.1	23.1	0
	LTH			x	x	x																	0.1	-31.1	0.1	-31.1	7.8
	LT2						x	x	x	x	x	x	x	x									349	36.7	349	36.7	3.3
	MTO														x	x	x	x	x	x		x	206.6	12.1	206.6	12.1	3.1
C	LN2	x	x																				63.6	-46.1	63.6	-46.1	0
	LTH				x	x	x	x		x	x	x	x	x									346	25.8	346	25.8	5.4
	MTO															x	x	x	x	x		x	208.7	0.1	208.7	0.1	0.7
D	LN2	x	x																				60.5	-47.5	60.5	-47.5	0
	LTH		x		x	x																	353.4	-41.8	353.4	-41.8	2.8
	LT2						x	x	x	x													349.3	16.5	349.3	16.5	6.3
	MTO														x	x	x	x	x	x		x	208.3	-3.2	208.3	-3.2	0.7
E	LN2	x	x																				171.9	-60.8	171.9	-60.8	0
	LTH			x	x	x																	342.7	-48	342.7	-48	3
	LT2					x	x	x	x	x													333.3	30.1	333.3	30.1	3.2
	MTO													x	x	x	x	x	x	x	x	x	209.4	-0.1	209.4	-0.1	2.9
F	LN2	x	x																				61.2	-51.8	61.2	-51.8	0
	LTH		x	x	x	x																	0.2	-54.5	0.2	-54.5	7.9
	LT2					x	x	x		x	x												346.4	28.9	346.4	28.9	3.9
	MTO													x	x	x	x		x			x	203.8	-5.7	203.8	-5.7	3.4
G	LN2	x	x																				219.3	52	219.3	52	0
	LTH				x	x	x	x	x	x	x												287.6	63	287.6	63	7.1
	MTO												x	x	x	x	x	x	x			x	214.6	31.2	214.6	31.2	1.4
H	LN2	x	x																				357.4	0.7	357.4	0.7	0
	LTH		x	x	x	x																	1.5	-44.9	1.5	-44.9	6.4
	MTO					x	x	x	x													x	327.9	39.5	327.9	39.5	6.6

C19S15:

Sample	ID	NRM	LN2	100	150	230	300	370	430	470	480	490	500	519	523	539	540	550	560	570	575	580	585	590	600	620	645	660	670	680	Origin	Geographic Declination	Geographic Inclination	Stratigraphic Declination	Stratigraphic Inclination	MAD (6 degree cutoff)
A	LTO			x	x	x	x	x		x	x	x	x	x	x	x	x	x	x	x	x	x	x	x	x	x	x	x	x	x	x	255	-14			2.2
B	LN2	x	x																													251.8	23.8			0
	LTO			x	x	x	x	x	x	x	x	x	x	x	x	x	x	x	x	x	x	x	x	x	x	x	x	x	x	x	x	247.8	-8.6			1.9
C	LTO			x	x	x			x	x	x	x	x	x	x	x	x	x	x	x	x	x	x		x						x	244.4	7.2			1.7
D	LTH	x	x	x	x																											262.6	12.8			4.7
	MTO					x	x	x		x	x	x	x	x	x	x	x	x	x	x	x	x	x	x	x	x	x	x	x	x	x	255.9	9.3			2.9
E	LN2	x	x																													293.1	9.3			0
	LTO			x	x	x		x	x	x	x	x	x	x	x	x	x	x	x	x	x	x	x	x	x	x	x	x	x	x	x	289.2	35.3			1.3
F	LN2	x	x																													290.7	-41.5			0
	LTO			x	x	x	x	x	x	x	x	x	x	x	x	x	x	x	x	x	x	x	x	x	x	x	x	x	x	x	x	283.5	19.5			2.7
G	LN2	x	x																													324.4	-71.9			0
	LTO			x	x	x	x	x	x	x	x	x	x	x	x	x	x	x	x	x	x	x	x	x	x						x	307.8	32.3			3.9
H	LN2	x	x																													80.7	-49.6			0
	LTH			x	x	x	x	x	x	x																						327.7	28.5			0.7
	MTO										x	x	x	x	x	x	x	x	x	x	x	x	x								x	333.8	10.4			6.9

C19S16:

Sample	ID	NRM	LN2	100	150	230	300	370	430	470	480	490	500	510	520	530	540	550	560	570	580	Origin	Geographic Declination	Geographic Inclination	Stratigraphic Declination	Stratigraphic Inclination	MAD (6 degree cutoff)
A	LN2	x	x																				124	71.2	124	71.2	0
	LTH			x	x	x	x	x	x														213.2	71.1	213.2	71.1	4.3
	MTO															x	x	x	x	x	x	x	220.5	4.5	220.5	49.5	6.8
B	LN2	x	x																				124.5	-25.2	124.5	-25.2	0
	LTH			x	x	x	x	x	x	x													132.2	-16.1	132.2	-16.1	3
	MTO										x	x	x	x	x	x	x	x	x			x	145.2	-13.2	145.2	-13.2	2.8
C	LN2	x	x																				70.3	22.6	70.3	22.6	0
	LTO			x	x	x	x	x	x	x	x	x	x	x	x	x	x	x	x			x	90	17.7	90	17.7	3.8
D	LTH	x	x	x																			1.2	-29.9	1.2	-29.9	1.4
	LT2			x	x	x																	20.6	-56.5	20.6	-56.5	2.4
	LTO					x	x	x														x	350.9	23.1	350.9	2.1	3.3
E	LN2	x	x																				142.1	18.8	142.1	18.8	0
	LTO			x	x	x	x	x	x	x	x	x	x	x	x	x	x	x	x	x		x	140.8	18.8	140.8	18.8	2.7
F	LN2	x	x																				49.1	-66.4	49.1	-66.4	0
	LTH		x	x	x	x																	347.6	-46.6	347.6	-46.6	3.1
	MTO						x	x	x	x													334	37	334	37	6.3
G	LN2	x	x																				61.4	-53	61.4	-53	0
	LTH		x	x	x	x																	357.6	-48	357.6	-48	3.1
	MTO						x	x	x	x	x											x	327	-43.3	327	43.3	3.5
H	LN2	x	x																				407	-44.5	40.7	-44.5	0
	LTH			x	x	x																	340.3	-44	340.3	-44	3.9
	MTO					x		x	x	x													328.7	21.7	328.7	21.7	5

C19S17:

Sample	ID	NRM	LN2	100	130	230	300	370	430	470	480	490	500	510	520	530	540	550	560	570	580	Origin	Geographic Declination	Geographic Inclination	Stratigraphic Declination	Stratigraphic Inclination	MAD (6 degree cutoff)
A	LTH	x	x	x																			204.7	-40.9	204.7	-40.9	6.1
	HTO					x	x	x	x									x				x	318.1	44.5	318.1	44.5	6.9
B	LTH	x	x	x	x																		20.9	-24.3	20.9	-24.3	4.8
	HTO					x	x	x		x		x										x	1.9	9.7	1.9	9.7	6.9
C	LN2	x	x																				205.1	-33.2	205.1	-33.2	0
	LTH			x	x	x																	3.2	-54.3	3.2	-54.3	3.8
	HTO						x	x														x	352.8	29	352.8	29.8	6.8
D	LN2	x	x																				241.1	-33.3	241.1	-33.3	0
	LTH		x	x	x	x	x																340	-49.6	340	-49.6	4.1
	HTO									x	x			x		x	x					x	302.5	-6.2	302.5	-6.2	7.6
E	LN2	x	x																				75.2	-46.7	75.2	-46.7	0
	LTH			x	x	x																	346.7	-47	346.7	-47	2.4
	HTO						x	x						x	x							x	353.4	39.6	353.4	39.6	6.6
F	LN2	x	x																				103.9	-23.2	103.9	-23.2	0
	LTH			x	x	x	x																356.2	-48.2	356.2	-48.2	4.5
	HTO							x	x	x	x	x	x	x	x	x	x	x	x			x	97.7	-0.1	97.7	-0.1	2.9
G	LN2	x	x																				110.7	-66.9	110.7	-66.9	0
	LTH			x	x	x																	359.6	-47.6	359.6	-47.6	3.8
	LT2						x	x	x	x													344.9	32.5	344.9	32.5	3.9
	HTO										x		x	x		x		x	x			x	326.9	-30.6	326.9	-30.6	4
H	LN2	x	x																				160.5	13.8	160.5	13.8	0
	LTH					x	x	x															210.1	46.6	210.1	46.6	4.6
	HTO								x	x		x			x		x	x	x	x		x	167.6	22.1	167.6	22.1	1.7

V19D01:

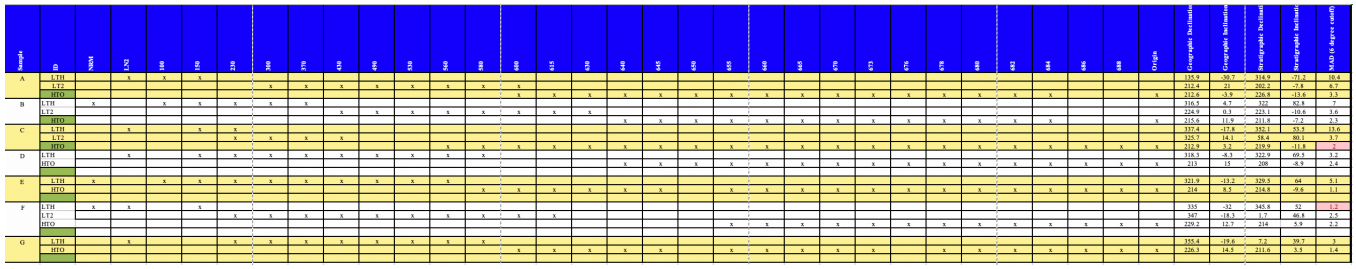

V19D02:

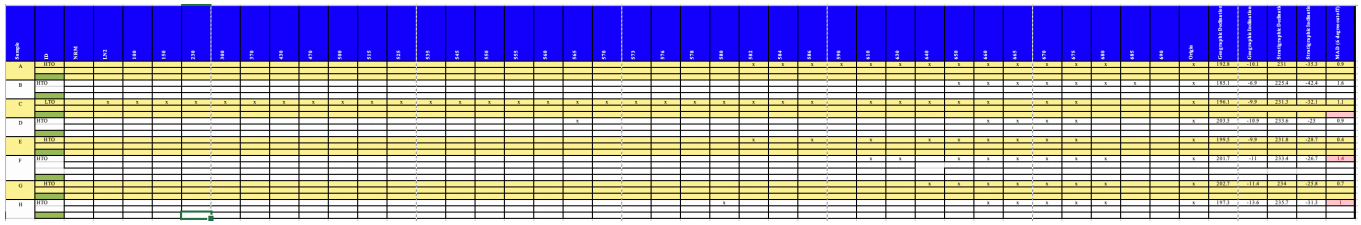

V19D03:

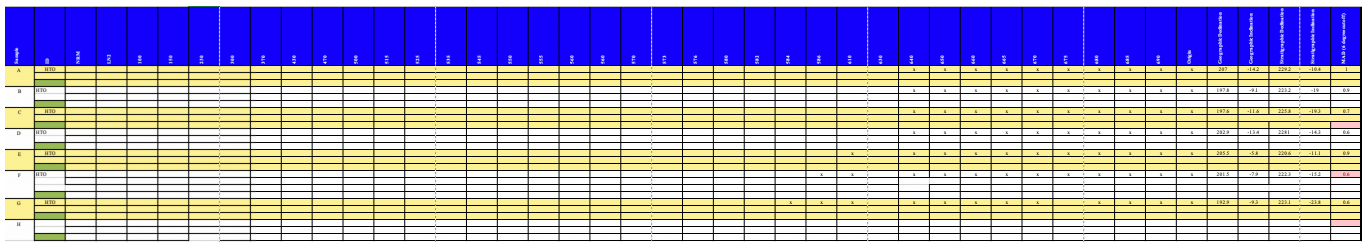

V19D04:

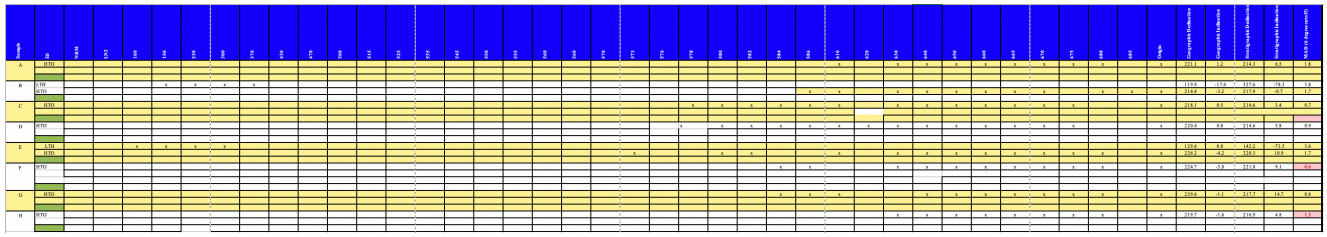

V19D05:

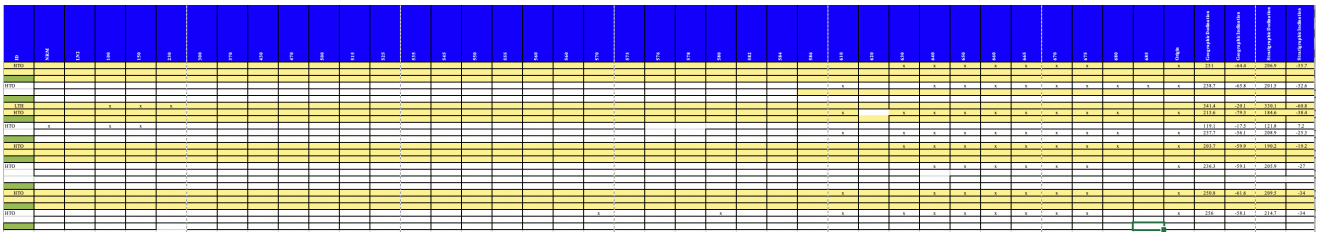

V19D06:

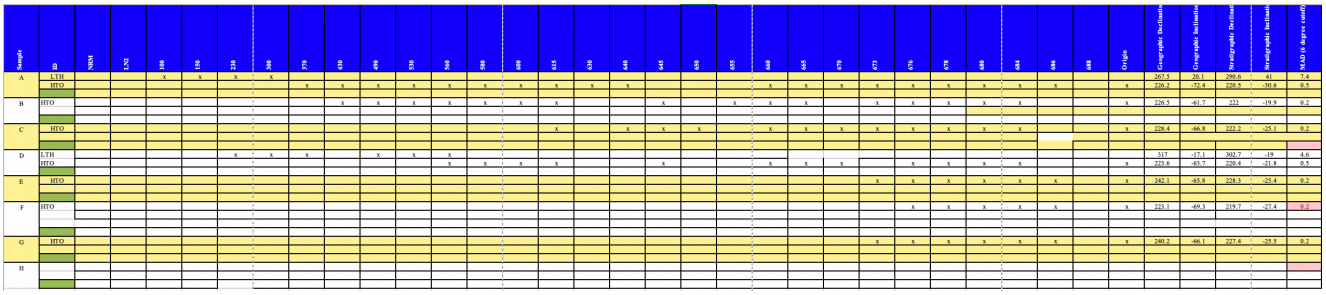

V19D07:

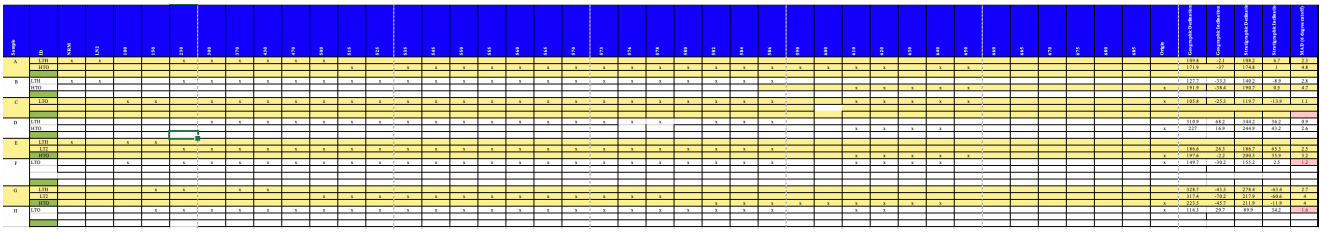

V19D08:

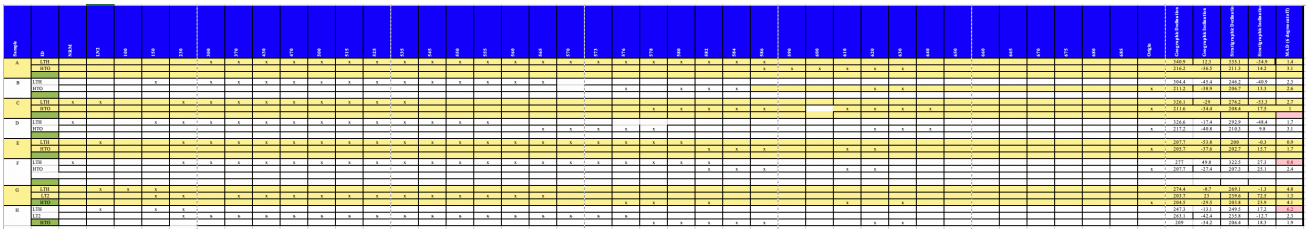

V19D09:

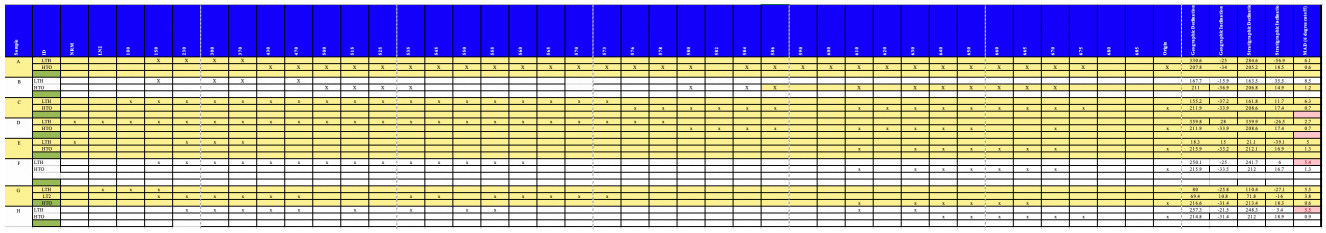

V19D10:

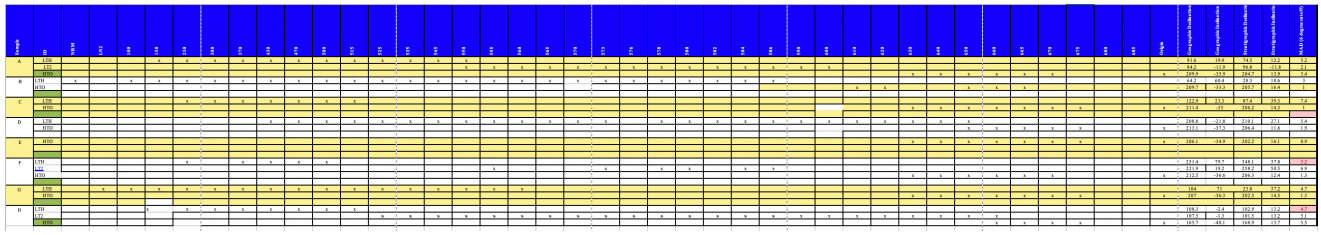

C19R1:

Sample	ID	NRM	LN2	100	150	230	300	370	430	470	480	490	500	510	520	530	540	550	560	570	580	Origin	Geographic Declination	Geographic Inclination	Stratigraphic Declination	Stratigraphic Inclination	MAD (5 degree cutoff)
A	LTH			X	X	X																					
	HTO						X	X	X	X				X		X			X			X	355.4	32.9	355.4	32.9	6.2
B	LTO	X	X	X	X	X	X	X	X	X	X		X	X	X	X	X	X	X	X	X	X	335	21.1	335	21.1	4.2
C	LTO	X		X	X	X	X	X	X	X	X	X	X	X	X	X	X	X	X	X		X	348.3	18.3	348.3	18.3	2.8
D	LTH	x	x		x	x																	331.4	-8.4	331.4	-8.4	3.8
	HTO						X	X	X	X	X	X			X	X	X					X	346.4	38.5	346.4	38.5	4.5
E	LTH		x	x	x	x																	61.2	-2	61.2	-2	5.3
	LT2						x	x	x	x	x	x	x	x	x	x							37.7	65.5	37.7	65.5	5.8
	HTO																x	x	x			x	316.5	48.2	316.5	48.2	2.7
F	LN2	x	x																				134.9	5.3	134.9	5.3	0
	LTH			x	x	x																	119.3	-15	119.3	-15	3.1
	LT2						x	x	x	x		x											55.6	63.5	55.6	63.5	2.7
	HTO													x				x	x			x	130.4	51.3	130.4	51.3	4.1
G	LTH	x	x	x	x	x	x																129.8	1.2	129.8	1.2	2.9
	HTO							x	x	x	x	x	x	x	x	x	x	x				x	132.4	30.5	132.4	30.5	5.3
H	LN2	X	X																				162.8	12	162.8	12	0
	LTH			X	X	X	X																150.5	7.9	150.5	7.9	3.1
	HTO									X			X	X	X				X	X		X	156.6	31.7	156.6	31.7	2.9

C19R2:

Sample	ID	NRM	LN2	100	150	230	300	370	430	470	480	490	500	510	520	530	540	550	560	570	580	Origin	Geographic Declination	Geographic Inclination	Stratigraphic Declination	Stratigraphic Inclination	MAD (5 degree cutoff)
A	LN2	x	x																				284.2	41.2	284.2	41.2	0
	LTH	x	x	x	x																		282.3	41.9	282.3	41.9	2.2
	LT2					x	x	x	x	x													295.9	52.8	295.9	52.8	5.5
	HTO										x	x	x	x	x	x	x	x	x	x		x	275.3	39.2	275.3	39.2	1
B	LTH	x	x	x	x																		261.8	49.2	261.8	49.2	2.2
	LT2					x	x	x	x	x	x	x											274.2	58.2	274.2	58.2	2.7
	HTO												x	x	x	x	x	x	x	x		x	254.5	48.1	254.5	48.1	1.4
C	LN2	x	x																				272.6	50.2	272.6	50.2	0
	LTH				x	x	x	x	x	x													307.2	61.3	307.2	61.3	4.3
	HTO										x	x	x	x	x	x	x	x	x	x		x	276	58.9	276	58.9	3
D	LTH	x	x	x	x	x																	272.2	69.5	272.2	69.5	4.9
	LT2						x	x	x	x													317.1	67	317.1	67	2.1
	HTO										x	x	x	x	x	x	x	x	x	x	x	x	275	63.4	275	63.4	1.1
E	LN2	x	x																				359.4	58.1	359.4	58.1	0
	LTH		x		x	x																	30.8	-58.7	350.8	-58.7	3
	LT2						x	x	x	x	x		x	x									340.6	53.5	340.6	53.5	2.1
	HTO														x	x	x	x	x			x	288.7	60.5	288.7	60.5	1
F	LN2	x	x																				342.4	39.8	342.4	39.8	0
	LTH			x	x	x																	329.3	-50.1	329.3	-50.1	5.9
	LT2					x	x	x	x	x	x		x										343.9	50.5	343.9	50.5	1.6
	HTO													x	x	x	x	x	x			x	302.7	59.1	302.7	59.1	1.1
G	LN2	x	x																				286.2	-40.6	286.2	-40.6	0
	LTH		x		x	x	x																5.7	-46.9	5.7	-46.9	4
	LT2						x	x	x	x													315.4	20.8	315.4	20.8	4
	HTO										x	x	x	x	x	x	x	x	x			x	289.1	-18.8	289.1	-18.8	1.3
H	LTH	x	x	x	x	x																	302.6	1.6	302.6	1.6	2.5
	HTO						x	x	x	x	x		x	x	x	x	x	x	x	x		x	299.6	20.8	299.6	20.8	3

C19U1:

Sample	ID	NRM	LN2	100	150	230	300	370	430	470	480	490	500	510	520	530	540	550	560	570	580	Origin	Geographic Declination	Geographic Inclination	Stratigraphic Declination	Stratigraphic Inclination	MAD (R-degree cutoff)
A	LTO			x		x		x	x	x	x	x	x	x	x	x	x	x	x	x		x	220.1	-7	220.1	-7	2.1
B	LTH		x	x	x	x																	239	-34.2	239	-34.2	1.4
	HTO								x	x	x	x	x	x	x	x	x	x	x	x		x	228.6	-8.6	228.6	-8.6	1.7
C	LTH	x	x	x																			268.4	-13.4	268.4	-13.4	1.2
	HTO				x	x		x	x	x	x	x	x	x	x	x	x	x	x			x	267.5	-5.8	267.5	-5.8	2
D	LTH	x	x	x	x	x																	287.4	-26.1	287.4	-26.1	1.3
	LT2						x	x	x	x	x												262.3	-18.1	262.3	-18.1	1.4
	HTO											x	x	x	x	x	x	x	x				252.4	-8.1	252.4	-8.1	2
E	NRM	x	x																				270.6	-18.8	270.6	-18.8	0
	LTH				x	x	x																293.6	-22.4	293.6	-22.4	5.5
	HTO							x	x	x	x	x	x	x	x	x	x	x	x			x	245.8	-4.4	245.8	-4.4	2.6
F	LTH	x	x	x	x	x																	275.1	-26.6	275.1	-26.6	0.5
	LT2						x	x	x	x	x	x											262.5	-13.7	262.5	-13.7	4.1
	HTO												x	x	x	x	x	x				x	248.7	-6.1	248.7	-6.1	2.2
G	LTH	x	x	x	x																		282.4	-2	282.4	-2	1.3
	LT2					x	x	x	x	x	x	x	x	x	x								272.9	4.2	272.9	4.2	6
	HTO															x	x	x	x	x		x	246.1	2.5	246.1	2.5	3.2
H	LTH	x	x		x																		316.6	26.1	316.6	26.1	4.6
	LT2						x	x	x	x	x	x	x	x									314.3	26.1	314.3	26.1	5.8
	HTO														x		x	x	x	x		x	221	17.8	221	17.8	1.3

C19U2:

Sample	ID	NRM	LN2	100	150	230	300	370	430	470	480	490	500	510	520	530	540	550	560	570	580	Origin	Geographic Declination	Geographic Inclination	Stratigraphic Declination	Stratigraphic Inclination	MAD (R-degree cutoff)
A	LTO		x	x	x	x																	328.6	-64.9	328.6	-64.9	12.1
B	LN2	x	x																				337.2	17.6	337.2	17.6	0
	LTO		x	x	x	x																x	334.8	-4.5	334.8	-4.5	8.9
C	LN2	x	x																				44.5	17.7	44.5	17.7	0
	LTO			x	x	x		x	x													x	5.1	-46.3	5.1	-46.3	3.1
D	LTO	x	x	x	x	x		x	x	x	x		x	x	x							x	337.3	-53.3	337.3	-53.3	1.5
E	LN2	x	x																				341.1	-5.9	341.1	-5.9	0
	LTO		x	x	x	x			x	x												x	340.9	-36.8	340.9	-36.8	5.2
F	LTO	x	x	x	x	x		x														x	340.9	-36.8	340.9	-36.8	8.5
G	LN2	x	x																				305	34.6	305	34.6	0
	LTO			x	x	x		x														x	316.9	-30.8	316.9	-30.8	7.8